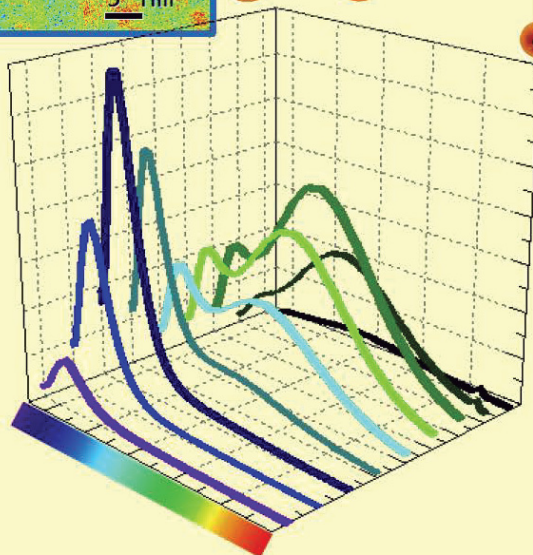
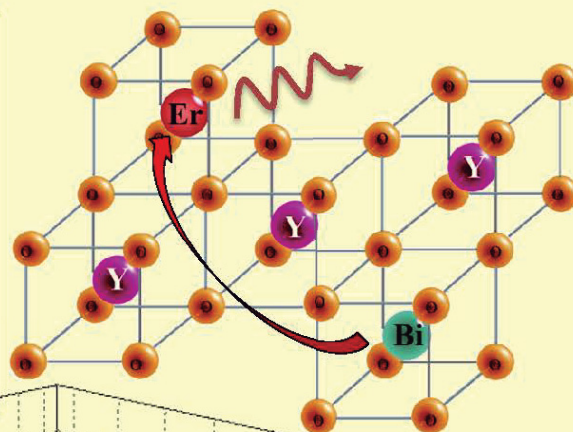
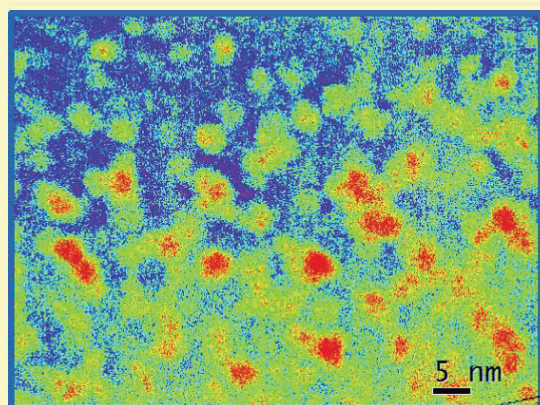


UNIVERSITÀ DEGLI STUDI DI CATANIA

Dottorato in Scienza e Tecnologia dei Materiali - XXVIII ciclo

Efficient light emission from bismuth-doped rare earths compounds for Si microphotronics

Adriana Scarangella



Tutor: Prof. Francesco Priolo

Supervisor: Dott.ssa Maria Miritello

Coordinatore: Prof.ssa Maria Grazia Grimaldi

UNIVERSITÀ DEGLI STUDI DI CATANIA



**DOTTORATO DI RICERCA
IN SCIENZA E TECNOLOGIA DEI MATERIALI
XXVIII CICLO**

Adriana Scarangella

**Efficient light emission from bismuth-doped
rare earths compounds for Si microphotronics**

**Tutor: Prof. Francesco Priolo
Supervisor: Dott.ssa Maria Miritello
Coordinatore: Prof.ssa Maria Grazia Grimaldi**

Tesi per il conseguimento del titolo

Cover

Top left: Bright field cross-sectional transmission electron microscopy image (in false colors) of Bi metallic precipitates in disilicates host after annealing treatment in nitrogen environment. More details can be found in section 3.2.3 within this thesis from page 123.

Top Right: Schematic of the bcc crystalline structure of (Er+Bi):Y₂O₃. The energy transfer process from Bi³⁺ to Er³⁺ ions and the consequent emission of a photon from Er ions are represented by red curved and wavy arrows respectively.

Bottom center: 3D emission spectra from Bi:Y₂O₃ by varying the excitation wavelength in the UV range (300 nm-400nm). The broad emission covers almost all the visible spectrum. More details can be found in section 2.3.3.

Efficient light emission from bismuth-doped
rare earths compounds for Si microphotonics

ADRIANA SCARANGELLA

Ph.D. Thesis – University of Catania

Printed in Catania, 10th December 2015

“I do not know what I may appear to the world, but to myself I seem to have been only like a boy playing on the seashore, and diverting myself in now and then finding a smoother pebble or a prettier shell than ordinary, whilst the great ocean of truth lay all undiscovered before me.”

“Non so come il mondo potrà giudicarmi ma a me sembra soltanto di essere un bambino che gioca sulla spiaggia, e di essermi divertito a trovare ogni tanto un sasso o una conchiglia più bella del solito, mentre l’oceano della verità giaceva inesplorato davanti a me.”

Sir Isaac Newton

Contents

Chapter 1: Silicon compatible materials for photonic applications	1
1.1. Silicon Microphotronics	3
1.1.1. Silicon microelectronics and its limits	3
1.1.2. The building blocks of Si photonic integrated circuits (PICs)	7
1.2. Silicon based light source: from materials and to devices	10
1.2.1. Visible light emitting materials and devices: state of art ..	10
1.2.2. Si quantum confined materials	15
1.2.3. Rare earths doped Si compatible materials for visible and infrared emission	19
1.2.4. Lasers on Si: Raman Si lasers and hybrid lasers	26
1.3. Silicon compatible materials for active photonic devices in the infrared wavelengths	31
1.3.1. Silicon passive waveguides for planar optical amplifiers ..	32
1.3.2. Enhanced light emission from active devices	37
1.4. Contents and motivations of this thesis	41
References	43
 Chapter 2: Bismuth-doped silicon compatible thin films for visible emission	 49
2.1. Bismuth as an emerging efficient emitter	51

2.1.1. Tuneable emission range controlled by the Bi oxidation state	52
2.1.2. Limits of the Bi application in Si-based light sources	55
2.2. Visible emission from Bi in silicate thin films	58
2.2.1. Yttrium silicate as a Si compatible host for emitting ions	58
2.2.2. Controlled emission range from Bi in yttrium disilicate thin films	63
2.3. Beyond the Bi solid solubility limit: Bi-doped yttrium oxide thin films	69
2.3.1. Yttrium oxide as a Si compatible host for REs ions	70
2.3.2. Optimization of the yttrium oxide host for Bi dissolution	72
2.3.3. Wavelength selective Bi^{3+} emission range	76
2.3.4. Three levels model for Bi^{3+} PL temperature dependence	82
2.3.5. Intense cathodoluminescence for FEDs applications	93
2.3.6. Bi^{3+} concentration influence on optical efficiency	94
2.4. Conclusions	97
References	100
 Chapter 3: Bismuth-enhanced erbium emission for telecommunications	 105

3.1. The use of bismuth as emitter for telecommunication windows	107
3.2. Bismuth in erbium-yttrium disilicate thin films	114
3.2.1. The approach of Er-based compounds to increase optical efficiency: the mixed Er-Y disilicate	114

3.2.2. Solubility of Bi ions under high temperature annealing and its influence on Bi-Er coupling.....	116
3.2.3. Chemical evolution of Bi precipitates under oxidizing or inert thermal treatments.....	123
3.2.4. Blockage action of Bi agglomerates in O ₂ atmosphere..	132
3.3. Bismuth as a sensitizer for Er optical emission in yttrium oxide thin films.....	137
3.3.1. Er spectroscopy in yttrium oxide.....	139
3.3.2. Efficient Bi and Er coupling for visible and infrared emission.....	143
3.4. Conclusions.....	154
References.....	156
 List of Publications.....	 161
 Acknowledgments.....	 163
 Curriculum Vitae.....	 165

Chapter 1: Silicon compatible materials for photonic applications

For almost 50 years, silicon microelectronics has been the engine of the modern information revolution, owing to the advent of the nanotechnology era that has produced always faster, cheaper, smaller and more performing devices inside the same silicon chip. However its fortune might be coming to an end. Indeed, as a consequence of the continuous reduction in size, much longer electrical interconnects are required, thus leading to an increase of signal delays and to electromagnetic interferences that cause power dissipation and limit the total performances of a chip.

A possible solution to this problem can be obtained by replacing the electrical interconnections with the optical ones by the realization of a totally integrated photonic circuit on a silicon platform. For this reason, recently strong efforts have been devoted to the development of the main constituents of a photonic circuit, such as waveguides, splitters or multiplexers, detectors, etc. However there is still a lack of integrated infrared light sources that are required to generate logic value 1-0 and to compensate the optical losses in waveguides. In addition recently also the demand for efficient integrated visible light sources for LEDs, displays and lab-on-chip applications is increasing. Different strategies have been proposed to satisfy these requirements and will be reviewed in the following chapter, by evidencing their strengths and their limits.

In order to further increase the efficiency of these light sources and to realize integrated photonic circuits, their coupling with passive devices, such as SOI or plasmonic waveguides and photonic crystals, has been recently proposed owing to the existence of several interesting effects. Two completely different approaches will be pursued in this thesis work: (i) the synthesis of silicon compatible REs compounds in which the REs amount can be varied in a continuous way increasing the efficiency of the light source without suffering from detrimental effects and (ii) the contemporary introduction of post-transition metals as either strong emitting elements in

the visible range or as sensitizers for the infrared emission, thus suggesting these materials as good candidates for an integrated light source on silicon.

1.1. Silicon Microphotonics

The modern information revolution is requiring always faster, smaller and more performing constituents to be integrated in our modern personal computers and smartphones. However a further downscaling of the dimensions by maintaining high the performances is going to become impossible in silicon microelectronic devices. In this section, a brief overview of Si microelectronics and its limits will be addressed and Si microphotonics will be proposed as a possible technological solution for devices.

1.1.1. Silicon Microelectronics and its limits

For almost 50 years, silicon microelectronics has been the engine of the modern information revolution. Since silicon is the second most abundant element on earth after oxygen, with a high refractive index of 3.47 at 1550 nm and transparent to infrared light with wavelengths above approximately 1100 nm, silicon wafers have still the lowest costs per unit area and the highest crystalline quality. In addition silicon large thermal conductivity, hardness, and low density are useful properties for semiconductor devices fabrication [1]. Complex microprocessors, dense memory circuits and other digital and analogic electronic devices mainly have the aim to process more and more data in a faster way using smaller components.

Indeed, since the development of the first transistor, a process of miniaturization started, moving to a huge size scaling towards the years that have brought the number of components inside the same chip to increase very fast. In particular a doubling of the number of transistors per chip every

18 months was observed by Moore [2] during the five years 1959-1965 and a grown trend was predicted up to 1975. Moreover this growth has maintained the same rate up to now by causing a total drop of the transistor price, from \$5.52 dollars in 1954 to one billionth of a dollar in 2005.

In this contest, silicon industry has successfully developed a complementary – metal – oxide semiconductor (CMOS) technology in order to realize silicon integrated circuit (IC) with many components grown monolithically in the same chip, in order to process, transfer and modulate the information with always increasing data rates. An example of the evolution of the Si IC since the development of the first prototype by Noyce and Kilby (1961, that gave the Nobel Prize to Noyce in 2000) is shown in Fig. 1.1 compared with a modern silicon wafer covered by billions of transistors [3].

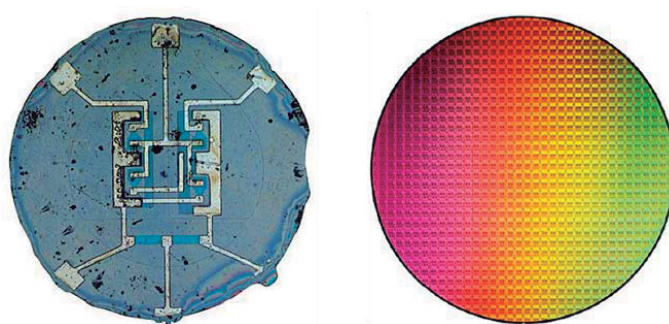


Figure 1.1. a). First integrated circuit available as a monolithic chip invented by Fairchild Camera and Instrument Corp in 1961 [3]. b) Intel Core, 1.3 billion transistors per chip (2015) [4].

CMOS technology is now arrived to the sub-10 nm range and future scaling trends have been predicted by the International Technology Roadmap for Semiconductors (ITRS [5]). Today gate oxide length is expected to reach at least 7 nm, but in such small dimensions some other issues have to be taken into account, as the inexistence of practical solutions

for interconnections to contact such small atomic nodes by maintaining high the device performances and contemporarily lowering the power consumption [6]. Therefore the problems of microelectronic downsizing relies on the die integration into circuits in which the transfer of the information is given by metallic interconnections. The resistance and capacitance increase by increasing the length of the metallic stripes, resulting in an increasing resistive-capacitive delay (RC delay) that limits the total device speed even if the intrinsic gate delay is decreasing by shrinking its dimension. Figure 1.2 shows the comparison of the gate delay with the delay for two different metallic connections versus gate length. This limit is known as the interconnection bottleneck [7].

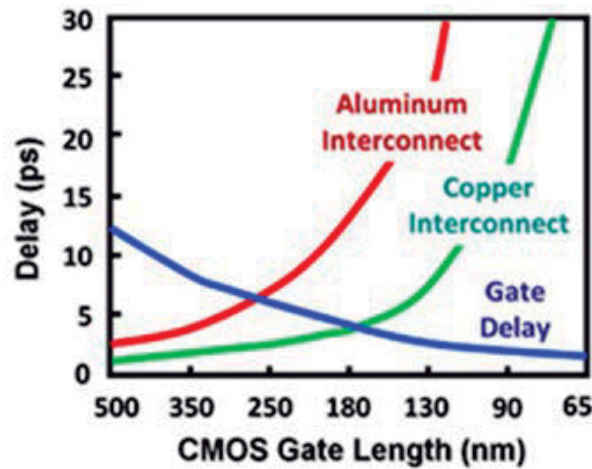


Figure 1.2. Comparison of the predicted gate delay and interconnect propagation delay in transistor versus technology generation [8].

Microphotonics has been proposed as a possible solution in order to overcome the microelectronic limits for interconnections. The idea is to use photons instead of electrons to carry and process the information, permitting much higher data rates compared with metallic wires. This approach is

already commercially available for long scale communication systems; in particular for data rates over 1 Gbps and distances exceeding 100 m, optical interconnection as silica optical fibers [9] have already developed. Using proper wavelength division multiplexing (WDM) systems (which multiplex a number of optical carrier signals onto a single optical fiber by using different wavelengths of a laser, enabling multiplication of capacity), optical systems are able to transmit many channels of data along a single fiber; systems with 40 different wavelengths, related to different information travelling at 10 Gbps, are commercially available and implemented at various points in the world wide telecommunication backbone.

The limits of photonics relies in the cost of the traditional optical systems, that are so expensive principally for the used exotic materials and for its fabrication technology, mainly based in discrete components and serial (step-by-step) fabrication instead of a monolithic one. Since electrical components are built by the standard CMOS technology that is globally optimized to bring the system costs down, the “Holy Grail” of photonics would be the integration of optical communication systems into a CMOS platform in order to deliver the superior performance of optics at the same cost as electronics.

To keep the cost low, however photonics has to satisfy some requirements, as the coexistence with CMOS materials (generally Si-based) [7] and the compatibility with CMOS processing steps and temperatures. The solution could be than to merge electronics and photonics into an integrated dual-function Si platform, called optoelectronic integrated circuit (OEIC) fabricated using the Si infrastructure.

With this purpose, in the last decades strong efforts have been devoted to the research of Si-based photonics materials and devices in order to

implement photonics into electronics. Even if nowadays it is already possible to find several photonic commercialized devices for long scale telecommunication systems, issues are still present in smaller scale, as in the connection between circuit boards, chips inside board and even between dies in the same chip.

In the next sections, a brief introduction on Si microphotronics IC and its constituent parts will be given, pointing on the newest results.

1.1.2. The building blocks of Si photonic integrated circuits (PICs)

The monolithic integration of Si photonic devices and CMOS electronics was proposed mainly to create highly dense circuits with lower costs. One example of totally integrated photonic circuit is shown in Fig. 1.3 where the merging of the basic building blocks of a silicon photonic integrated circuit (PIC) with electronics components is proposed [10].

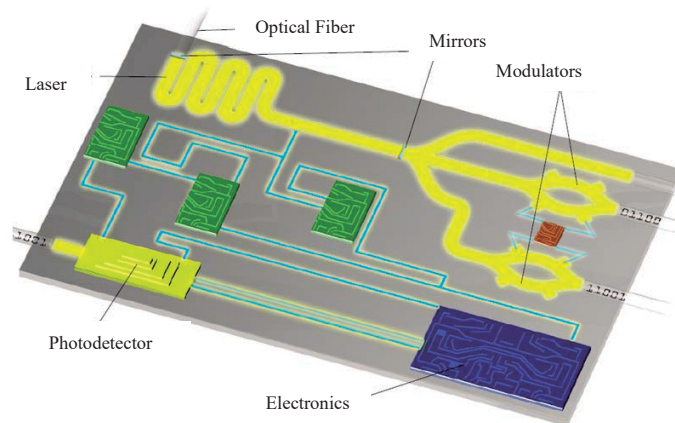


Figure 1.3. a). Schematic representation of a totally integrated photonic circuit with electronic and photonic components both coexisting in the same chip [10].

Although PICs offer several advantages for Si photonics, they also introduce complexity in the integration process due to the dimensional mismatch between the sub-100 nm size of electronic devices and the 0.1–1 μm size of photonic components, makes challenging the optimization of this coupling.

Among the PICs component (known also as building blocks), it is possible to distinguish between passive components, as waveguides, filters and directional couplers, so defined because no source of energy is required for them to operate, and the active ones, that require an external source of energy for its operation and have an output related to the input signals, as Si modulators, detectors, lasers [11].

The passive components are used to transmit, switch, encode and carry light up to a detector where the optical signal is converted into an electronic one. During the past decades, strong efforts have been made on the development of light modulators and Si waveguides and the optimization of the fiber-to-waveguide coupling. Couplers such as inverted taper, made by a Si core and a SiO_2 or a polymer cladding with the aim to expand or reduce the optical mode in order to match the modal size of the fiber, or such as grating, where the periodic structure assists the light coupling, have been already widely studied [11,12].

Utilizing these building blocks, Intel researchers announced in 2010 the first complete Si-based PIC, shown in Fig 1.4 [13]. The complete device includes two silicon chips, a transmitter and a receiver. The transmitter is composed by hybrid Si lasers connected with four optical channels, each running at 12.5 Gbps, which are combined by a passive multiplexer onto a single fiber to transmit data up to 50 Gbps to the receiver where a

demultiplexer and a set of four integrated photodetectors collect the light and convert it into an electrical data stream.

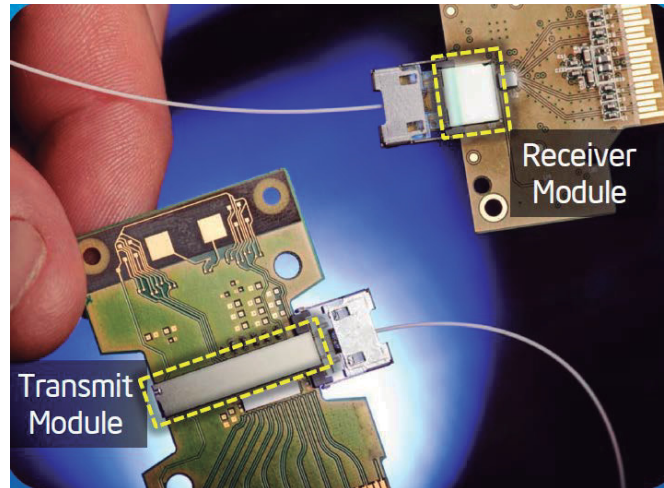


Figure 1.4. A 50 Gbps Silicon Photonics transmit module (left) sends laser light from the silicon chip at the center of the green board to the receiver module (right), where a second silicon chip detects the data from the laser [13].

Despite this important example in Si integrated data connection, the biggest issue remains unsolved, i.e. the realization of efficient active Si compatible emitting devices. Indeed while also Si-based modulators [14] and photodetectors [15] are already optimized, light sources as light emitting devices (LEDs) and lasers coupled with active waveguides and optical amplifiers are still under extended and dynamic investigation. The most recent and important examples will be discussed in the following sections.

1.2. Silicon-based light source: from materials to devices

Since the development of the first monochromatic red LED using GaAsP semiconductor in the sixties, the LED efficiency is strongly increased, especially in the last years, owing to the development of more performant technologies and to the increase of the demand. Nowadays colored LEDs have already become the technology of choice for traffic signals, interior and exterior vehicle lighting, replacement of neon, etc. Today further applications are raising, from the backlights for cell phone displays and huge flat panel television, to the lab-on-chip and sensor systems for use in biotechnology, pharmaceutical, biomedical research, clinical diagnosis and environmental analyses. From a technological standpoint, high-efficiency LEDs integrated on the Si platform would be a great result [16,17]. In addition such devices could offer significant advantages over the standard light sources in terms of costs, compatibility, reproducibility, etc. In the next section, the state of art of the emitting materials for LED and field emission displays (FED) applications will be discussed; then the attention will be pointed in the development of new approaches for Si visible and infrared integrated light sources.

1.2.1. Visible light emitting materials and devices: state of art

LEDs are optoelectronic devices consisting of multiple components, grouped in die and packaging parts. The die is composed by a thin single crystal layer of a semiconductor p-n junction that generates the emitted light after electrical stimulation (responsible of the internal quantum efficiency, IQE). The packaging contains instead electrodes, thermal dissipation

Nowadays, the already commercialized LEDs are mostly made from III–V semiconductors, due to their high IQE, result of their direct band gap. In addition the advances in their development have allowed a fine tuning of the emission wavelength from the UV to the infrared (IR) by using semiconductors with a suitable band gap. A restriction of these types of LEDs is the difficulty to realize p- or n-doping, which is essential to have a LED. LEDs are nowadays mainly based on III-phosphide semiconductors, that exhibit high efficiency in the red but very scarce at shorter wavelengths due to the weak carrier confinement and to the indirect minima in the conduction band. Another developed class is the III-nitride systems that have high efficiency in the UV-blue but suffer from losses for longer wavelengths, owing to defects and dislocations [18]. This behaviour is clearly represented in Fig. 1.6 where the external quantum efficiency (EQE= IQE×EXE) is shown as a function of the emitted wavelength.

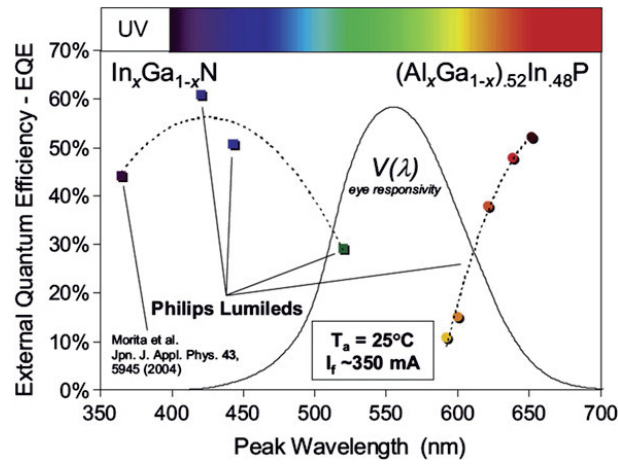


Figure 1.6. External quantum efficiency versus the emitted wavelength for the standard used semiconductor materials for LEDs. The eye response $V(\lambda)$ is also shown [18].

Even if efficiencies of the order of 50-70% have been obtained for red and blue LEDs, the efficiency of the green LEDs, where the eyes response $V(\lambda)$ has a maximum, is still very low. Thus there is a lack of green sources for LED applications, called as the “green gap”.

This “green gap” also affects the realization of white LEDs (WLEDs). Indeed one of the most used approaches to realize WLEDs is to mix red, green and blue LEDs. This approach, shown in Fig. 1.7.a), has some limits related not only to the absence of efficient green LEDs but also to their different efficiencies in time (aging) and their intrinsic narrow emissions. This results in a poor colour rendering index (CRI), defined as the ability of a light source to accurately render all frequencies of its colour spectrum when compared to a perfect reference light. Alternatively, white LEDs can be produced starting from a monochromatic UV-blue LED combined with phosphors (phosphors converting LEDs), materials containing emitting elements generally in the form of powders. The phosphors are luminescent materials able to convert light from lower to higher wavelength. The most common used one is the Ce:YAG (yttrium aluminium garnet) that emits yellow light, as shown in Fig.1.7.b).

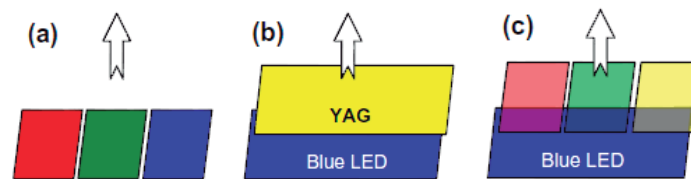


Figure 1.7. Different procedures for white light production. **a)** LEDs color mixing; **b)** color conversion from a blue LED coupled with a yellow phosphor; **c)** color conversion from a blue LED coupled with red, green, and yellow nanophosphors [18].

Also the combination of a blue LED with green+yellow+red phosphors have been already proposed to obtain warmer light, as shown in Fig. 1.7.c). Obviously, these approaches permit to have higher CRI but lower efficiency. An alternative to LEDs and pc-LEDs for displays and flat screens is the field emission display (FED) technology [21] that uses the principle of cathodoluminescence (CL) [22], i.e. the emission of light after excitation by electron beams, instead via current flows. However in order to have comparable high efficiency, most of the available phosphors nowadays must work with a very high electron voltage beam (5-10 kV ranges), usually obtained by cold cathode electron emitters needing vacuum conditions. This last point makes this technology not preferred due to the risk of vacuum breakdown [23] that limits the device lifetime. For these reasons, the research nowadays is moving towards materials which show bright luminescence under lower electron voltage beam (<5 kV).

Since all these examples represent a trade-off between the spectral response and the efficiency, the ideal solution would be the development of new alternative materials in order to cover all the required ranges without using the combination of more light sources. In addition either direct bandgap semiconductor materials or phosphors are not compatible with the standard Si technology, therefore they cannot be applied as light sources for integrated circuits.

Since the indirect band gap makes silicon an inefficient light emitter, realizing a Si light source is tricky and several strategies have been proposed. Some examples of Si-based visible and infrared light emission will be illustrated in the next sections, even if it still remains a challenge to achieve electrically pumped room-temperature (RT) continuous-wave (CW) devices.

1.2.2. Si quantum confined materials

Due to the increasing demand of integrated visible light sources on Si platforms, many options have been explored, such as the alloying Si-Ge, and the strain and defect engineering. The most successful approach to obtain light emission from Si is the quantum confinement in nanostructures [24]: when one or more dimensions are reduced to nanometric sizes (1-10 nm), the electrical and optical properties of quantum confined materials change with respect to the bulk. As a consequence when electron-hole (e-h) pairs become spatially confined, the translational symmetry of the system is no more satisfied and the wave-functions become squeezed in the real space, but broaden in the momentum space. This causes a relaxation of the momentum conservation and it has some consequences:

(i) e and h can be treated by particles-in-a-box arguments, thus only some wavelengths can be supported by the material, i.e. the permitted energies become quantized and strictly connected to the dimensions (L) following the relationship

$$E_g = E_g^{Si} + \frac{\hbar^2}{2\mu} \left(\frac{\pi}{L} \right)^2 \quad (1.1)$$

Therefore by reducing the grain size a blue shift from the 1140 nm emission of a bulk Si is observed. One example of a strong red emission from the 0D structure of Si nanocrystals (Si-nc) in toluene under UV irradiation is reported in Fig. 1.8 [25].

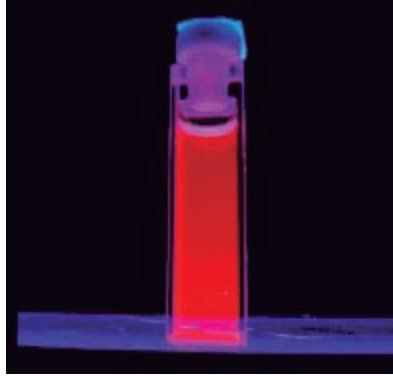


Figure 1.8. Emission of a cuvette filled with a colloidal suspension of Si-nc in toluene under UV illumination [25].

(ii) Change of the local density of states (LDOS) and increase of the radiative recombination probability [26] have been obtained. In addition, the spatial constrictions result in a lower probability that e-h pairs meet non-radiative recombination centers. As a demonstration, the typical Si bulk radiative lifetime of the order of ms reduces up to μs for Si-nc as the nanoparticles dimension decreases.

(iii) Participation of oxygen and/or interface-related states has been suggested to affect the PL properties [24]. Also the contrast of refractive index of the Si nanostructures with respect to the surrounding medium can increase light extraction efficiency from the material reducing the internal reflections. As a result, internal quantum efficiency increases. For Si-nc, values larger than few percent [25] have been demonstrated, up to 60% [27].

Since the discovery of a visible broad luminescence from porous Si [28] and the development of new fabrication technologies, strong efforts have been devoted to the synthesis of Si nanostructures, mostly Si-nc and Si nanowires (NWs). The first ones have been synthesized by different methods, from the chemical synthesis by exploiting reactions of suitable

precursors [25,29], useful for biological applications, to the thermodynamically induced self-aggregation in non-stoichiometric dielectrics [30], synthesized by magnetron co-sputtering, chemical vapor deposition (CVD), sol gel methods, etc. Figure 1.9.a) reports a high resolution transmission electron microscopy image of Si-nc grown in SiO₂ starting from a Si rich oxide.

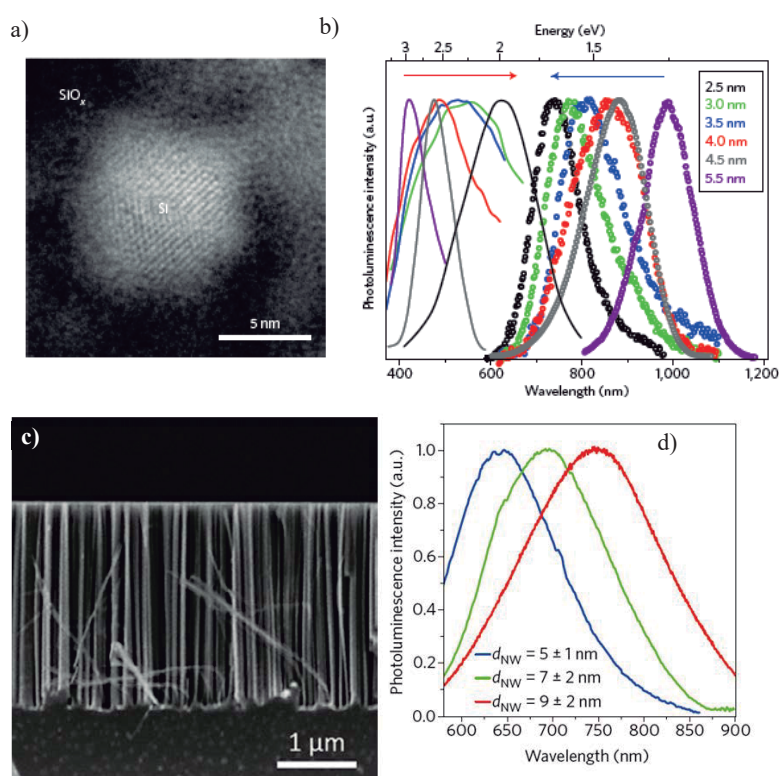


Figure 1.9. a) High-resolution transmission electron microscopy image of a Si-nc embedded in SiO₂ [30]; b) blue-shift of Si-nc emission by decreasing their size [31]; c) SEM image from Si NWs and d) their typical size-dependent shift of emission peak from Si nanowires with different mean diameters [33].

Tuning of the optical band gap over a wide range of energies from about 0.9 eV to 4 eV for the smallest synthesized nanocrystals has been obtained [24]. The tunable photoluminescence is shown in Fig.1.9.b) by the blue-shift from about 1000 nm to 700 nm, accompanied by other effects as the down-shift of “direct-bandgap” characterized by an emission from 400 nm to 600 nm [31].

Also for Si-NWs several fabrication methods have been exploited, as nanolithography, vapor-liquid-solid (VLS) methods and metal-assisted chemical etching [32], obtaining very thin and long structures, strongly confined in two dimensions, as shown in Fig. 1.9.c). Also in this case, the control of the Si NWs thickness results in a control of the emitted wavelengths, as shown in Fig. 1.9.d). Internal quantum efficiency of the order of 0.5% has been already obtained for this structure [33].

The research of luminescent materials has been accompanied by strong efforts dedicated to the realization of electroluminescent MOS devices made by Si-nc in SiO₂. An example is reported in Fig. 1.10.a) where an Emission Microscopy (EmMi) image in false colors, proportional to the intensity of the emitted light, is illustrated [34]. The challenge in these structures is represented particularly by the difficulty of electrical injection. This can be solved by using Si-NWs that, in addition to the similar optical properties, could permit a continuous conduction of current along the wires length. EL devices have been indeed demonstrated. One example is shown in Fig. 1.10.b) where a LED made by p-type NWs contacted by a n-type transparent electrode (AZO) is reported [33].

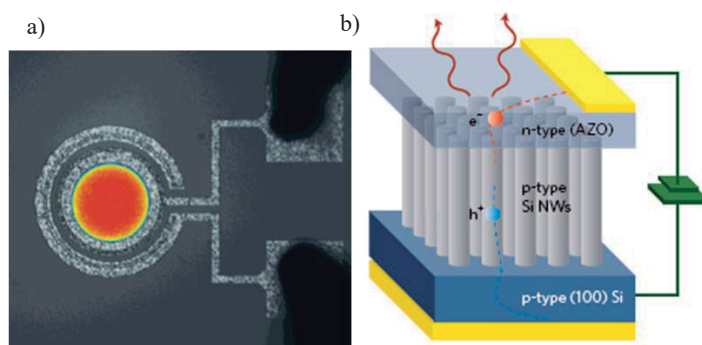


Figure 1.10.a) EmMi image of a typical Si-nc electroluminescence device showing uniform red emission [34]; **b)** Schematic of an electroluminescent device using p-type Si nanowires [33].

Although many efforts are dedicated to the realization of always more efficient Si nanostructures, the challenge of current flows together with some drawbacks in the synthesis procedures (such as the difficulty in obtaining uniform doping and in the size control, the presence of metals, the presence of surface states and defects, the strong dependence on processing parameters, etc.) have not yet made possible the commercialization of these structures.

1.2.3. Rare earths doped Si compatible materials for visible and infrared emission

In this scenario, the introduction of rare earths (REs) as guests in Si-based dielectric hosts has also been proposed as alternative to Si nanostructures for visible and infrared light sources [35]. REs are characterized by a peculiar electronic configuration, $[\text{Xe}]4f^n6s^2$ (with $1 \leq n \leq 14$) with a partially filled 4f shell and the same outer-shell configuration, namely $5s^25p^66s^2$, therefore they all show very similar

reactivity and coordination behavior. Since 4f electrons are not the outermost ones, they are shielded from the external fields by the 5s and 5p electronic shells, thus resulting only weakly perturbed by the charge of the surrounding ligands. Many optical properties of RE ions depend on 4f shell electrons. Thus when a RE ion is introduced into a solid, it loses its outer electrons (3+ valence state) but, since the 4f electron wave-functions are localized, the resulting energy spectrum is composed by a series of atomic-like levels weakly affected by the crystalline field. Thus the REs optical properties, as absorption and emission spectra, can be understood from consideration on the free ions. The presence of a crystalline field induces only a splitting of the atomic-like levels in multiplets, as schematically represented in in Fig. 1.11 for a trivalent RE ion (erbium). This effect, however, is crucial in allowing radiative emission. In fact, 4f-4f transitions are forbidden in a free ion by the electric dipole selection rules and only a state mixing caused by the crystalline field through the Stark effect makes these transitions possible when REs are embedded in solid hosts.

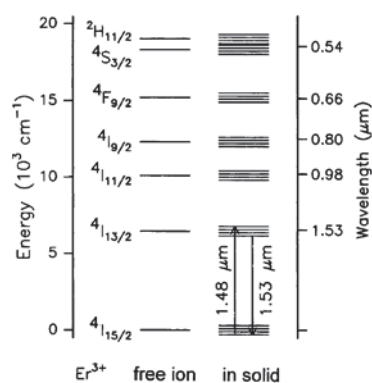


Figure 1.11. Schematic representation of Er energy levels in absence and in presence of the crystal field. Stark effect splits Er energy level. The Er main transition is also indicated [39].

Trivalent visible emitting REs already widely known are Tb^{3+} , Ce^{3+} , Eu^{3+} and Gd^{3+} for the green, blue, red and UV emission respectively [36]. REs activated luminescent materials are widely used for solid-state lasers, fluorescent lamps, flat displays, optical fiber communication systems and other optical devices already commercialized and nowadays a big field of research is using them as phosphors for pc-LEDs. However since strong efforts are currently undertaken worldwide to achieve efficient light emission from REs doped Si based materials and devices with the aim to develop an integrated optoelectronic platform on Si, the optimization of their optical properties by an improvement of the host quality and of the dopants dissolution in order to maximize the internal and external optical efficiency is still an important research field.

Such REs doped materials appear attractive due to the compatibility with the standard CMOS technology and represent not only the basis for inter-/intrachip optical interconnects but also find applications in micro-displays, waveguide amplifiers, biological agent detection, solid state lighting, sterilization, etc.

Despite the fact that photoluminescence properties have been already widely studied, a very few works exist on their EL properties, i.e. on their emission after electrical excitation, necessary to realize Si integrated optical devices. Examples on light sources operating in the green, blue and ultraviolet (UV) have been recently demonstrated [37,38]. Two of the most significant MOSLEDs based on 100 nm thick Eu-doped or Gd-doped SiO_2 are reported in Fig. 1.12. In particular, Fig. 1.12.a), b) and c) show the optical photographs of the EL from a 200 μm diameter Eu-based device excited by different currents, 20 μA , 1 mA and 2.5 mA. The PL spectra for

different Eu contents are also reported in Fig. 1.12.d) ascribed to the contemporary presence of Eu^{2+} and Eu^{3+} oxidations states.

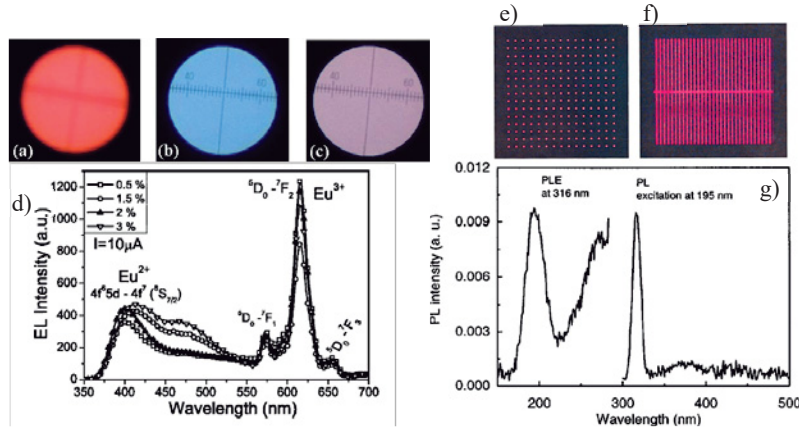


Figure 1.12. a)-c) Optical photographs of the EL from Eu-based device under different currents. d) EL spectra for different Eu contents [37]. e)-f) CCD photographs of the EL emission from two different structures of Gd-based devices and g) relative PL and PLE spectra [38].

The different colors in EL can be justified by a selective excitation through the impact of electrons with different energies. Instead from the PL and PLE shown in Fig. 1.12.g) it was possible to observe the peculiar Gd emission line at 316 nm overlapped with a broader band (2000 times weaker) related to emission from defects that are used as a benchmark for EL emission in the CCD photographs reported in Fig. 1.12.e) and f) for two different structures.

A widely used approach to generate light emission in the infrared is to introduce Er as an impurity element in materials fully compatible with the standard Si technology. The importance of Er relies mostly on its transition ${}^4\text{I}_{13/2} \rightarrow {}^4\text{I}_{15/2}$ with emission of a photon at $1.54 \mu\text{m}$ [39], shown in Fig. 1.11, and its amplification can be obtained by involving the upper level ${}^4\text{I}_{11/2}$ by

pumping it at 980 nm. The 1.54 μm emission is of big importance for telecommunication because it falls in the minimum loss of optical fibers. Indeed Er doped fiber amplifiers (EDFA) with high lengths and low Er content are already commercialized.

In order to apply Er-doped materials as amplifiers in microphotonic applications by maintaining high the efficiency, higher Er content should be introduced. However, this brings to detrimental phenomena that avoid the possibility to have light emission and amplification from all the REs ions for the following reasons:

(i) a solid solubility limit is encountered when Er ions, above a critical concentration threshold, whose value is different for each host, start to segregate and precipitate by forming optically inactive (metallic) clusters. This phenomenon is more marked after annealing treatments, owing to the high mobility of Er ions in Si-based compounds, as shown in Fig. 1.13.a) by the cross-sectional transmission electron microscopy (TEM) image of Er-doped SiO_2 after annealing treatment at 1200°C for 1 h [39]. This cluster formation is always detrimental for Er optical properties, as shown in Fig. 1.13.b): while an increase of both PL and lifetime values by increasing the annealing temperature is reported up to 700°C, owing to the recovery of defects introduced by ion implantation, the PL quenches for higher temperatures. This demonstrates the formation of Er optically inactive nano-clusters, unwanted for photonic applications.

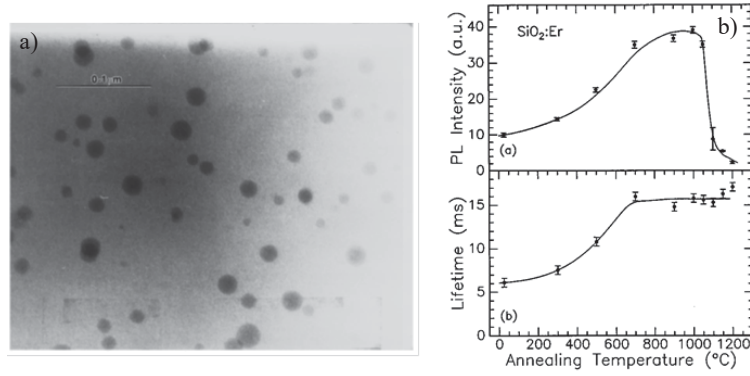


Figure 1.13. a) TEM image of Er metallic clusters in SiO₂ after annealing treatment at 1200°C for 1 h; b) Relative room Temperature PL peak intensity and lifetime at 1.54 μm measured as a function of temperature [39].

(ii) Concentration quenching and cooperative up-conversion are instead based on the interactions between Er ions, whose probability increases by increasing the Er content. The first one is characterized by the interaction between an Er ion excited in $^4I_{13/2}$ energy state and a nearby one in the ground state: indeed the first one can de-excite either emitting a photon or transferring the absorbed energy to the nearby one, by causing an energy migration that can be concluded by the emission of a photon, Fig. 1.14.c), or by a non-radiative transfer to a quenching center, Fig. 1.14.d) [40], thus lowering the total optical efficiency of the system. This phenomenon will be discussed better in the next chapters of this thesis work.

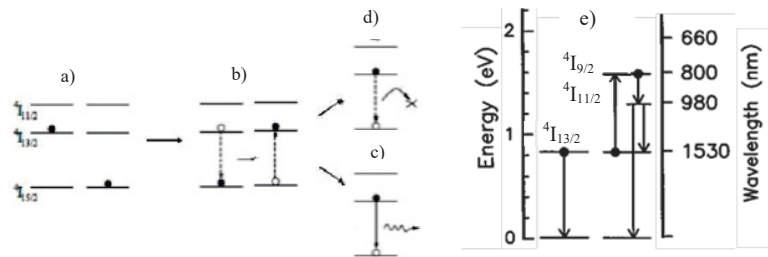


Figure 1.14. a)-d) Schematic of the concentration quenching process and of e) upconversion for Er ions [39].

The second one involves instead two Er ions excited in the same energy levels and it is influenced also by a high excitation photon flux (that favours the probability of having two excited Er ions close one another). As a consequence, the first one can de-excite non radiatively to the ground state transferring the energy to the second one, that is excited to an upper energy level. Depending on the Er energy levels involved, different cooperative UP processes can happen. An example is shown in Fig. 1.14.e): if Er ions are both in the $^4I_{13/2}$ energy level, the second one can be excited up to the higher $^4I_{9/2}$, de-exciting again non-radiatively up to $^4I_{11/2}$ and then emitting a photon at 980 nm or at 1540 nm at the expense of two photons at 1540 nm. The occurrence of UPs determines a sub-linear increase of PL intensities at 1.54 μm versus the photon flux and a “stretching” of the correlated decay time because of the faster depletion of the energy level in presence of UP. Obviously these processes lower the PL efficiency at 1.54 μm useful for light amplification in the IR, but contemporarily permit to obtain and enhance the Er visible emission through excitation in the IR, of great interest for bio-applications [41]. Thus a specific control of Er-Er mean distances and interactions is fundamental to permit the realization of efficient light sources and amplification in the infrared.

In addition to the many efforts devoted in finding new approaches to solve these limits, another aspect that has to be taken into account is the low Er excitation cross section due to the nature of its transitions, forbidden by the parity selection rules and partially permitted only in presence of a crystal field. The use of a broad sensitizer can relax the stringent conditions for high pump sources in optical amplifiers and raise the system efficiency. One of the most proposed approaches is to use Si-nc as broadband high absorbing sensitizers for Er to realize an Er doped wavelength amplifier (EDWA)

where the pump laser can be substituted by LEDs or even by electrical injection [42,43], thus opening the way towards an on-chip laser. Si-nc have typical wide absorption spectrum in the visible with absorption cross sections of the order of 10^{-16} cm^2 around the 488 nm region [44] that is five orders of magnitudes higher [45] than that of Er^{3+} in stoichiometric silica ($8 \times 10^{-21} \text{ cm}^2$ at 488 nm). A strong energy coupling has been demonstrated in Er^{3+} -doped silica containing Si-nc [46]. In addition to the possibility to increase the Er effective excitation cross section, Si-nc can conduct electrical current, opening the route to electrically pumped optical amplifiers. However, many aspects of the exact nature of the interaction and the energy transfer processes are still controversial and under investigation and despite the presence of several promising results, the presence of some limiting factors such as strong carrier absorption, cooperative upconversion, excited state absorption, Auger de-excitation and low fraction of Er^{3+} ions coupled to the Si-nc [47] need to be faced.

Thus, the application of REs doped materials in Si microphotronics have still some unresolved open points.

One of the approaches that will be then pursued in this work in order to realize efficient Si-based light sources is the doping with heavy metal ions in place of REs and the development of REs compounds in place of the doped Si-based materials for visible and infrared emission.

1.2.4. Lasers on Si: Raman Si lasers and hybrid lasers

In addition to the already discussed approaches to achieve visible and infrared emission from Si-based materials, different strategies have been developed in order to realized infrared lasers on Si. Raman scattering was

the first demonstrated method to achieve Si-based laser and amplifiers thanks to some Si properties such as a high optical damage threshold, excellent thermal conductivity, high refractive index and large Raman gain coefficient (approximately 10^3 – 10^4 larger than that of silica owing to its crystalline structure [48]). When a scattering medium is irradiated with two simultaneous beams (pump and signal), the first one (pump) excites the constituent molecules or atoms to a higher vibrational level, while the second one, resonant with a Stokes transition, triggers the generation of another Raman Stokes photon. Thus, amplification can be achieved. This technique, known as stimulated Raman scattering, has enabled the realization of Raman glass fiber amplifiers.

One of the best results has been obtained by Intel Corporation in 2007 [49] and it is shown in Fig. 1.15. The used structure consists of a ring resonator cavity with an optimized p-i-n diode structure to reduce free-carrier absorption (FCA) and two-photon absorption (TPA) coupled with a waveguide, as shown by the model in Fig. 1.15.a) and in the cross SEM in Fig. 1.15.b); the Raman generated lasing signal at 1545 nm, shown in Fig. 1.15.d) increases by increasing the pump power, by obtaining very low pump threshold (approximately 20 mW) with 50 mW output power.

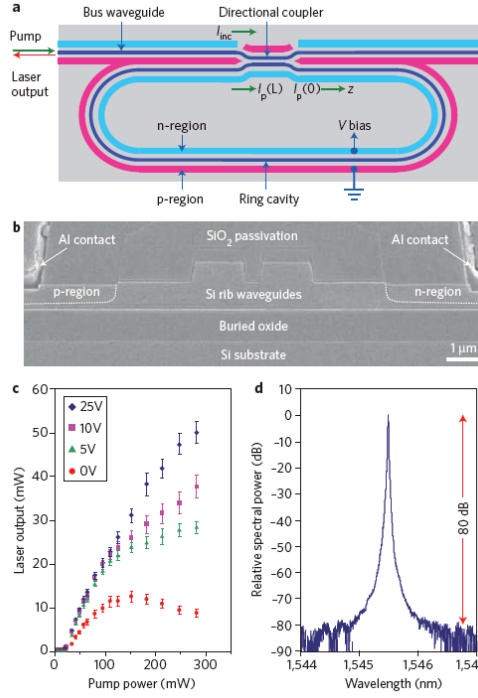


Figure 1.15. **a)** Schematic of the Raman laser consisting of a p-i-n junction device coupled with a ring cavity; **b)** cross-sectional SEM of the p-i-n junction; **c)** laser output power versus pump input power for different junction polarization; **d)** spectral power of the obtained Raman Si laser [49].

Another approach is the hybrid integration of III–V semiconductors [50] or Ge [51] gain medium within a Si platform for lasing. There are two main methods used for the hybrid integration: (i) epitaxial growth of crystalline semiconductors onto the silicon substrate and (ii) bonding of a full or partial wafer of a light-emitting semiconductor structure.

The first approach is mainly used for the Ge on Si. Ge emission probability is higher than the Si one since the energy mismatch between the two minima in the Ge conduction band, known as Γ valley and L valley, is small (0.134 eV). Several approaches have been studied to further reduce

this mismatch and increase the radiative emission [51]. Strain is the most promising one and it can be induced during its epitaxial growth on Si owing to the small mismatch between Si and Ge lattice parameters. In addition, it affects the Ge band structure by decreasing the energy difference between L and Γ valley as shown in Fig. 1.16.a)-c). A tuning of the emitted wavelength up to 2.3 μm has been demonstrated by increasing the strain: since for applications in telecommunication windows emission wavelengths in the range 1.4 μm and 1.6 μm are required, a lower strain (0.25%) is sufficient to obtain an intense emission and permits also to introduce a very low dislocation density useful for Ge lasers realization [52].

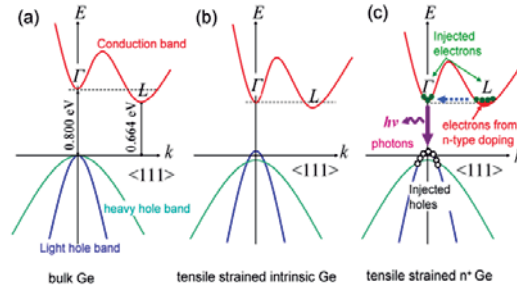


Figure 1.16. a) Schematic of Ge band diagram with evidenced transitions from L and Γ valley in the conduction band to the valence band. b) Strain influence and c) additional doping influence on Ge band diagram, permitting radiative transition [11].

Two of the newest results are shown in Fig. 1.17.a)-c). The first one is a LED made by a Ge p⁺/n⁺ junction on a Si substrate by which both PL and EL have been achieved [53], while the second one is a Ge on Si CW laser working at RT, optically [54] or electrically [55] stimulated. It consists in 1.6 $\mu\text{m} \times 0.5 \mu\text{m}$ doped Ge waveguide epitaxially grown on the Si substrate, thermally treated to introduce a tensile strain of 0.24% and coupled with a Fabry-Pérot cavity to enhance the emission from the direct gap. A cross-

sectional SEM picture of the Ge waveguide is shown in the bottom inset of Fig. 1.17.c). Emission through optical pumping with a 1064 nm Q-switched laser of 1.5 ns pulse duration is shown in the same figure.

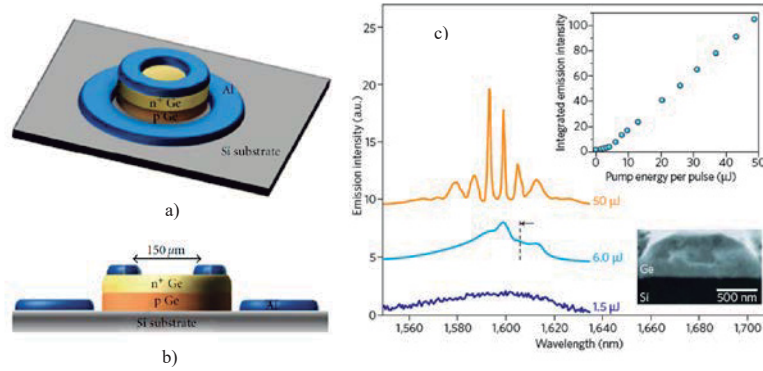


Figure 1.17. a) Isometric and b) cross section schematic of Ge-based light emitting diode [53]. c) Edge emission spectra of a Fabry-Pérot Ge waveguide under three different levels of optical pumping and the relative cross-section SEM image (bottom inset). The integral emission output versus pump power input is also shown [54].

Owing to the fact that the best emitting materials are in any case the direct band gap semiconductors, such as GaAs or InP, strong efforts have been devoted to the synthesis of these materials in Si but with scarce results, since the high lattice mismatch (120% and 77% respectively) introduces a high defects density. Nowadays the approach of wafer bonding already used for silicon-on-insulator (SOI) has been proposed also for other compound semiconductors in order to realize hybrid III–V lasers [50,56]. Therefore hybrid Fabry – Pérot lasers at RT [56] have been already fabricated for on-chip light sources. An electrically pumped compact micro-ring resonator laser with diameters varying between 15–50 μm [57] is shown in Fig. 1.18 with the correspondent cross-sectional SEM image reported in the left inset.

Low CW thresholds, about 4 mA, with reasonable output powers (3.5 mW) have been observed in devices with diameters of 50 μm [57]. Further reducing the laser diameter will result in a drastic reduction in the threshold. Thanks to the dimension reduction, the fabrication of millions of micro-ring lasers on a single Si wafer is now possible.

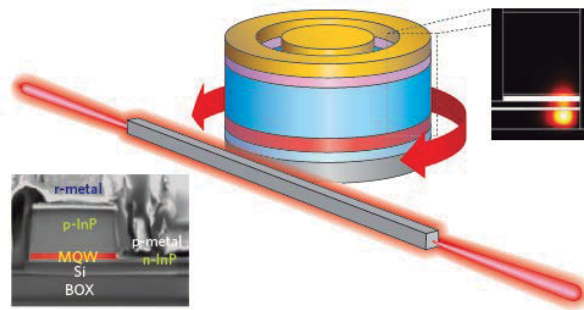


Figure 1.18. Schematic of a hybrid micro-ring laser with a Si bus waveguide. In the left inset a cross-sectional SEM of the microring laser is shown; in the right inset an expanded view of the transverse electric mode is reported [57].

1.3. Silicon compatible materials for active photonic devices in the infrared wavelengths

The importance of Si-based light sources in the visible range for lighting and displays and in the infrared range for telecommunication relies mostly in the possibility to realize integrated active devices on Si platforms. For example, Er doped materials for infrared emission are strongly suitable as active media in Si passive components, as Si optical waveguides, in order to realize active devices as optical amplifiers. The most important passive components and their coupling with optically active materials will be discussed in the following sections.

1.3.1. Silicon passive waveguides for planar optical amplifiers

Among the passive Si-based components used to transport light from a point to another, optical waveguides are the most common, owing to the light confinement obtained within a high refractive index zone (core) surrounded by a lower refractive index one (cladding) due to the total internal reflection phenomenon. The evolution in the synthesis of waveguides fully compatible with the standard Si technology for microphotonics has brought nowadays to innovative solutions, such as SOI waveguides, photonic crystals and plasmonic waveguides.

Owing to the high difference in refractive index between silicon (3.45) and silica (1.45), in SOI waveguides it is possible to scale down the size of the waveguide modes in ultra-compact dimensions (approximately $0.1 \mu\text{m}^2$) thus allowing a large number of optical components integrated in the same chip, as required by the CMOS technology. However, as devices are downsized, deviations from ideal profiles in fabrication (as sidewall roughness) will become prominent and will result in scattering at the interfaces between waveguide core and cladding, which becomes a major source of propagation losses [12]. The most common structures are the channel waveguides, where the guiding layer is completely embedded in the cladding, and the ridge waveguides, where the guiding layer consist of a slab with a dielectric ridge on top embedded between two layers having low refractive index. Even if the scattering losses, typically around 0.2–3.0 dB/cm, can be lowered by reducing the layers roughness through oxidation of the waveguide sidewalls, new types of passive devices are being developed.

Among them, photonic crystals (PhCs) are probably one of the most important developments of the last decades for applications in Si microphotonics. In particular 2D PhCs slabs on high-quality SOI substrates have been optimized by realizing a structure in which region of high (typically Si) and low (typically air) refractive index dielectrics are periodically alternated, creating an optical lattice. As the periodical structure of crystals is characterized by permitted and forbidden electronic states, the same is obtained for light [58]: there is indeed a spectral range of wavelengths that cannot propagate in the crystal and that is reflected in the vertical direction (photonic band gap, PBG). In addition, as introducing defects in a crystal generates permitted electron states inside the band gap, breaking the symmetry of a PhCs structure by introducing defects (such as removing holes or changing their dimensions or their periodicity parameters) permits the propagation of light at a certain frequency. This is in particular true if an entire line of holes is removed, determining the creation of a channel waveguide [59] in which light is forced to propagate. Due to the high confinement, PhC waveguides can shrink light in dimension smaller than $0.15\text{ }\mu\text{m}$.

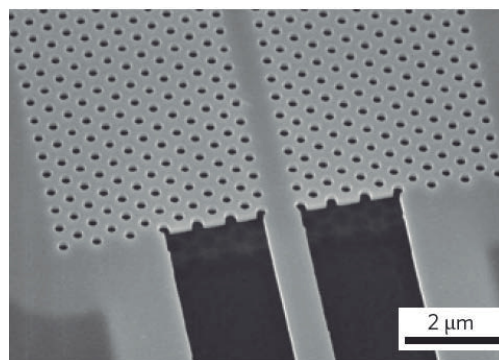


Figure 1.19. Scanning electron microscope (SEM) image of a PhC waveguide etched in a thin silicon membrane and connected to a tapered ridge waveguide [60].

As an example, a PhC waveguide etched in a thin silicon membrane and connected to a tapered ridge waveguide is shown in Fig. 1.19 [60].

Another interesting and more recent approach proposed to further squeeze the light confinement is the exploiting of plasmonic. Indeed photonic devices suffer from the diffraction limit, i.e. the minimum reachable size cannot be lower than half wavelength of the involved photon. This induces a big difference in the physical sizes of the electronic and photonic components (about two orders of magnitude) of PICs. Although gratings and inverted taper could solve this problem [11,12], the creation of sub-wavelength oscillating modes obtained by coupling the incoming photons with the metal free-electron gas (plasmonic oscillations) [61] could merge the high performances offered by photonics and the nano-scale integration offered by electronics in a single element. In particular, surface plasmon polaritons (SPP) are electrons oscillations propagating on an metal/insulator interface, strongly confined in the perpendicular direction up to some nm (two orders of magnitude lower than the typical confinement obtained in the standard photonic waveguides) and then characterized by higher electromagnetic fields. The applications of SPP in photonics could be then very useful in order to guide and manipulate optical signals in PICs. A wide variety of plasmonic waveguide designs have been investigated for the general purpose of on-chip communication [62,63]. Figure 1.20 provides an overview of some of them, which are all capable of strong optical confinement with manageable propagation losses. The simplest plasmonic waveguides are constituted by a metal strip surrounded by two insulators (dielectrics) known as an insulator-metal-insulator (IMI) plasmonic waveguide, shown in Fig. 1.20.a); the inverse metal-insulator-metal structure (MIM), shown in Fig. 1.20.b), has also been investigated. The combination

of dielectric and plasmonic waveguide principles has attracted a lot of attention from researchers; for example, a dielectric strip placed on a metal plane (dielectric loaded SPP waveguides, DLSPP), shown in Fig. 1.20.c), yields a better plasmonic confinement perpendicular to the surface with respect to IMI and MIM structures but similar SPPs propagation lengths. This is considered a general limit for dielectric plasmon-based waveguides in the visible and infrared ranges, because the propagation losses of SPPs waveguides increase with the cubed refractive index of the adjacent dielectric, owing to the increase of electron-electron and electron-phonon interactions and of the scattering with defects or bounding. In addition, metals themselves are plagued by large losses, especially in the visible and ultra-violet (UV) spectral ranges, arising in part from inter-band electronic transitions, that are detrimental for the performances of the plasmonic devices, seriously limiting the feasibility of many plasmonic applications. In addition, the synthesis of metals is not compatible with the Si standard technology and thus is unpractical for applications in an integrated device.

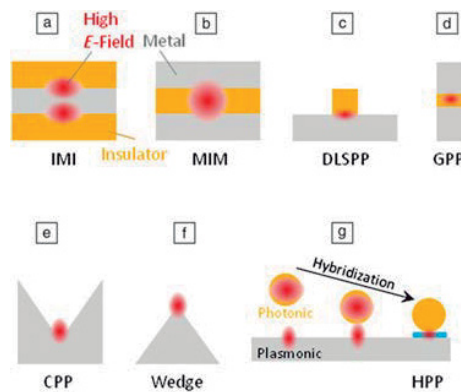


Figure 1.20. Surface plasmon waveguide cross-section architectures, with the optical data propagating in the third dimension. **a)** IMI; **b)** MIM; **c)** DLSPP; **d)** gap plasmon polariton (GPP); **e)** channel plasmon polariton (CPP); **f)** wedge SPP and **g)** hybrid plasmon polariton (HPP) [62].

In an attempt to mitigate material losses, recently different approaches have been proposed. One of the nicest example is the realization of hybrid plasmon polariton (HPP) devices, shown in Fig. 1.20.g), in which a thin oxide gap is inserted as a separation between the dielectric core and the metal layer, which pulls the optical modes into the nanometer gap layer [64].

Recently a new strategy is emerging, the use of alternative plasmonic materials such as transparent conductive oxides (TCO) or nitrides in place of metals. Negative dielectric function characterizes the TCO in the infrared range and the nitrides in the visible one [65]. The comparison between the real and imaginary part of the dielectric functions of these alternative plasmonic materials and the standard metals, Au and Ag, is reported in Fig. 1.21. While the real part determines the range in which the material has a plasmonic behaviour ($\epsilon' < 0$), the imaginary part (ϵ'') is strictly connected with losses.

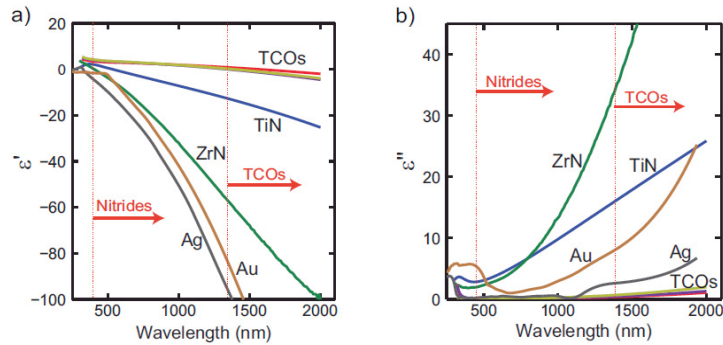


Figure 1.21. Comparison of the optical constants of TiN, ZrN and TCOs thin films with the ones of gold and silver. The arrows show the wavelength ranges in which nitrides and TCOs are metallic. **a)** From ϵ' versus wavelengths it is shown the optical range where TCOs and nitrides have smaller negative permittivity values than metals, while in **b)** the relative losses are compared [65].

By this comparison it is possible to deduce that these innovative materials behave as metals regarding the plasmonic properties, but completely reducing the losses and their optimization as waveguides in PICs could give a great performances improvement.

1.3.2. Enhanced light emission from active devices

All the above described examples are related to passive devices. However it is possible to couple them with emitting elements in order to make them active. This point has important applications, as the realization of optical planar amplifiers or light sources, from LED to many LASER prototypes.

In addition to the already widely known examples of Er-doped waveguides made of Si compatible materials as Al_2O_3 , SiO_2 , ZnO and Si-nc in SiO_2 , innovative examples regard the emission and amplification of IR light in PhCs. Photonic band structures and PBGs can improve mainly extraction (η_{extr}) and collection efficiency (η_{coll}) of photonic devices. Owing to these improvements, the possibility to control and enhance the light emitted by crystalline Si has been demonstrated [66]. The device schematically shown in Fig. 1.22.a) consists of a PhC structure patterned in a p-i-n junction formed into the top 200-nm-thick Si layer by area-selective implantations of boron and phosphorous ions, as shown by the SEM image of the central part in the zoom of Fig. 1.22.a). The device EL intensity, shown in the inset of Fig. 1.22.b), increases by increasing the PhC period (a), defined as the distance between two holes, reaching enhancement of about 14 times with respect to the un-patterned device. This enhancement is

mainly caused by the improvement of η_{extr} and η_{coll} due to the photonic band structures.

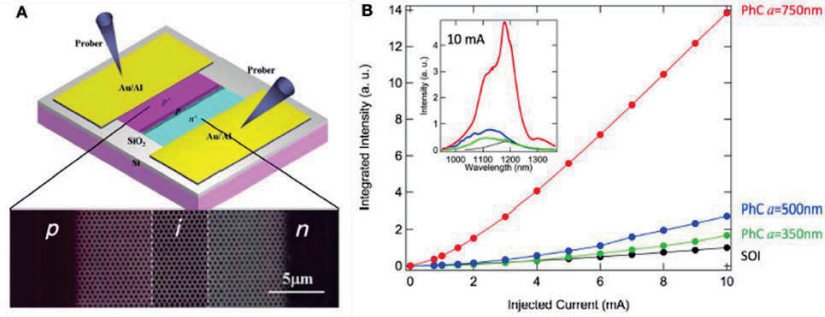


Figure 1.22. a) Schematic representation of a Si PhC LED. The SEM image shows the center area of the device. b) Integrated EL intensities for various periods a . The inset shows the corresponding EL spectra at 10mA [66].

Another interesting proposed structure that can be coupled with emitting materials is the PhC nanocavity, realized by removing one or more holes in the periodic structure. This creates localized modes in the xy plane having frequency in the forbidden band gap that however cannot propagate in the rest of the crystal. Because the electromagnetic field intensity and the light–matter interactions in an optical cavity scale as its Q/V ratio, with Q being the quality factor (the energy loss per cycle divided by the energy stored inside) and V its modal volume (measure of the spatial extent and energy density of the mode), the request for PhC nanocavities with a high Q/V ratio is intense. State-of-the-art Si PhC cavities feature Q values higher than 4×10^6 while keeping modal volumes below $(\lambda/n)^3$, where n is the effective index of the cavity mode [67]. Therefore they allow to strongly reduce the dimension of the cavity, without suffering from scattering losses. These values are comparable with the ones obtained in micrometric ring-

resonators [68] that however have much bigger sizes; in addition PhC nanocavities performances are increasing constantly with the improvements in silicon nanofabrication.

An example of enhanced emission by PhC nanocavity is shown in Fig. 1.23. In this case, optically active defects have been introduced directly into a silicon high-Q PhC nanocavity using a simple hydrogen plasma treatment, visible in the plan view SEM image in Fig. 1.23.a) by dark dots [69]. Although the Si defects luminescence notoriously quenches very quickly with temperature, the coupling with a PhC nanocavity can suppress this quenching and enhance light emission by more than four orders of magnitude relative to bulk Si [69], as shown in Fig. 1.23.b). Based on this surprising result, an electrically driven CW nano-LED source was also realized [69] at RT and it exhibits a narrow linewidth in the important technological wavelength window between 1.3–1.6 μm , tunable by the periodicity parameter a of the PhC cavity.

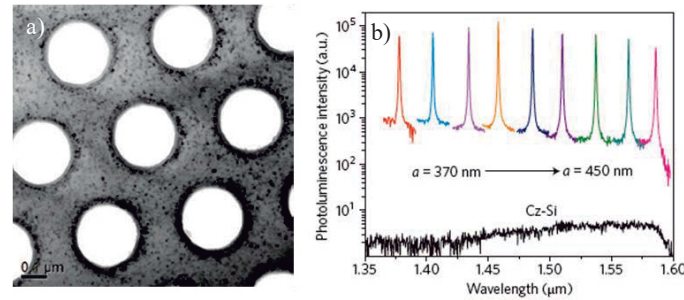


Figure 1.23. Silicon PhC nanocavity emitting at sub-bandgap wavelengths. **a)** TEM image of the structure, showing with black dots the active defects created by hydrogen plasma treatment and **b)** emission lines of the fundamental cavity modes by varying a , four orders of magnitude higher than that of bulk Si [69].

Based on the above result, the applications of PhC nanocavities are growing considerably in the last years. In particular, the control of the

spontaneous emission rate by the light extraction due to the PBG [70] and by Purcell effect has been demonstrated to interestingly enhance the spontaneous emission intensity of an atom or a quantum dot located inside the cavity [71]. For this reason, this effect has been proposed to increase optical efficiency of Er-doped systems for infrared amplifiers. As an example, Fig. 1.24 reports the coupling between a Si PhC cavity and a very thin layer of Y-Er disilicate film [72], as shown in the cross-section view in Fig. 1.24.a). In order to obtain the highest quality factor Q and to tune the cavity resonance at around $1.54 \mu\text{m}$, the cavity parameters have been optimized by shifting the holes, as shown in Fig. 1.24.b), thus matching perfectly with Er emission, shown in Fig. 1.24.c). In addition, Er PL enhancement of about two orders of magnitude has been estimated by the peak-to-background ratios in Fig. 1.24.d) for all the investigated samples, owing to the increased extraction efficiency and the Purcell effect.

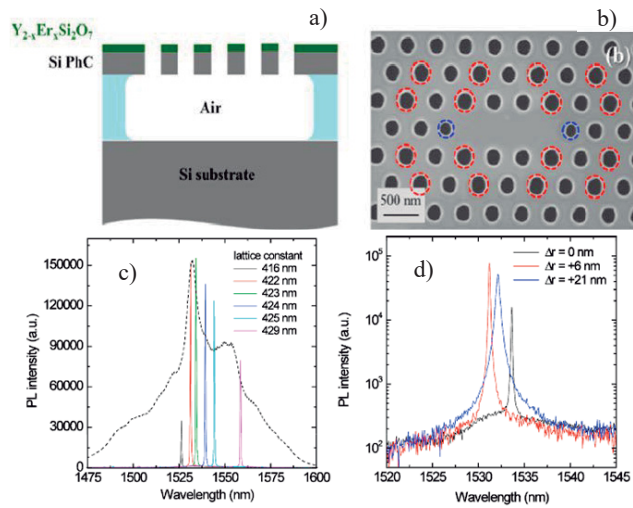


Figure 1.24. a) Cross-section scheme of the top-coated Si PhC membrane after the Y-Er disilicate deposition and relative b) plan view SEM image; c)-d) PL emission from the top-coated cavities by varying the PhC nanocavity parameters. The dashed black line reports the typical shape of Er emission in Y-Er disilicate film [72].

By engineering these systems, also LEDs operating in the IR have been demonstrated [73]. As an example the coupling between a slot waveguide covered by an Er-doped SiO_2 thin layer containing Si-nc as emitting material and a PhC structure is shown in Fig. 1.25.a), with a detailed zoom on the PhC region in Fig. 1.25.b). Thanks to the photonic structure, when the device is biased with an external direct voltage source, the Er emission in the vertical direction is 3-fold increased. The device EL at RT was investigated by EmMi, as shown Fig. 1.25.c) in false colors.

In this way it has been demonstrated that the use of PhCs and the combination of optimized emitting materials, as Er-doped ones, is a very encouraging step towards the realization of all-silicon-based light sources.

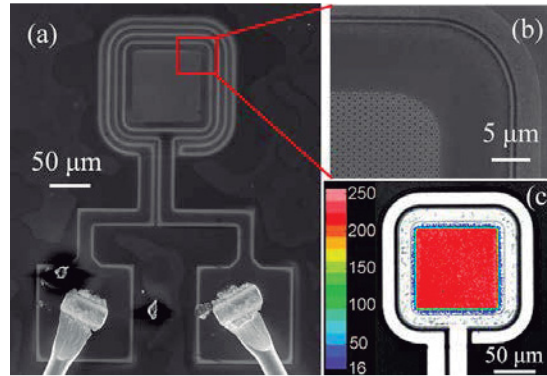


Figure 1.25. **a)** Top-view SEM image of the PhCs structure coupled with a slot waveguides covered by an Er containing emitting layer. **b)** Detailed SEM image of the top-right part of the device, highlighting the patterned PhC. **c)** EmMi image of one device under forward polarization; the image is in false colors [73].

1.4. Contents and motivations of this thesis

From the above mentioned results, it is clear that the research on Si-based optical light sources is still moving on, with the aim to integrate these

components in microphotonic devices useful not only for displays and lab-on-chip applications but also for telecommunications, where microphotonic circuits can be employed as substitutes of electronic parts in our day-life accessories. In order to do that, a further improvement of the materials performances and a further development of new Si-based devices are required. Aim of this thesis work is hence to synthesize and characterize novel materials that can be introduced in the Si microphotronics scenario.

In **Chapter 2**, the needs of new light sources in the visible range will be faced. Bismuth, belonging to post-transition metals, is proposed as an emitter for Si-based transparent materials in place of the most common used REs, as Eu and Tb: this element indeed can improve much more the optical efficiency of the systems thanks to its peculiar electronic configuration and to its high absorption and emission cross sections. After a brief introduction of its potentiality as a visible emitter in glass and crystalline hosts and of the open points regarding the application in Si-based materials, its introduction in two different Si-compatible yttrium based hosts, the yttrium disilicate and the yttrium oxide, will be discussed. These matrices are indeed suitable for the introduction of dopant elements in the Y^{3+} substitutional position. In particular, the influence of different annealing atmospheres on the structural and optical properties will be presented for both the hosts, thus proposing them as efficient, Si compatible optical materials for applications on Si platforms as down-converters for the solar spectrum and as broad and tuneable emitters in the visible range.

In **Chapter 3**, the possibility to exploit also infrared emission by involving erbium-yttrium mixed compounds will be addressed. This approach permits to increase the Er content up to the constituent level (10^{22} at/cm³) without optically inactive clusters formation and to control the Er-Er

interactions by controlling accurately the Er-Er mean distances, thus increasing the efficiency of the system. A further interesting approach that will be illustrated is the possibility to introduce Bi as a sensitizer for Er. Therefore by the optimization of the structural and optical properties, the coupling Bi-Er will be proposed in order to enhance Er optical emission at 1.54 μm up to 2000 times. This result makes Bi-Er-Y mixed compounds good candidates for light emission and amplification in the telecommunication windows, thus achieving an interesting goal for Si-microphotonics.

References

- [1].B. Jalali, *J. Lightwave Tech.* **24**, 4600 (2006).
- [2].G. E. More, *Electronics* **38** (1965).
- [3].D. Brock, C. Lécuyer, *Makers of the Microchip: A Documentary History of Fairchild Semiconductor* (MIT press, 2010).
- [4].Website: www.intel.com
- [5].<http://www.itrs.net>
- [6].H. Iwai, *Solid State Electron.* **48**, 497 (2004).
- [7].L. C. Kimerling, *Appl. Surf. Sci.* **159**, 8 (2000).
- [8].B. Jalali, S. Fathpour, K. Tsia, *Green Silicon Photonics*, Optics and Photonics News (2009).
- [9].C. Gunn, *Micro IEEE* **26**, 58 (2006).
- [10]. M. Paniccia, S. Koehl, "The silicon solution", *Spectrum IEEE*, **42**, 38 (2005).
- [11]. W. N. Ye, Y. Xiong, *Journal of Modern Optics* **60**, 1299 (2013).
- [12]. Z. Fang, C. Z. Zhao, *ISRN Optics* **2012**, 27 (2012).
- [13]. Intel Labs, "The 50G Silicon Photonics Link" (2010); <http://www.intel.com>
- [14]. Q. Xu. B. Schmidt, S. Pradhan, M. Lipson, *Nature* **435**, 325 (2005).
- [15]. L. Colace, G. Masini, G. Assanto, *IEEE J. Quantum Electron.* **35**, 1843 (1999).

- [16]. L. Rebohle, T. Gebel, R. A. Yankov, T. Trautmann, W. Skorupa, J. Sun, G. Gauglitz, R. Frank, *Optical Materials* **27**, 1055 (2005).
- [17]. K. D. Hirschman, L. Tsybeskov, S. P. Duttagupta, P. M. Fauchet, *Nature* **384**, 338 (1996).
- [18]. U. Lafont, H. van Zeijl, S. van der Zwaag, *Microelectronics Reliability* **52**, 71 (2012).
- [19]. M. G. Craford, *LEDs for Solid State Lighting and Other Emerging Applications: Status, trends and challenges, Proc. of SPIE* **5941** (2005).
- [20]. M. G. Craford, *Innovation in LEDs*, 2015 DOE Solid-State Lighting R&D Workshop.
- [21]. Y. Fan, M. Rose, in *Handbook of Visual Display Technology* (Springer Berlin Heidelberg, 2012), pp. 1071.
- [22]. L. Ozawa, *Cathodoluminescence and Photoluminescence: Theories and Practical Applications* (CRC press 2007).
- [23]. L. E. Shea, *The Electrochemical Society Interface* **7**, 24 (1998).
- [24]. F. Priolo, T. Gregorkiewicz, M. Galli, T. F. Krauss, *Nat. Nanotech.* **9**, 19 (2014).
- [25]. E. Froner, R. Adamo, Z. Gaburro, B. Margesin, L. Pavesi, A. Rigo, M. Scarpa, *J. Nanoparticle Res.* **8**, 1071 (2006).
- [26]. M. S. Hybertsen, *Phys. Rev. Lett.* **72**, 1514 (1994)
- [27]. D. Jurbegs, E. Rogojina, L. Mangolini, U. Kortshagen, *Appl. Phys. Lett.* **88**, 233116 (2006)
- [28]. L. T. Canham, *Appl. Phys. Lett.* **57**, 1046 (1990).
- [29]. R. D. Tilley, J. H. Warner, K. Yamamoto, I. Matsui, H. Fujimori, *Chem. Commun.* **14**, 1833 (2005).
- [30]. N. Daldosso, M. Luppi, S. Ossicini, E. Degoli, R. Magri, G. Dalba, P. Fornasini, R. Grisenti, F. Rocca, L. Pavesi, S. Boninelli, F. Priolo, C. Spinella, F. Iacona, *Phys. Rev. B* **68**, 085327 (2003).
- [31]. W. D. A. M. de Boer, D. Timmerman, K. Dohnalova, I. N. Yassievich, H. Zhang, W. J. Buma, T. Gregorkiewicz, *Nature Nanotech.* **5**, 878 (2010).

-
- [32]. V. Schmidt, J. V. Wittemann, S. Senz, U. Gösele, *Adv. Mater.* **21**, 2681 (2009).
- [33]. A. Irrera, P. Artoni, F. Iacona, E. F. Pecora, G. Franzò, M. Galli, B. Fazio, S. Boninelli, F. Priolo, *Nanotechnology* **23**, 075204 (2012).
- [34]. G. Franzò, A. Irrera, E. C. Moreira, M. Miritello, F. Iacona, D. Sanfilippo, G. Di Stefano, P. G. Fallica, F. Priolo, *Appl Phys A* **74**, 1 (2002).
- [35]. G. Liu, X. Chen, *Handbook on the physics and chemistry of rare earths* (Elsevier B.V. Amsterdam, 2007).
- [36]. L. Rebohle, W. Skorupa, *Rare earths implanted MOS devices for silicon photonics* (Springer Berlin, 2010).
- [37]. J. M. Sun, S. Prucnal, W. Skorupa, T. Dekorsy, A. Mücklich, M. Helm, L. Rebohle, T. Gebel, *J. Appl. Phys.* **99**, 103102 (2006).
- [38]. S. Prucnal, J. M. Sun, W. Skorupa, M. Helm, *Appl. Phys. Lett.* **90**, 181121 (2007).
- [39]. A. Polman, *J. Appl. Phys.* **82**, 1 (1997).
- [40]. E. Snoeks, P.G. Kik, A. Polman, *Opt. Mater.* **5**, 159 (1996).
- [41]. W. Ge, X. R. Zhang, M. Liu, Z. W. Lei, R. J. Knize, Y. Lu, *Theranostics* **3**, 282 (2013).
- [42]. G. Franzò, V. Vinciguerra, F. Priolo, *Appl. Phys. A: Mater. Sci. Process.* **69**, 3 (1999).
- [43]. P. G. Kik, A. Polman, in *Towards the First Silicon Laser* (Springer Netherlands, 2003), Vol. 93, pp. 383.
- [44]. C. E. Chryssou, A. J. Kenyon, C.W. Pitt, *Mater. Sci. Eng. B* **81**, 16 (2001).
- [45]. W. J. Miniscalco, *J. Lightw. Technol.* **9**, 234 (1991).
- [46]. N. Daldosso, L. Pavesi, *Laser & Photon. Rev.* **3**, 508 (2009).
- [47]. B. Garrido, C. García, S.-Y. Seo, P. Pellegrino, D. Navarro-Urrios, N. Daldosso, L. Pavesi, F. Gourbilleau, R. Rizk, *Phys. Rev. B* **76**, 245308 (2007).
- [48]. D. Liang, J. E. Bowers, *Nat. Photon.* **4**, 511 (2010).
- [49]. H. Rong, S. Xu, Y.-H. Kuo, V. Sih, O. Cohen, O. Raday, M. Paniccia, *Nat. Photon.* **1**, 232 (2007).
- [50]. H. Park, A. W. Fang, S. Kodama, J. E. Bowers, *Opt. Express* **13**, 9460 (2005).

- [51]. J. Liu, X. Sun, D. Pan, X. Wang, L. C. Kimerling, T. L. Koch, J. Michel, *Opt. Express* **15**, 11272 (2007).
- [52]. J. Liu, D. D. Cannon, K. Wada, Y. Ishikawa, S. Jongthammanurak, D. T. Danielson, J. Michel, L. C. Kimerling, *Appl. Phys. Lett.* **84**, 660 (2004).
- [53]. S.-L. Cheng, J. Lu, G. Shambat, H.-Y. Yu, K. Saraswat, J. Vuckovic, Y. Nishi, *Opt. Express* **17**, 10019 (2009).
- [54]. J. Liu, X. Sun, R. Camacho-Aguilera, L. C. Kimerling, J. Michel, *Opt. Lett.* **35**, 679 (2010).
- [55]. R. E. Camacho-Aguilera, Y. Cai, N. Patel, J. T. Bessette, M. Romagnoli, L. C. Kimerling, J. Michel, *Opt. Express* **20**, 11316 (2012).
- [56]. G. Roelkens, D. V. Thourhout, R. Baets, R. Nötzel, M. Smit, *Opt. Express* **14**, 8154 (2006).
- [57]. D. Liang, M. Fiorentino, T. Okumura, H.-H. Chang, D. T. Spencer, Y.-H. Kuo, A. W. Fang, D. Dai, R. G. Beausoleil, J. E. Bowers, *Opt. Express* **17**, 20355 (2009).
- [58]. J. D. Joannopoulos, S. G. Johnson, J. N. Winn, R. D. Meade, *Photonic crystals: Molding the Flow of Light* (Princeton Univ. Press, 1995).
- [59]. S. McNab, N. Moll, Y. Vlasov, *Opt. Express* **11**, 2927 (2003).
- [60]. B. Corcoran, C. Monat, C. Grillet, D. J. Moss, B. J. Eggleton, T. P. White, L. O'Faolain, T. F. Krauss, *Nat. Photon.* **3**, 206 (2009).
- [61]. R. Zia, J. A. Schuller, A. Chandran, M. L. Brongersma, *Materials Today* **9**, 20 (2006).
- [62]. V. J. Sorger, R. F. Oulton, R.-M. Ma, X. Zhang, *MRS Bulletin* **37**, 728 (2012).
- [63]. D. K. Gramotnev, S. I. Bozhevolnyi, *Nat. Photon.* **4**, 83 (2010).
- [64]. R. F. Oulton, V. J. Sorger, D. A. Genov, D. F. P. Pile, X. Zhang, *Nat. Photon.* **2**, 496 (2008).
- [65]. G. V. Naik, J. Kim and A. Boltasseva, *Opt. Mater. Express* **1**, 1090 (2011).
- [66]. S. Iwamoto, Y. Arakawa, *IEICE Trans. Electron.* **E95-C**, 206 (2012).
- [67]. Y. Taguchi, Y. Takahashi, Y. Sato, T. Asano, S. Noda, *Opt. Express* **19**, 11916 (2011).

- [68]. D. K. Armani, T. J. Kippenberg, S. M. Spillane, K. J. Vahala, *Nature* **421**, 925 (2003).
- [69]. A. Shakoor, R. Lo Savio, P. Cardile, S. L. Portalupi, D. Gerace, K. Welna, S. Boninelli, G. Franzò, F. Priolo, T. F. Krauss, M. Galli, L. O'Faolain, *Laser & Photonics Reviews* **7**, 114 (2013).
- [70]. S. Noda, M. Fujita, T. Asano, *Nat. Photon.* **1**, 449 (2007).
- [71]. E. M. Purcell, *Phys. Rev.* **69**, 681 (1946).
- [72]. R. Lo Savio, M. Miritello, A. Shakoor, P. Cardile, K. Welna, L. C. Andreani, D. Gerace, T. F. Krauss, L. O'Faolain, F. Priolo, M. Galli, *Opt. Express* **21**, 10278 (2013).
- [73]. R. Lo Savio, M. Galli, M. Liscidini, L. C. Andreani, G. Franzò, F. Iacona, M. Miritello, A. Irrera, D. Sanfilippo, A. Piana, F. Priolo, *Appl. Phys. Lett.* **104**, 121107 (2014).

“To raise new questions, new possibilities, to regard old problems from a new angle, requires creative imagination and marks real advance in science.[...] Logic will get you from A to B. Imagination will take you everywhere.”

“Sollevare nuove domande, nuove possibilità, riguardare vecchi problemi da un nuovo angolo, richiede immaginazione e segna un reale avanzamento della scienza.
[...] La logica ti può portare da A a B.
L’immaginazione invece ti può portare ovunque.”

Albert Einstein

Chapter 2: Bismuth-doped silicon compatible thin films for visible emission

As extensively discussed in chapter 1, the increasing demand for Si compatible light sources has required the investigation of a wide variety of materials, such as Si nanostructures or rare earths (REs) doped materials. In this scenario, heavier main group elements have been recently proposed as alternative emitters. Hence chapter 2 will be focused on the introduction of bismuth in silicon based thin films as an emerging visible emitter for possible applications such as an integrated light source device for microphotonics.

Yttrium disilicate and yttrium oxide thin films have been chosen as hosts for Bi ions owing to their transparency in the whole visible and infrared ranges and their compatibility with the standard Si-microelectronics technology. Undoped thin films have been synthesized by RF magnetron co-sputtering and Bi was introduced by ion implantation processes. The influence of different annealing treatments (in N₂ or O₂) on the structural and optical properties will be extensively discussed in this chapter.

Even if the annealing temperature of 1000°C is not sufficient to permit a total crystallization of the Bi-doped yttrium disilicate thin films, this temperature is already high enough to induce the precipitation of some Bi ions in metallic clusters, as shown by TEM analyses. In addition the presence of two broad emissions in the blue (O₂) and in the orange/red (N₂) spectral ranges was demonstrated by the optical characterization. They have been ascribed to the stabilization of the dissolved Bi ions in two different oxidation states, namely Bi³⁺ and Bi²⁺.

Instead Bi-doped yttrium oxide thin films were demonstrated to be polycrystalline already after the deposition. Moreover an accurate study of the structural properties have permitted to demonstrate that Bi³⁺ is the only oxidation state present. In addition, two Bi³⁺ broad and intense emissions in the blue and in the green spectral ranges have been recorded under a

selective UV excitation, due to the presence of two possible cation lattice sites. Finally a three level scheme was employed to model the Bi excitation and de-excitation processes, validated by optical measurements at cryogenic temperatures. On the basis of their chemical and optical properties, Bi-doped Y disilicate and oxide thin films can be considered potential materials for Si microphotonic applications.

2.1. Bismuth as an emerging efficient emitter

Bismuth is the heaviest stable element of the periodic table. Since its electronic configuration is $[\text{Xe}]-4f^{14}5d^{10}6s^26p^3$, it can be found in different oxidation states, from 0 to +5. One of the most interesting feature of all its oxidation states is that they are all optically active with peculiar broad absorption and emission bands spread from the ultraviolet (UV) to the infrared (IR). For this reason it has gained the appellation of “wonder metal” and the researchers interest on its optical properties is abruptly increased in the last ten years, as represented by the statistics in Fig. 2.1 related to the number of ISI publications per year having “bismuth luminescence” as keyword.

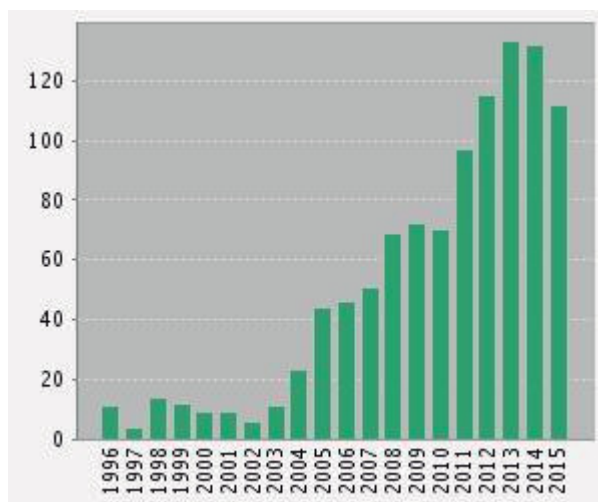


Figure 2.1. Number of publications per year having the keyword “bismuth luminescence” in the last 20 years. The diagram is taken from [1].

The stabilization of its different oxidation states depends strongly on the chemical environment of its host, but the most common found for visible

emission for lighting, field emitting displays (FEDs) and light emitting devices (LEDs) are the Bi^{3+} and Bi^{2+} oxidation states.

2.1.1. Tuneable emission range controlled by the Bi oxidation state

The spectroscopy of Bi^{3+} ions, which has the $6s^2$ electronic configuration, has been extensively investigated in a variety of host lattices, from crystalline matrices to glasses. The ground state of the free ion is $^1\text{S}_0$, whereas the $6s6p$ excited states give rise to the triplet levels [$^3\text{P}_0$, $^3\text{P}_1$, $^3\text{P}_2$] and the $^1\text{P}_1$ singlet state as shown by the potential energy diagram in configurational coordinate reported in the inset of Fig. 2.2.a). The allowed transitions are $^1\text{S}_0 \rightarrow ^1\text{P}_1$, typically around 230 nm, and $^1\text{S}_0 \rightarrow ^3\text{P}_1$, in the range of 250–400 nm. Instead, the $^1\text{S}_0 \rightarrow ^3\text{P}_0$ and the $^1\text{S}_0 \rightarrow ^3\text{P}_2$ transitions are normally forbidden, but become partially allowed only if coupled with asymmetrical lattice vibrational modes. Since the minimum of the excited state potential is always shifted relative to the one of the ground state $^1\text{S}_0$, a shift between the correspondent broad emission and excitation band is expected (the so called Stokes shift) [2].

About the energetic positions of the excited states, they strongly depend on the local field felt by Bi ions, and therefore by the embedding host. As an example, Fig. 2.2.a) reports the Bi^{3+} spectroscopy in $\text{Y}_3\text{Ga}_2\text{O}_{12}$ single crystal [3], widely used as REs host for solid state lasers, up-converters and scintillators. The excitation spectrum, curve (c), and the emission spectra at 80 K, curve (d), and at 141 K, curve (e), can be associated to the $^3\text{P}_1 \rightarrow ^1\text{S}_0$ transition. By changing the host the emission peak, associated to the same transition, shifts, as for the borate glass [4] shown in

Fig. 2.2.b), where it appears shifted at 430 nm instead of 320 nm. By varying the concentration of alkali ions (Na_2O) in the same host, further shifts of both the excitation and the emission bands are also visible, due to the modification of the host covalence and consequently to the energetic positions of the $^3\text{P}_1$ bands [4]. This spectroscopic behaviour is extensively reported for different Bi-doped crystalline phosphors [5] and glasses [6,7].

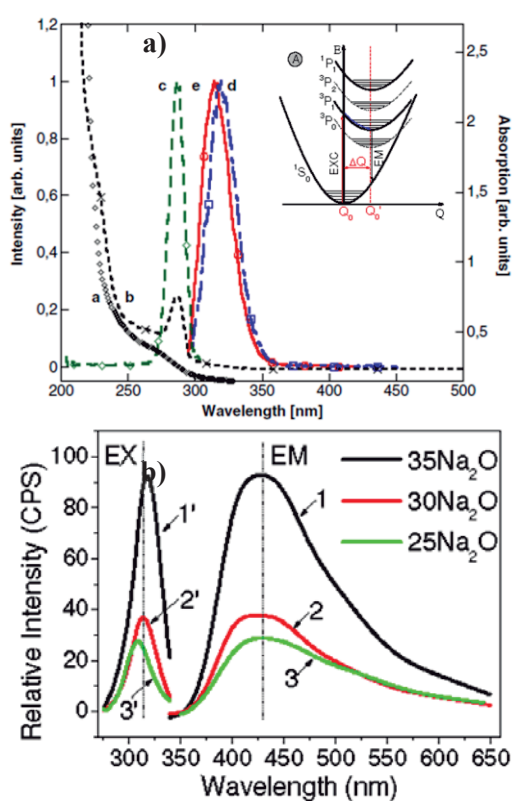


Figure 2.2.a) Absorption bands of undoped single crystal $\text{Y}_3\text{Ga}_2\text{O}_{12}$, curve (a), and Bi^{3+} doped $\text{Y}_3\text{Ga}_2\text{O}_{12}$, curve (b), excitation bands (curve c) and emission spectra at 80 K (curve d) and 141 K (curve e) [3]. In the inset, the configurational coordinate diagram of Bi^{3+} ion [4]. **b)** Excitation and emission spectra of Bi^{3+} doped borate glasses with different contents of alkali ions (Na_2O) [4].

In addition to this blue-green emission band, associated to Bi^{3+} ions, it is interesting to note that a narrow orange band was also reported in synthetic $\text{Bi}:\text{BaSO}_4$ for the first time in 1886 [8], but for a long time its origin was not clear. A century later a convincing interpretation has been done by *Hamstra et al.* [9] that associated this luminescence to Bi^{2+} ions. More recent studies clearly revealed that a visible emission in the orange-red range is associable to Bi^{2+} ions and it is widely found in different hosts such as crystalline SrB_4O_7 [10], $\text{SrB}_6\text{O}_{10}$ [11], $\text{M}^{2+}\text{BPO}_5$ ($\text{M} = \text{Ba}, \text{Sr}, \text{Ca}$) [12], and $\text{Sr}_2\text{P}_2\text{O}_7$ [13]. As examples, the spectroscopies of Bi^{2+} ions in $\text{SrB}_6\text{O}_{10}$ (upper spectra) and in SrB_4O_7 (lower spectra) [11] are shown in Fig. 2.3.a).

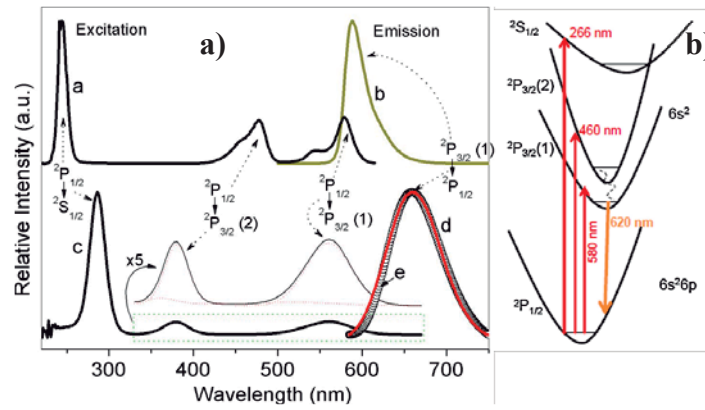


Figure 2.3. a) Bi^{2+} red emission and excitation spectrum from $\text{SrB}_6\text{O}_{10}$ (upper spectra) and SrB_4O_7 (lower spectra) [11]. The involved transitions are also indicated. b) Configurational coordinate diagram of Bi^{2+} ion [14].

The emission spectra can be associated to the $^2\text{P}_{3/2} \rightarrow ^2\text{P}_{1/2}$ transition while the excitation spectra are formed by three UV- visible bands relative to the electronic transitions $^2\text{P}_{1/2} \rightarrow ^2\text{S}_{1/2}$, $^2\text{P}_{1/2} \rightarrow ^2\text{P}_{3/2}(1)$ and $^2\text{P}_{1/2} \rightarrow ^2\text{P}_{3/2}(2)$ of Bi^{2+} ions, whose configurational coordinate energy diagram is shown in Fig. 2.3.b).

2.1.2. Limits of the Bi application in Si-based light sources

While the Bi emission in glasses or crystalline powders is extensively studied, very few works deal with Bi in Si compatible thin films for photonic devices. The motivation is due to the fact that the reported Bi optical properties are strongly limited by the high temperatures typically used for Si-compatible materials, thus evidencing some issues, such as the out-diffusion of Bi ions and their precipitation [15], that make it difficult to control the Bi oxidation state. Indeed due to the low bismuth melting point (300 °C) [15,16] and to its high mobility in Si-based materials, the Bi precipitation is often found and unwanted because the metallic precipitates are optically inactive [16]. As examples, Fig. 2.4.a) and Fig. 2.4.b) report transmission electron microscopy (TEM) images of the precipitates formed in Bi-doped porous silica after annealing treatments at 1000 °C in hydrogen atmosphere [17] and in c-Si (100) after the Bi ion implantation [18], respectively.

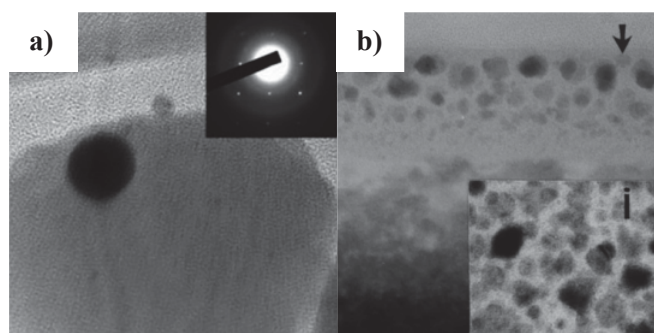
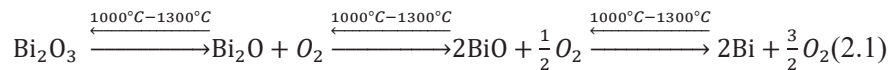


Figure 2.4. **a)** Cross sectional TEM image of a Bi crystalline precipitate in porous silica formed after 1000 °C annealing in a reducing atmosphere [17]. The full scale of the image is 153 nm. The inset reports the corresponding diffraction pattern; **b)** Cross sectional TEM image of Bi precipitates in silicon and the respective plan view as inset [18].

In the case of Bi ion implantation process in Si compatible thin films, several works report the formation of Bi metallic nanoclusters also before the annealing treatments and the co-existence of Bi⁰ and Bi³⁺ [19,20] chemical states, demonstrated by X-ray photoelectron spectroscopy (XPS). In addition, the evolution of implanted Bi ions after annealing treatments have been studied in these hosts, demonstrating that Bi³⁺ chemical state is preserved in oxidizing atmosphere, while it evolves in Bi⁰ in reducing atmosphere, at temperature above 650°C. Unfortunately, it is not easy to distinguish if the Bi contribution comes from dissolved ions or from oxidized nanoparticles, and in the last case which is their chemical composition, especially when embedded in complex silica-based materials. It was demonstrated that thermal treatments in oxygen typically can lead to the Bi precipitations in Bi oxides and silicates in place of Bi metallic nanoparticles. However, differently from Bi metallic nanoparticles, all the Bi³⁺ compounds are optically active, as demonstrated in Ref [21] for Bi oxide nanoclusters and in Ref. [22,23] for Bi silicate scintillators and nanopowders. Therefore, the control of the valence state of Bi ions and the chemical composition of the possible precipitates, if metallic or oxidized, is a fundamental aspect for their use in photonic applications.

Due to the low melting points, such as 820 °C for oxides and about 1030°C for silicates [24], these Bi compounds can be not stable under high temperature treatments, indeed they can differently evolve depending on the presence of oxidizing or reducing agents inside the same host [25], as in the following reactions [26]:



These reactions modify the chemical state of Bi ions from the 3+ to the 0 oxidation states and are reversible [27].

Therefore in order to synthesize very efficient Bi visible emitters it is necessary to control the synthesis parameters in order to permit a good dissolution of Bi ions and to avoid the formation of optically inactive precipitates that reduces the optical efficiency of the Bi-containing systems.

Another limiting factor for optical efficiency depends on concentration, as widely studied for RE-doped systems [28], the concentration quenching. It is an ion-ion interaction mechanism that consists in a resonant energy transfer (ET) between neighbour Bi ions, thus the energy continues to travel in the host until the last Bi ion de-excites by emitting a photon or by transferring it to a non-radiative decay channel, such as a defect. The probability to meet a quenching center increases by increasing the Bi content, with a consequent reduction of the emitter decay time and therefore of the emission intensity, as shown in Fig. 2.5.

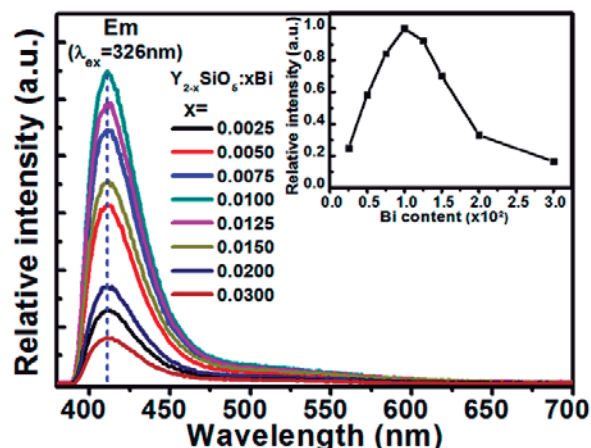


Figure 2.5. Emission spectra of $\text{Bi}_x:\text{Y}_{2-x}\text{SiO}_5$ nanopowders for different Bi contents under excitation wavelength at 326 nm. The inset shows the typical concentration quenching effect, strongly evident for x Bi content higher than 0.01 [29].

Assuming that the emitters are uniformly distributed inside the host, the quenching centers density is low enough and the energy transfer occurs through dipole-dipole interactions, the emitter lifetime, τ , can be expressed by the equation [30]

$$\frac{1}{\tau} = \frac{1}{\tau_r} + \frac{1}{\tau_i} + 8\pi C N_q N \quad (2.2)$$

where τ_r is the radiative lifetime, τ_i is the intrinsic non-radiative lifetime in absence of energy transfer, C is an interaction constant, N_q and N are respectively the defects and emitters concentration.

Thus, to make bismuth an efficient emitting center in Si compatible materials, the control of the Bi concentration and of the defect centers is a very important step in order to maximize the optical efficiency of the system, together with the preservation of a good ions dissolution in the host.

2.2. Visible emission from Bi in silicate thin films

In order to solve the limits encountered in dissolving optically active Bi in Si compatible materials we have proposed its introduction in yttrium disilicate thin films. Indeed it has been recently demonstrated that this host is one of the most suitable for Si based photonic devices. After a brief introduction on its potentiality, the structural and optical properties will be shown.

2.2.1. Yttrium silicate as a Si compatible host for emitting ions

RE silicates belong to an important class of chemically stable Si-compatible compounds formed by the mixture of silicon oxide with another

RE oxide. In this material, REs ions are not only dopants in the host but constituents, thus permitting to have silica-based materials containing high amount of REs atoms without the limit of metallic clusters formation. Recently different classes of RE silicates thin films have been studied for photonic applications [31,32], and in particular the interest is further growing towards mixtures of different RE silicates. Indeed they consist in very similar compounds, with the same crystalline structure and similar lattice parameters. In this way, also owing to the similar ionic radii between REs, it is possible to replace in a RE silicate structure another RE atom in substitutional position, by permitting to dissolve large amount of optically active REs without clusters formation. In addition, this approach has permitted to control in a continuous way the REs concentrations and, consequently, their interatomic mean distances, in order to minimize the detrimental effects of concentration quenching.

Among all the RE silicates already studied, we have chosen yttrium disilicate. Although yttrium does not belong to the lanthanides series, it chemically behaves as a RE, owing to its similar ionic radius and to its electronic configuration, $[\text{Kr}]-4d^15s^2$, that allows it to lose its three outer electrons, becoming Y^{3+} . The advantage of this structure with respect to the other REs silicates is that Y^{3+} is not optically active (having the 4f shell empty), thus giving transparency properties from the visible to the infrared range to its compounds. As a consequence, if another optically active RE is dissolved inside, the optical properties of the compound are strictly related to the additional RE.

By depending on the relative content of SiO_2 and Y_2O_3 , different stoichiometric yttrium silicates have been stabilized [33], as shown in Fig. 2.6 by the phase diagram of $(\text{SiO}_2 + \text{Y}_2\text{O}_3)$ system. Y_2SiO_5 and $\text{Y}_2\text{Si}_2\text{O}_7$ are

the most stable stoichiometric phases in thin films for application in microelectronic as dielectric gates [34,35] and in photonic devices as optically active media [36,37], thanks to the high chemical stability at the typical working conditions of Si-based devices.

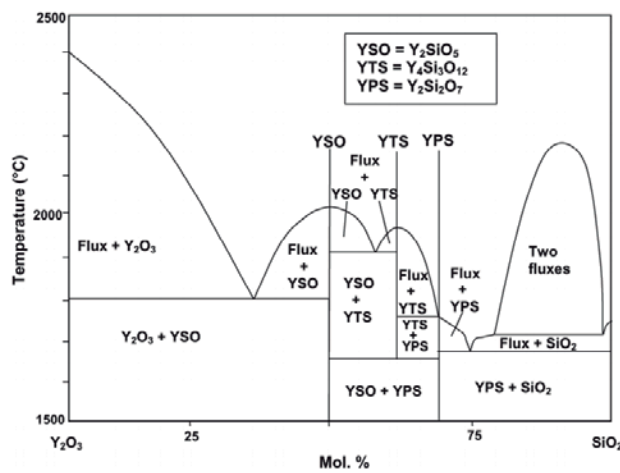
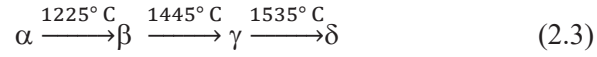


Figure 2.6. Phase diagram of $(\text{SiO}_2 + \text{Y}_2\text{O}_3)$ system [38].

The crystalline properties of Y_2SiO_5 and $\text{Y}_2\text{Si}_2\text{O}_7$ are fairly complicated because both have different crystalline phases, called polymorphisms, depending on the synthesis parameters and post annealing treatments. The control of the crystalline structure is very important because the different ligands between RE and oxygen atoms strongly affect the optical properties of REs. In particular, Fig 2.7 reports the different polymorphs found for different RE disilicates by varying the temperature of the synthesis process. Different modifications (α , β , γ and δ phase) can be stabilized and, according to *Ito* and *Johnson* [39], the transition sequence of the reconstructive transformations is the following:



Instead, the γ -phase is not shown in Fig. 2.7 because it corresponds to a “low-temperature” form, that is found also in nature in a mineral called yttrialite.

The most common phases in which thin films crystallize, after treatments at temperatures typically used for Si-based devices, are the γ and α phases, found in some cases also simultaneously. The remaining phases β , γ and δ form at higher temperature, thus are not easily stabilized. The γ -phase is monoclinic, characterized by a space group $P2_1/m$ and cell parameters $a = 7.50 \text{ \AA}$, $b = 8.06 \text{ \AA}$, $c = 5.02 \text{ \AA}$ and $\beta = 112.4^\circ$ [40]. The α -phase, found usually together with the γ -phase, has instead a triclinic structure, characterized by a space group $P-1$, with unit cell parameters: $a = 6.59 \text{ \AA}$, $b = 6.60 \text{ \AA}$, $c = 12.25 \text{ \AA}$ and $\alpha = 94.0^\circ$, $\beta = 89.2^\circ$, $\gamma = 93.1^\circ$.

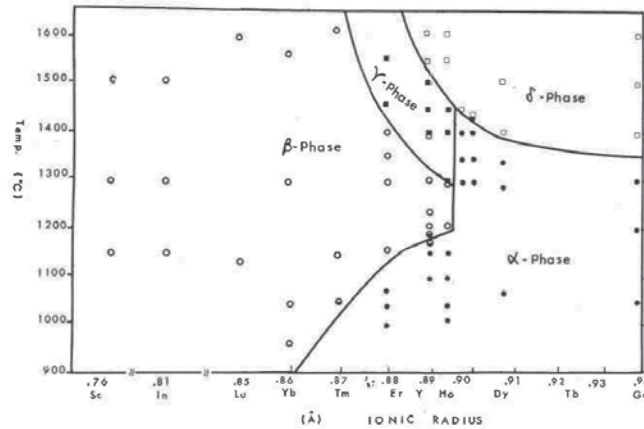


Figure 2.7. The different stable polymorphisms obtained for different $\text{RE}_2\text{Si}_2\text{O}_7$ by varying the annealing temperature [33].

Thus in general, in order to crystallize an amorphous disilicate thin film annealing temperatures above 900 °C – 1000 °C are required. An example of α -phase crystallization of $\text{Y}_2\text{Si}_2\text{O}_7$ on SiO_2 is shown in Fig 2.8. As it is possible to observe, the layer is kept amorphous although thermal treated up to 1000 °C. This thermal budget, even if not sufficient to permit the crystallization, improves the quality of the host by inducing a local ordering of the atoms as demonstrated by the optical properties of the active RE elements introduced in the host [42,43]. Temperature of 1100°C and above are indeed needed to observe crystallization.

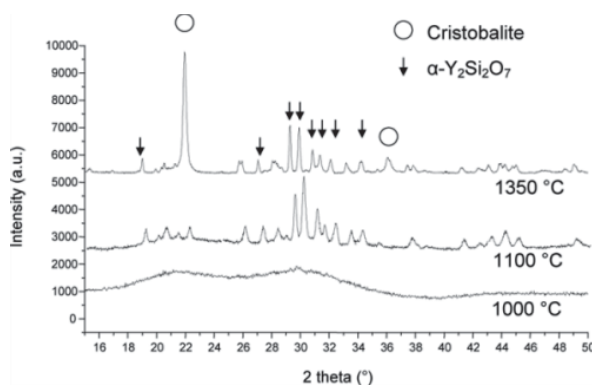


Figure 2.8. X-ray diffraction pattern of yttrium disilicate, that shows the crystallization in the α -phase of $\text{Y}_2\text{Si}_2\text{O}_7$ after 1100 °C annealing treatment [41].

The possibility to dissolve inside the Y disilicate other optically active REs has been already widely demonstrated in literature. Owing to the known similarities of Y^{3+} and RE^{3+} ionic radius and taking into account their similar crystalline structure, trivalent REs can be then well incorporated in Y substitutional position, thus tuning the concentration from the dopant to the constituent level without cluster formation, as already demonstrated for Er,

Yb for the infrared emission and for Eu, Tm, Ce [37,44] for visible emission in field emission displays (FED) applications. Also the stabilization and dissolution of divalent species, as Yb^{2+} , Eu^{2+} , Sm^{2+} , Tm^{2+} as efficient visible emitters have been demonstrated in several disilicate structures [45,47] by covering different ranges of the visible spectrum.

Since Bi ions can be stabilized in different oxidation states depending on the synthesis condition and the chemical environment and due to the peculiar properties of disilicate host to dissolve very high amount of dopants without clustering, we have proposed the introduction of Bi ions in yttrium disilicate structure. Only a few works already exist focused on Bi in yttrium monosilicate powders [29,48], interested in realizing white phosphors by the coupling with visible REs emitters such as Eu and Dy; however there are no studies on silicon-based thin films. Thus in the following the structural and optical properties will be discussed in details.

2.2.2. Controlled emission range from Bi in yttrium disilicate thin films

Yttrium disilicate thin films have been grown by ultra-high vacuum magnetron co-sputtering. The used base pressure was about 10^{-9} mbar. All the depositions were performed in Ar atmosphere (5×10^{-3} mbar) by radiofrequency co-sputtering from two high purity targets, Y_2O_3 and SiO_2 , on c-Si (100) substrate heated at 400°C during the film growth. By varying the power applied to the targets it was possible to calibrate the deposition parameters in order to obtain good quality thin films having the yttrium disilicate stoichiometry, such as $\text{Y}:\text{Si}:\text{O}=2:2:7$, as verified by Rutherford Back-scattering Spectrometry (RBS).

Bismuth was then introduced in the as deposited $\text{Y}_2\text{Si}_2\text{O}_7$ film, 130 nm thick, by a 400 kV HVEE (High Voltage Engineering Europe) ion implanter. The energy, 270 keV, has been chosen by SRIM (Stopping and Range of Ions in Matter) simulations, in order to center the Bi distribution inside the film thickness. Nominal Bi dose of $2 \times 10^{15} \text{ Bi/cm}^2$ has been used. The as-implanted samples were then annealed by a rapid thermal annealing (RTA) treatment at 1000°C for 30 seconds in an oxidizing atmosphere (O_2) and in an inert one (N_2), in order to remove eventual defects introduced by the ion implantation process and to optimize the quality of the disilicate structure.

The amorphous nature of the doped thin films after both the annealing treatments was confirmed by transmission electron microscopy (TEM). The diffraction pattern, acquired with the JEOL Jem 2010 TEM under 200 keV parallel electron beam, is shown in the inset of Fig. 2.9 for the O_2 treated sample. By bright field TEM images it was possible to observe the good quality of the annealed film also after this high temperature annealing. In the bright field TEM cross section reported in Fig. 2.9 for O_2 treated sample, the Y disilicate film appears uniform and exhibits a sharp interface with an underlying thin SiO_2 layer, about 3-4 nm thick. However it is evident also the presence of some precipitates, less than 3 nm in diameter, in the middle of the film thickness. Similar images have been obtained also for the annealing treatment in nitrogen.

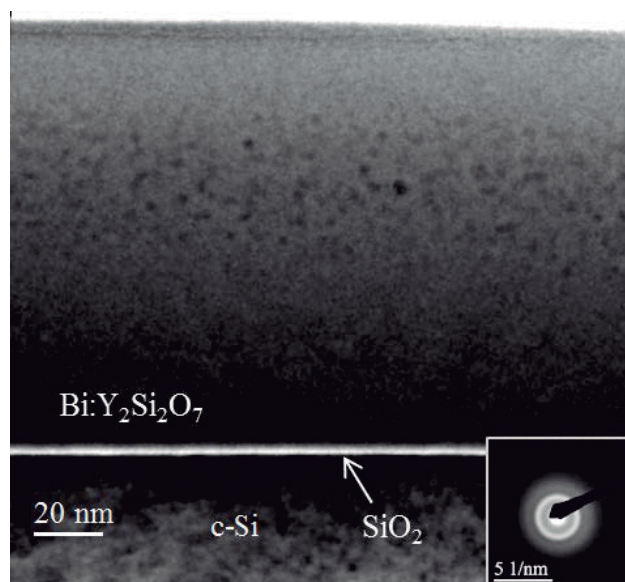


Figure 2.9. Bright field cross view TEM image of the annealed $\text{Bi:Y}_2\text{Si}_2\text{O}_7$ thin film on c-Si after O_2 treatment. In the inset the relative diffraction pattern is shown, evidencing the amorphous nature of the sample.

By an electron energy loss spectrometer coupled to the TEM apparatus, it was possible to acquire energy filtered TEM (EFTEM) images by selecting electrons that have lost the energy corresponding to the excitation of the typical shell core electrons. By making EFTEM selecting the $\text{N}_{2,3}$ -Y edge at 26 eV, the L-Si edge at 99 eV and K-O edge at 532 eV, it was possible to obtain elemental maps with the typical nanometric resolution of TEM, that demonstrated that all these elements are uniformly distributed along all the film thickness. The absence of out-diffusion of Y and O combined with the presence of a sharp interface with underlying Si are important factors for the realization of optical devices, since they demonstrate the chemical stability, especially after high temperature annealing treatments.

However it was not possible to distinguish the nature of the precipitates neither to acquire the EFTEM signal coming from electrons with energies correspondent to the O_{4,5}-Bi edge (30 eV), owing to the low Bi content and its overlapping with a broader and more intense signal related to the host plasmon, typically extended between 10 eV and 50 eV. Therefore since no precipitates are present in the un-doped Y disilicate samples we can suppose that the precipitates contain Bi, but nothing can be deduced about their composition.

Therefore a further analysis was performed by RBS measurements, in order to obtain information about the Bi distribution. In particular, Fig. 2.10 compares the Bi distribution profile of the as implanted sample with the ones after annealing treatment in N₂ and in O₂ atmospheres. RBS analysis of the as implanted sample reveals that the Bi distribution profile has a Gaussian shape, according to the ion implantation process, peaked at about 60 nm from the surface and with a FWHM of 56 nm, thus the implanted Bi dose is entirely included inside the film thickness.

Surprisingly the profiles appear different after the different treatments. In particular after the N₂ treatment the Bi distribution profile is not varied with respect to the as-implanted one, instead after the O₂ annealing it is broadened along all the film thickness and has a constant intensity equal to about 1.7×10^{20} Bi/cm³ (0.2 Bi%). Since after both treatments the total integral doses are unchanged, we can conclude that no Bi desorption occurs at this high temperature annealing. Then a redistribution of Bi ions along the film thickness is induced only in the oxidizing ambient, by an enhancement of the Bi mobility inside the Si-O structure, as already observed in silica [16].

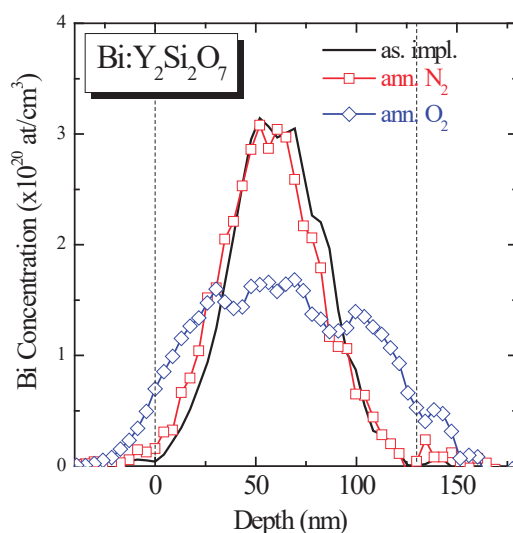


Figure 2.10. Bi distribution profile as a function of depth from the surface of the as-implanted sample and of the samples treated in nitrogen (ann.N₂) and in oxygen (ann.O₂). The profiles are obtained by RBS measurements.

Therefore, since the TEM analyses do not reveal any differences between the two treatments, we can conclude that the different atomic Bi distribution can be associated to dissolved Bi ions, not visible in TEM. Instead we suppose that the precipitates observed for both atmospheres have a metallic nature, as reported in section 2.1.2 for silica based materials [20]. Also the optical properties of the samples treated in the two annealing ambients confirm the different natures. The photoluminescence spectra (PL) of the samples treated in nitrogen and in oxygen were studied by using an He-Cd laser, with 325 nm line as excitation source, in order to involve the excitation of all the possible Bi oxidation states. The spectra have been compared in Fig. 2.11. When the samples are treated in oxygen, a blue broad band peaked at 430 nm has been observed; it is ascribed to the $^3P_1 \rightarrow ^1S_0$

transition of Bi^{3+} ions after excitation of the same Stokes shifted band. Instead for the nitrogen treated sample no blue luminescence is detectable, but only a weaker broad emission peaked at 620 nm has been observed. This orange-red signal can be associated to the Bi^{2+} oxidation state: after the $^2\text{P}_{1/2} \rightarrow ^2\text{S}_{1/2}$ excitation, Bi^{2+} ions de-excite non-radiatively to $^2\text{P}_{3/2}$, and then return to the ground state with the emission of a photon.

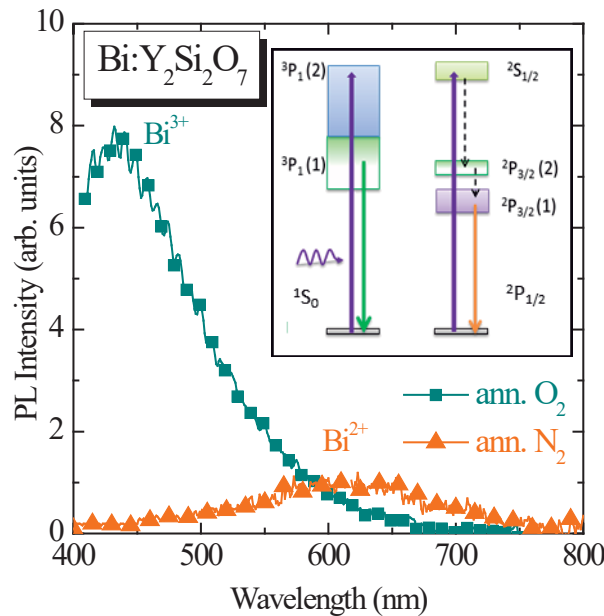


Figure 2.11. Comparison of the PL spectra from the Bi doped Y disilicate after the annealing treatment in oxygen and in nitrogen under the 325 nm excitation source [49]. In the inset, a scheme of the energy levels of both the emitting Bi oxidation states is shown, with the relative transitions involved in the excitation and emission processes.

A scheme of the energy bands of both Bi^{3+} and Bi^{2+} oxidation states is shown in the inset of Fig. 2.11. Thus after N_2 atmosphere thermal treatment the PL measurements suggest the absence of Bi^{3+} oxidation state and instead the presence of Bi^{2+} ions, probably formed by the Bi^{3+} ions reduction

induced by the high temperature annealing in N₂ atmosphere, as already demonstrated in porous silica [17]. Since the nanoparticles observed in the TEM images are present for both the annealing atmospheres, while the optical properties demonstrate a strong difference, we believe that the different optical properties can be associated to dissolved Bi ions in the host. These ions can diffuse in oxygen, as already demonstrated by RBS measurements, stabilizing themselves in Bi³⁺ oxidation state. However, though in nitrogen no Bi diffusion has been observed, optical properties demonstrate that dissolved Bi ions are present as Bi²⁺ ions.

In conclusion, although in yttrium disilicate host Bi ions are not completely dissolved into the host, the stabilization of two different oxidation states, Bi³⁺ and Bi²⁺, can be controlled by the post-annealing atmosphere and thus different emission bands, respectively in the blue and in the orange range, are obtained by making this material suitable for application in visible Si-based light emitting devices.

2.3. Beyond the Bi solid solubility limit: Bi-doped yttrium oxide thin films

In order to find a proper host to better dissolve higher optically active Bi doses in Si-compatible materials, in this section yttrium oxide thin film has been proposed. Though extensively used as phosphor, a very few reports regard its application as thin film for photonic devices. After a brief introduction on its potentiality, the structural and optical properties will be shown.

2.3.1. Yttrium oxide as a Si compatible host for REs ions

Yttrium oxide, as Y silicate, can be used as host for REs, owing to the feasibility in introducing them in Y^{3+} substitutional positions, since they have the same valence state and similar ionic radii. For example, $Eu:Y_2O_3$ powders are widely used as efficient red phosphors in combination with other green and blue emitting materials for the fabrication of “cool white” fluorescent lamps. As an example, the optical properties of (Eu+Tb) codoped nanophosphors are shown in Fig. 2.12.

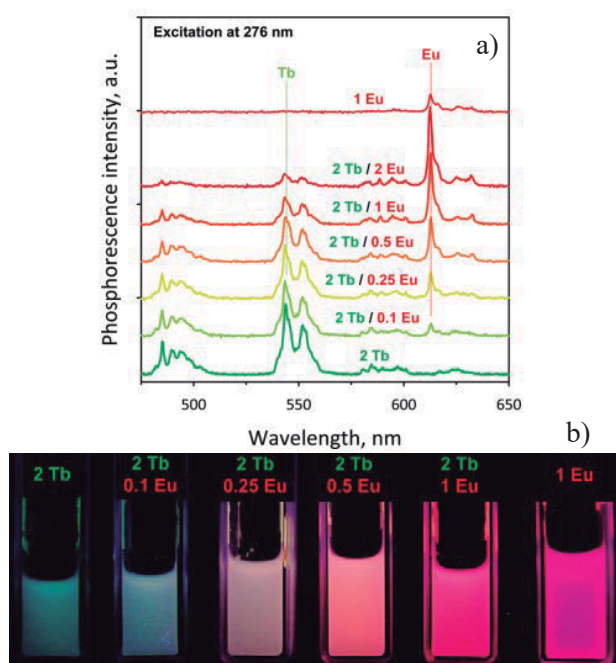


Figure 2.12. a) PL properties of Eu and Tb codoped Y_2O_3 phosphors with different Tb/Eu content ratios. b) Photos of the color-tuning of PL emission when the phosphors are dispersed in ethanol under 254 nm excitation. [51].

In particular the PL spectrum is reported in Fig. 2.12.a) where the typical green/blue emission associated to the Tb $^5D_4 \rightarrow ^7F_5$ transition is compared with the red one relative to Eu $^5D_0 \rightarrow ^7F_2$ transition. The color from the nanophosphors is fine-tuned by varying the atomic ratio of the two REs. Also photos recorded from the same nanophosphors dispersed in ethanol under UV irradiation are reported in Fig. 2.12.b) [51].

In recent years yttrium oxide (Y_2O_3) thin films grown on c-Si are receiving extensive interest in a wide range of technological applications. Indeed owing to the high dielectric constant (~ 16), the low lattice-mismatch [$a_0^{(Si)} \times 2 = 1.086$ nm; $a_0^{(Y_2O_3)} \times 2 = 1.064$ nm] and the high thermal and chemical stability with silicon at the typical Si-processing temperature, Y_2O_3 thin film has been used as a high-k dielectric for the replacement of the SiO_2 gate in complementary metal oxide semiconductor (CMOS) devices [52,53] as well as a buffer layer in memory devices [54]. Several methods have been successfully developed to synthesize good quality yttrium oxide films on silicon, such as electron beam evaporation, pulsed laser deposition (PLD), magnetron sputtering, chemical vapour deposition (CVD), molecular beam epitaxy (MBE), and atomic layer deposition (ALD).

Together to the technological developments of yttria thin film synthesis, its properties of transparency over a broad spectral range (from 0.2 μm to 2 μm), high refractive index (~ 1.9 -2.0), large band gap (~ 5.8 eV), low absorption and the well-known good quality as host for REs makes this material highly interesting also for optical and electro-optical devices, including laser mirrors, broadband interference filters, waveguides, and nano-photonic devices. In addition, since the low host phonon energies, approximately 330 cm^{-1} - 370 cm^{-1} , ensure low non-radiative losses, RE in Y_2O_3 films can reach higher quantum efficiencies. Among the REs

introduced in yttrium oxide thin films, Eu has been proposed as an efficient visible emitting center for LEDs [55]; it is also possible to find some examples of Eu [56] or Tm [57] doped Y_2O_3 thin films for visible waveguide applications. Moreover, the couple Er-Yb has been also extensively investigated for waveguides [58] or up-conversion processes in the visible for bio-applications.

2.3.2. Optimization of the yttrium oxide host for Bi dissolution

Un-doped yttrium oxide thin films were deposited on 5 inches c-Si wafers by radio-frequency magnetron co-sputtering. The power applied to the Y_2O_3 target was fixed at 500 W and the substrate was kept heated at 400°C during the deposition. Bi ions were then introduced by ion implantation at 270 keV, as already described for Bi-doped $\text{Y}_2\text{Si}_2\text{O}_7$. The Bi dose was varied between 2×10^{13} Bi/cm² and 5×10^{15} Bi/cm². The un-doped and as-implanted samples were then annealed at 800 °C for 30 min in oxygen atmosphere to remove eventual defects left over by the implantation process and to favor the stabilization of the Bi³⁺ oxidation state.

The Y_2O_3 stoichiometry has been verified by RBS both for the as deposited and Bi-doped samples. As an example the RBS spectrum is shown in Fig. 2.13.a) for the sample implanted with 5×10^{15} Bi/cm². The surface energy thresholds of the detected elements are also indicated in the same figure. The constant signals related to Y and O content along the film thickness evidence their uniform distribution, differently from the Bi related signal. The zoom of the Bi profile is reported in Fig. 2.13.b), where the x axis of the RBS spectrum has been converted from an energy scale to a

depth scale and the y axis has been converted in Bi concentration through the SIMNRA software. The Bi distribution is not uniform, as expected for an implantation profile, and shows the typical Gaussian shape related to the ion implantation processes.

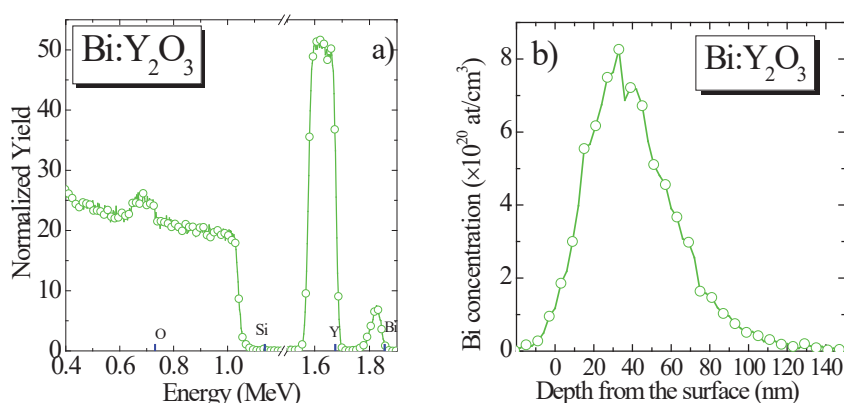


Figure 2.13. a) RBS spectrum of Y₂O₃ implanted with 5×10^{15} Bi/cm² thin film, 120 nm thick. O, Y, and Bi (in order of increasing energy) surface energy thresholds are reported as blue lines. b) Bi concentration as a function of the film thickness is reported.

The as deposited sample results to be polycrystalline, due to the thermal contribution provided by the substrate heating (400°C), that facilitates the ordered redistribution of Y and O atoms. In particular the polycrystalline body centered cubic (bcc) structure of Y₂O₃ [59] was detected by XRD analysis.

The diffraction pattern of the as-implanted samples is unchanged with respect to the as-deposited samples. Moreover after annealing treatment both the un-doped and the implanted sample keep unchanged the crystalline structure with respect to the as-deposited one. As an example Fig 2.14 shows the comparison of the XRD patterns of the annealed un-doped samples and doped with 2×10^{15} Bi/cm². Thus both the annealing treatment and the

presence of the Bi atoms do not affect the film crystalline structure. Indeed since all the diffraction peaks do not show a doublet when Bi is present, the absence of two separated phases of Y_2O_3 and Bi_2O_3 is guaranteed. They present only a slight shift towards higher angles, as shown in the insert of Fig. 2.14: it can be correlated to a slight shrinkage of the yttria lattice parameter induced by the introduction of Bi ions, having larger ionic radius, in Y sites. Thus we can suppose a good dispersion of Bi^{3+} ions in substitutional Y sites in the yttria lattice.

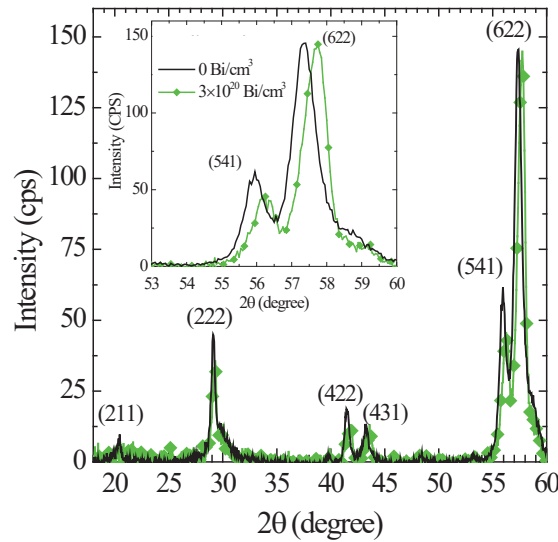


Figure 2.14. XRD spectrum of the un-doped Y_2O_3 thin film compared with the one of the as-implanted sample with $2 \times 10^{15} \text{ Bi/cm}^2$, both annealed at 800°C for 30 min in oxygen. The Muller indices of the bcc Y_2O_3 crystalline structure are reported. The slight peaks shift at higher diffraction angles in the doped sample is reported in zoom in the inset.

In order to further confirm the Bi dissolution inside the matrix and the host quality, TEM analysis has been performed. Figure 2.15 reports a TEM image in bright field of the yttrium oxide film doped with $5 \times 10^{15} \text{ Bi/cm}^2$

after the annealing treatment. The uniformity and good quality of the film is evident, in particular the good interface between film and substrate is guaranteed, thus demonstrating a good chemical stability on silicon also after high temperature annealing treatments. Large polycrystalline grains (of about 15-20 nm) are evident, and the related diffraction pattern, shown as an inset, further confirms its polycrystalline nature. The TEM images appear unchanged with respect to the ones acquired from the as-deposited and the as-implanted samples before the annealing treatment. Therefore we can assure again that implantation and annealing processes do not modify the structure of the yttrium host.

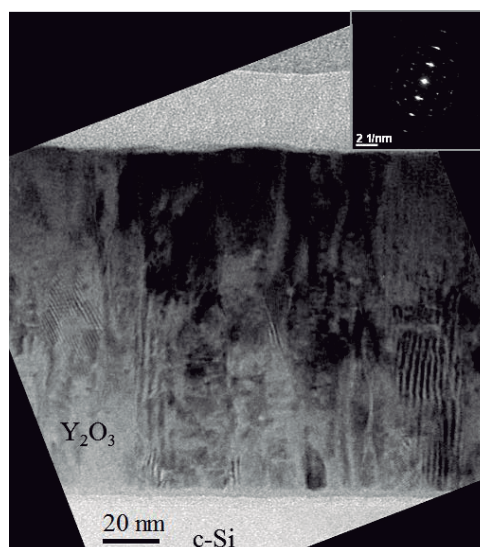


Figure 2.15. Bright-field cross-sectional TEM view of Bi:Y₂O₃ with 5×10^{15} Bi/cm² after annealing treatment. The relative diffraction pattern is shown in the inset.

Moreover no Bi precipitates are visible along the film thickness, thus demonstrating a good dissolution of Bi ions inside yttrium oxide thin film.

Therefore this host appears suitable to incorporate high Bi content without any precipitation.

2.3.3. Wavelength selective Bi³⁺ emission range

In order to study the optical properties of dissolved Bi ions in this host, the PL spectra have been recorded by using a He-Cd laser, with 325 nm excitation wavelength to involve the excitation of all the possible Bi oxidation states. Since Y is not excitable under this condition, the only observed broad band peaked at about 500 nm, shown in Fig. 2.16.a), can be associated to the Bi³⁺ ³P₁ → ¹S₀ transition. Therefore also the optical properties confirm the existence of only Bi³⁺ optically active oxidation state. Two other minor peaks at 406 nm and at 363 nm are also present.

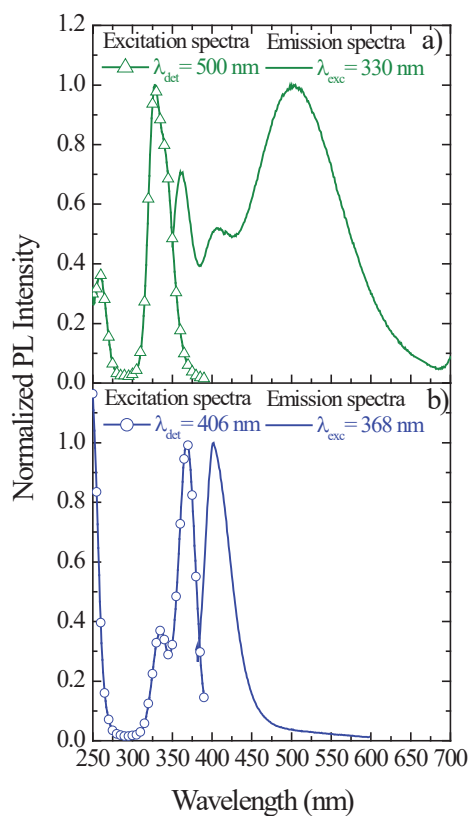


Figure 2.16. Normalized PL emission spectra from Bi:Y₂O₃ for 2×10^{15} Bi/cm². Two different emissions can be observed: **a)** related to C₂ and **b)** to S₆ symmetric sites. The excitation wavelength are reported. The excitation bands of the two sites are also shown.

In order to understand the nature of these emission peaks, PLE spectra have been recorded at 500 nm, line and open triangles in Fig. 2.16.a), and at 406 nm, line and open circles in Fig. 2.16.b). The two excitation spectra are different and can be ascribed to the same $^1S_0 \rightarrow ^3P_1$ transition but associated to two known different Y³⁺ lattice sites: S₆ sites, characterized by having two oxygen vacancies along the diagonal of the cubic cell, and C₂ sites, with

oxygen atoms missing from one of the face diagonals, as schematized in Fig. 2.17 [60]. In an yttrium oxide cubic cell the ratio between these two sites is 1:3.

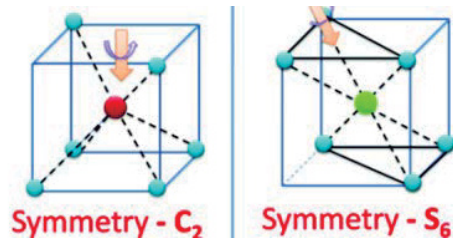


Figure 2.17. Crystalline scheme of the two symmetric sites in bcc- Y_2O_3 . Red and green dots represent the trivalent atoms while light blue dots the oxygen atoms. Two oxygen vacancies are present in both of the cells, located in a face diagonal in the C_2 site and in the cube diagonal in the S_6 site [60].

Since Bi^{3+} ions are supposed to occupy the Y^{3+} sites in substitutional position, both the two symmetric sites are possible for Bi occupancy. Due to the extensively discussed sensitivity of Bi optical properties to the environment, we expect that the emission and excitation spectra will be strongly dependent on the occupied site. The energetic schemes for a free Bi^{3+} ion and for a Bi^{3+} ion incorporated in the two symmetric Y_2O_3 sites are compared in Fig. 2.18.a), b) and c) respectively [61]. When the Bi ions are in presence of the crystalline field, the $^3\text{P}_1$ energy level splits in a doublet (in the S_6 site) or in a triplet (in the C_2 site). The correspondent levels are indicated by the Mulliken symbols [62] that take into account the symmetries with respect to the principle rotation axis. As a consequence, the radiative transitions appear strongly affected by the symmetric sites and in particular each one is peculiar of the correspondent one.

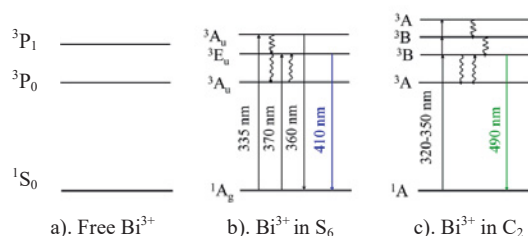


Figure 2.18. Scheme of the Bi^{3+} lower energy levels **a)** for a free ion and **b)-c)** for an ion in presence of the crystal field for the S_6 and C_2 symmetric sites respectively [61]. The most important radiative excitation and de-excitation transitions are represented by straight arrows while the non-radiative ones by wavy arrows. The reported energy level nomenclature is given by Mullikan symbols.

Thus the broad excitation band observed between 300 nm and 380 nm in Fig. 2.16.a), when the emission wavelength is fixed at 500 nm, can be ascribed to the excitation from 1S_0 to 3P_1 , that is the convolution of the triplet 3A - 3B - 3B when Bi^{3+} is in the C_2 symmetric site. The further excitation peak observed in the deep UV, at 258 nm, can be ascribed to the transition from 1S_0 to 1P_1 , permitted by the selection rules and not shown in Fig. 2.18.

Instead when the emission wavelength is fixed at 406 nm, the excitation spectrum in Fig 2.16.b) presents two main excitation peaks at 334 nm and 368 nm that can be instead associated to the $^1S_0 \rightarrow ^3P_1$ transition in the S_6 symmetric site, where the 3P_1 excited state is splitted in the doublet 3A_u and 3E_u , owing to the effects of crystalline fields and spin orbital coupling, as in Fig. 2.18.b). A further peak below 250 nm is expected; it is associated to the $^1S_0 \rightarrow ^1P_1$ transition as already identified at 258 nm for the C_2 site. Moreover the emission peak at 363 nm observed in the of Fig. 2.16.a) can be then ascribed to the $^3P_1(^3A_u) \rightarrow ^1S_0(^1A_g)$ transition of the S_6 site.

It is interesting to note from the comparison of PLE spectra in Fig. 2.16.a) and b) that it is possible to excite selectively one of the two sites by choosing the appropriate excitation range. In particular, it is possible to obtain only the green emission from C_2 site under 310 - 330 nm excitation range and only the blue emission from S_6 site for excitation wavelengths between 360 nm - 390 nm. This point is well described by the 3D emission spectra shown in Fig. 2.19 where it is evident that the green and blue emission can be alternatively switched on (and off) by properly choosing the excitation wavelength.

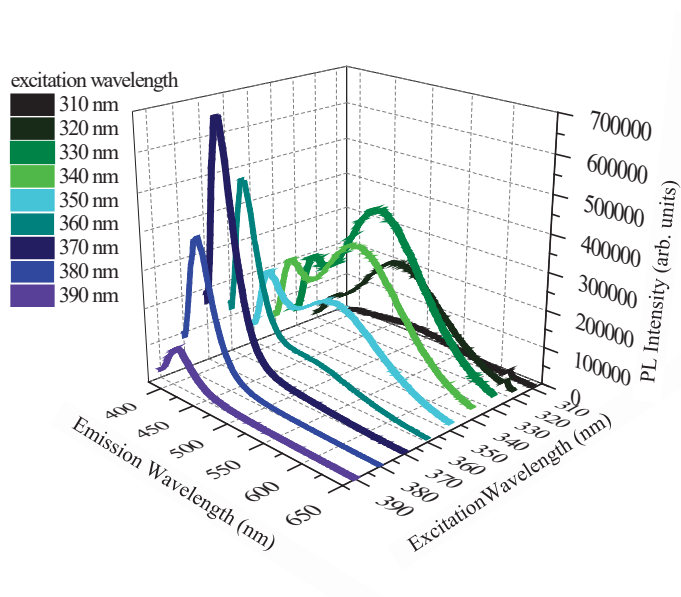


Figure 2.19. 3D PL emission spectra by varying the excitation wavelength from Bi:Y₂O₃.

Since the excitation wavelengths range between 330 and 350 nm is common to the two excitation spectra, it can excite both sites. Therefore the emission spectra in this case are given by the overlap of the two sites

emissions. In particular under 350 nm excitation, both sites have equal intensities, as it is clearly visible from the Fig. 2.19, thus obtaining a broader emission ranging from 400 nm to 600 nm.

In order to obtain the true color of the broadband emission of the sample, we have calculated the Commission International de l'Eclairage (CIE) chromaticity coordinates [63] that indicate the color of the light source independently of its luminous intensity. Indeed the chromaticity of a color can be specified by two chromaticity coordinates, x and y , that are calculated through the overlap integral of a spectral emission in all the visible range with the three functions (known as color matching functions) representing the cones spectral responses of the eyes of a standard observer. In Fig. 2.20 the CIE coordinates of the sample are represented as open dots in the CIE chromaticity diagram. In particular we report in the following the chromaticity coordinates associated to the light emitted under three peculiar excitation wavelengths, that are chosen in order to selectively isolate C_2 or S_6 Bi^{3+} emissions (320 nm and 370 nm) and to excite both of them with the same emission intensity (350 nm). Values of (0.24, 0.36) and of (0.18, 0.08) have been obtained under the 320 nm and the 370 nm excitation, respectively; the latter one in particular is very close to the CIE (1931) RGB standard blue source (0.169, 0.089). Under 350 nm excitation values of (0.23, 0.32) have been instead estimated, thus far away from the CIE (1931) RGB standard white source (0.33, 0.33) due to the lack of a red component in the emission spectrum. However, as it is possible to see by the dashed line reported in Fig. 2.20, it is possible to tune the visible emitted light in a continuous way from the violet to the green by just tuning the excitation source in the UV, from 310 nm to 390 nm, thus suggesting this material as a suitable blue/green emitter for light emitting devices.

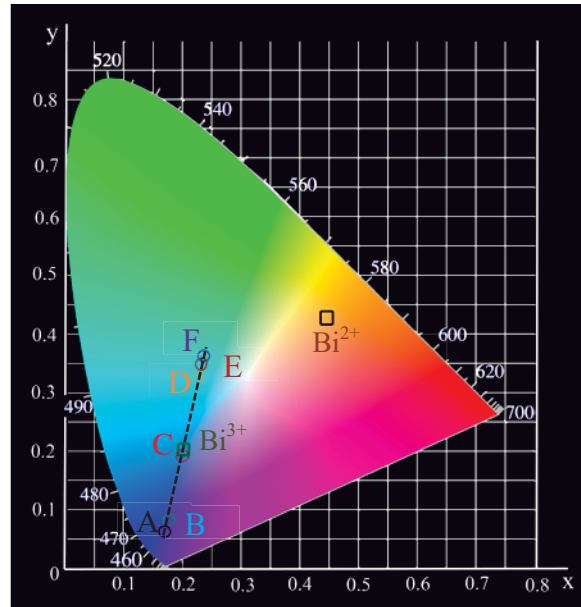


Figure 2.20. CIE chromaticity coordinates of the Bi:Y₂O₃ containing 2×10^{15} Bi/cm² after annealing treatment, under different excitation wavelengths: A under 380 nm, B under 370 nm, C under 360 nm, D under 350 nm, E under 340 nm and F under 320 nm. Chromaticity coordinates of Bi³⁺ (0.20,0.19) and Bi²⁺ (0.42,0.45) in disilicates are reported by squares as a comparison.

2.3.4. Three levels model for Bi³⁺ PL temperature dependence

In order to further understand the Bi de-excitation mechanisms in the C₂ site, which shows a high efficiency in a broader wavelengths range, temperature dependence of the optical properties has been investigated under 325 nm excitation wavelength. This analysis has permitted to study the Bi³⁺ emission properties when phonon-assisted interactions with the host are

somehow frozen by the low thermal budget and to compare them with the optical properties at room temperature (RT).

Under this excitation wavelength we have acquired both decay times and PL spectra, by varying the temperature in all the range 11 K-200 K. A He-Cd laser chopped by an acousto-optic crystal at 55 Hz has been used as excitation source. The modulated luminescence signal has been detected with a water cooled Hamamatsu photomultiplier tube coupled with a photon counting multichannel scaler with overall time resolution of 200 ns.

Figure 2.21 shows the lifetime behavior acquired at $\lambda_{\text{det}} = 500$ nm ($^3P_1 \rightarrow ^1S_0$ transition) for two different temperatures in the low temperature regime, 11 K and 30 K, for the sample containing 2×10^{15} Bi/cm². Lifetime curves appear faster at 30 K and a further reduction has been observed by increasing the temperature up to 200 K, not shown.

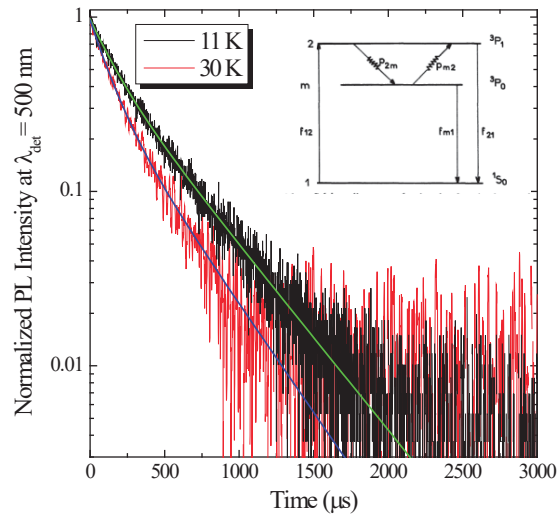


Figure 2.21. Time resolved measurements of Bi³⁺ emission band at 500 nm for 2×10^{15} Bi/cm² acquired at two different temperatures, 11 K and 30 K. Double exponential fits are also reported in the figure. In the inset, the used three energy levels scheme is illustrated.

In all the cases the curves can be fitted by a double exponential function with decay values named τ_{s1} and τ_{s2} . The already mentioned decreasing trend have been observed for both lifetimes: values ranging from 120 μs to 0.42 μs have been obtained for τ_{s1} and from 374 μs to 0.90 μs for τ_{s2} in the temperature range between 11 K and 200 K.

The $^3\text{P}_1 \rightarrow ^1\text{S}_0$ transition, related to the visible emission, is allowed by the dipole-dipole selection rules, thus radiative decay rates in the range between 10^7 - 10^9 s^{-1} are expected. However we were not able to resolve this fast component (τ_{fast}) due to the overall resolution of the used system (200 ns). Since it does not explain the longer decay times observed in Fig. 2.21 for all the investigated temperatures, a three levels model must be taken into account [64,65], whose scheme is shown in the inset of Fig. 2.21, where, the ground state ($^1\text{S}_0$) has been labeled as 1, the first permitted excited state (the multiplet $^3\text{P}_1$) as 2 and the forbidden excited state, $^3\text{P}_0$, has been labeled as “m” (metastable). We have already mentioned that the first excited level, $^3\text{P}_0$, shown in Fig. 2.18, cannot be excited directly by the absorption of a photon because the transition from the ground state is forbidden by the selection rules, but however phonon-mediated transitions between $^3\text{P}_1$ and $^3\text{P}_0$ occur. The $^3\text{P}_1$ lifetime value is of the order of 0.5 ms [65,66].

Assuming that all of these levels can be populated, being n_1 , n_m and n_2 the relative populations, the rate equation of the three energy levels can be written as [65]

$$\frac{dn_1}{dt} = n_2 f_{21} + n_m f_{m1} - n_1 f_{12} \quad (2.4)$$

$$\frac{dn_m}{dt} = n_2 p_{2m} - n_m (p_{m2} + f_{m1}) \quad (2.5)$$

$$\frac{dn_2}{dt} = n_1 f_{12} + n_m p_{m2} - n_2 (f_{21} + p_{2m}) \quad (2.6)$$

where f_{12} and f_{21} are the rate of absorption and of radiative de-excitation of the 3P_1 energy level from and to the ground state, f_{m1} is the total de-excitation rate to the ground state of the 3P_0 energy level, and p_{2m} and p_{m2} represent respectively the phonon de-excitation and phonon absorption rate from 2 to m (and vice versa). When the excitation source is switched off, a possible solution of the above equations is represented by a PL intensity function of time as a sum of two decreasing exponentials, with decay constant obtained by the solutions of the following equation:

$$\left(\frac{1}{\tau}\right)^2 - (\alpha + \beta)\frac{1}{\tau} + (\alpha\beta - p_{2m}p_{m2}) = 0 \quad (2.7)$$

with $\begin{cases} \alpha = p_{m2} + f_{m1} \\ \beta = p_{2m} + f_{21} \end{cases}$

By assuming that the radiative rate f_{21} of the permitted level is much bigger than the one of the metastable level f_{m1} and that p_{2m} is much bigger than p_{m2} in the low temperature regime, two solutions can be obtained. The first one, τ_{fast} , is associated only to the radiative emission rate f_{21} and to the 3P_1 non-radiative de-excitation up to 3P_0 by a phonon exchange with the lattice, thus being very fast,

$$\frac{1}{\tau_{fast}} = p_{2m} + f_{21}. \quad (2.8)$$

The second one is instead related to the metastable state and to the interaction between 3P_1 and 3P_0 by the absorption of a phonon; thus this lifetime value, τ_{slow} , is much longer,

$$\frac{1}{\tau_{slow}} = f_{m1} + \frac{f_{21}p_{m2}}{p_{2m} + f_{21}}. \quad (2.9)$$

This behaviour can be qualitatively explained by considering that the absorbed UV photon promotes an electron from 1S_0 to 3P_1 energy band. Then this electron can return in the ground state by causing the emission of a photon at 500 nm or it can be trapped by the energy favoured 3P_0 metastable state. Since the radiative de-excitation from this energy level is forbidden by selection rules, the electron can be reabsorbed by the 3P_1 energy level with a temporal delay related to the phonon-assisted processes. At this point it returns back in the ground state by the emission of a photon at 500 nm but, owing to the temporal delay introduced by these phonon-assisted de-excitation and reabsorption processes, the measured 3P_1 lifetime value (τ_{slow}) results longer than its direct de-excitation time (τ_{fast}).

The phonon absorption rate p_{m2} and the phonon emission rate p_{2m} are linked by the Boltzmann distribution (thermodynamic equilibrium between 3P_0 and 3P_1)

$$p_{m2} = p_{2m} e^{-\epsilon/k_B T} \quad (2.10)$$

where ϵ is the energy distance between 2 and m, T is the temperature in Kelvin and k_B is the Boltzmann constant. Thus τ_{slow} can be differently approximated in the low and in the high temperature regime by the following relationships [65]:

$$\left\{ \begin{array}{ll} \frac{1}{\tau_{\text{slow}}} = f_{m1} + \left(\frac{1}{f_{21}} + \frac{1}{p_{2m}} \right)^{-1} e^{-\epsilon/k_B T} & \text{for low temperature} \quad (2.11) \\ \tau_{\text{slow}} = \frac{1}{f_{21}} + \frac{1}{p_{2m}} & \text{for high temperature} \quad (2.12) \end{array} \right.$$

By taking into account the above described model, we can associate the observed experimental decay times in Fig. 2.21 to τ_{slow} . Since in addition the 3P_1 energy level can be splitted in a triplet, as widely discussed in section 2.3.2, the two observed components τ_{s1} and τ_{s2} can be then correlated to the interaction between the metastable state and the two 3P_1 sub-levels, named 3B .

In the low temperature regime the temperature dependence of $1/\tau_s$ can be evaluated by separately fitting $1/\tau_{s1}$ and $1/\tau_{s2}$ trends by Eq. (2.11). The $1/\tau_{s1}$ and $1/\tau_{s2}$ trends as a function of temperature and the relative fitting curves are shown in Fig. 2.22. In both cases the rates maintain almost constant up to 25 K, then they decrease rapidly.

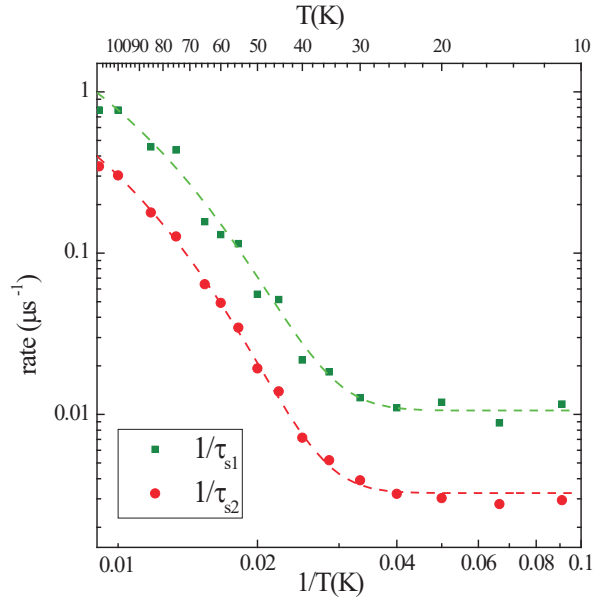


Figure 2.22. $1/\tau_{s1}$ and $1/\tau_{s2}$ decay rate versus $1/T(K)$. The continuous lines are the fitting curves, obtained by Eq. (2.11). The values ϵ_1 of 24.4 ± 0.5 meV and ϵ_2 of 21.8 ± 1 meV have been obtained by the fit.

By the reported fits, it has been possible to estimate fundamental parameters such as p_{2m} and ϵ . In particular values of $9.5 \mu\text{s}^{-1}$ and $5.1 \mu\text{s}^{-1}$ have been obtained for the phonon de-excitation rate p_{2m} , while values of $21.8 \pm 1 \text{ meV}$ for ϵ_1 and of $24.4 \pm 0.5 \text{ meV}$ for ϵ_2 have been obtained for the distances between each sub-level contained into $^3\text{P}_1$ and the metastable $^3\text{P}_0$. This suggests a distance between the sub-levels of around $2.6 \pm 1.1 \text{ meV}$. These values are compatible with the value of 30 meV already obtained for ϵ in the case of $\text{Bi:Y}_2\text{O}_3$ powders [67].

In order to verify if the same lifetime decreasing trend as a function of temperature was still valid for higher temperatures, time resolved measurement at room temperature (RT) was performed for the sample containing the same Bi dose, $2 \times 10^{15} \text{ Bi/cm}^2$, at the same $\lambda_{\text{det}} = 500 \text{ nm}$. Since the lifetime curve was not detectable by using the previous apparatus, compact spectrofluorometer equipped with a pulsed nano-LED at a nominal emission peak of 330 nm and time pulse of 1.5 ns as an excitation source has been used, suitable to detect much faster decay times but only at room temperature. The luminescence signal has been recorded with an Hamamatsu photomultiplier by using the time-correlated single photon counting (TCSPC) method. The decay curve acquired under these conditions is reported in Fig. 2.23.

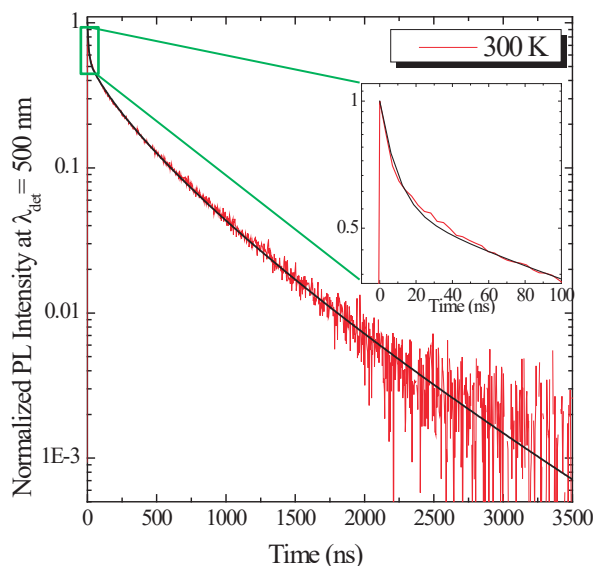


Figure 2.23. Time resolved measurement of Bi^{3+} emission band at 500 nm for $2 \times 10^{15} \text{ Bi/cm}^2$. The measurement is acquired at RT. Double exponential fit is also reported in the figure. In the inset, a zoom of the initial range 0-100ns is shown, by evidencing a further faster decay time. By a single exponential fit, reported in the same figure, lifetime value of 8 ns has been obtained.

By comparing this decay curve with the ones acquired at low T, shown in Fig. 2.21, it is immediately evident that the temporal scale differs by a factor of 1000. Despite this aspect, also at RT the lifetime curve can be fitted by a double exponential function, obtaining values of 105 ns for τ_{s1} and 497 ns for τ_{s2} which are around three orders of magnitude lower than the ones found at 11K. In addition to these slow components, the ns pulsed light source has permitted to detect much faster decay time; indeed at RT we can distinguish also the presence of a rapid component, zoomed in the inset of Fig. 2.23. This component can be fitted by a single exponential function, obtaining a value of 8 ns. Since a faster component, representing the

radiative de-excitation from the 3P_1 , is expected as a solution of Eq. (2.7), we can conclude that the observed rapid lifetime corresponds exactly with the τ_{fast} component of the three levels model.

Also the PL emission shape was detected to be strongly affected by the temperature. Fig. 2.24.a) compares the PL spectra at two different temperatures, 11 K and 275 K, for the same Bi content 2×10^{15} Bi/cm² under 325 nm excitation. Totally different spectra appear. Indeed the main broad peak observed in the green at RT decreases at lower temperatures and a further more intense peak at lower wavelengths, i.e. at 430 nm, appears, resulting in a blue light detectable also by naked eyes. We believe that this second emission cannot be ascribed to the S_6 site for two reasons: (i) the used excitation wavelength is not in resonance with the S_6 excitation band at RT so we do not expect resonance at cryogenic temperature (where the excitation and the emission bands should be indeed narrower due to the absence of lattice vibrations); (ii) the S_6 site emission at RT is typically peaked at around 406 nm.

In order to understand the nature of this blue emission, in Fig. 2.24.b) the relative integrated blue PL has been reported as a function of the temperature in comparison with the integrated green-PL and with the total integrated PL in the whole spectrum.

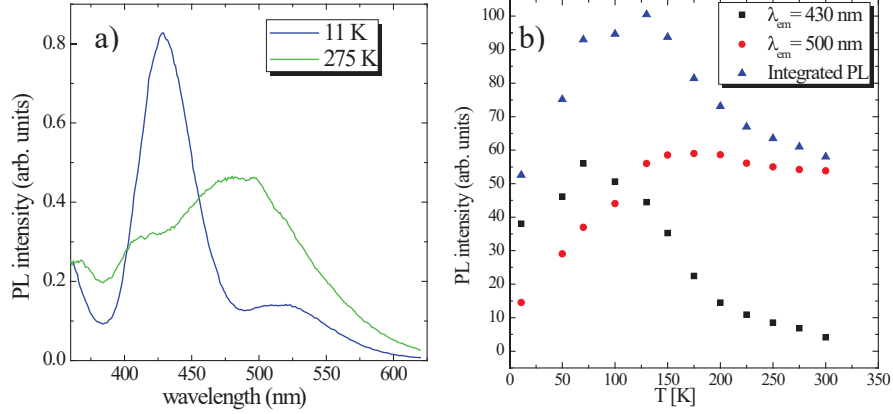


Figure 2.24. a) PL spectra for two different temperature ranges, 11 K and 275 K, under 325 nm excitation for 2×10^{15} Bi/cm². b) Green, blue and total integrated PL trend versus temperature. Integrated PL have been obtained after Gaussian deconvolution of the two peaks reported in a).

We believe that this blue-radiative emission is related to the transition from the third level of 3P_1 triplet, named 3A , to the ground state. Since the relative lifetime value is under the detection limit of 200 ns, we have concluded that this level is not involved in the interactions with the 3P_0 metastable state.

We can then explain the observed integrated PL trends of Fig. 2.24.b) in the following manner: while at low temperature the highest energy sub-level 3A , excited by the incoming photon, de-excites radiatively by emitting a photon at 430 nm faster than the non-radiative phonon-assisted de-excitation towards the two lowest 3B energy levels, when the temperature is increased this non-radiative transfer prevails. Indeed the PL intensity at 430 nm quickly decreases by increasing the temperature above 75 K because of the reduction of the number of Bi ions populating 3A , and becomes almost

zero for temperatures above 150 K, thus meaning that almost no Bi ion populates it any more. Contemporarily, the number of Bi ions in the two 3B energy sub-levels increases owing to the non-radiative de-excitation from the over-lying 3A energy sub-level by reaching a constant value at about 150 K, thus resulting in an increased PL intensity in the green, as shown in Fig. 2.24.b).

In addition, a slight decrease of PL intensities at 500 nm is visible at high temperature; this behavior is instead due to the activation of thermal quenching (non-radiative) processes related to de-excitation by phonons exchange with the vibrational levels of the host.

Therefore it is possible to conclude that while at high temperature the Bi^{3+} (C_2) lifetime is mostly related to the radiative de-excitation combined with the emission and re-absorption of phonons, at low temperature, where the phonons absorption is inhibited, the lifetime is mainly governed by the de-excitation through the metastable state 3P_0 , thus increasing the lifetime measurements and affecting also the PL behaviour versus $T(K)$. The control of the non-radiative quenching phenomena and the maximization of the number of Bi ions excited within the 3P_1 energy band, avoiding the transition in the metastable 3P_0 energy band, is indeed very important in order to obtain very efficient visible light sources. In addition by changing the temperature it is possible to move the population of the excited Bi ions from one level to another, by tuning the color of the emitted light from blue to green range.

2.3.5. Intense cathodoluminescence for FEDs applications

Among the different approaches used to produce flat panel displays, an important role is played by field emission displays (FEDs), which are emitting materials excited by electrons coming from a field emitter. Although it is true that in FED technologies many efforts are currently devoted to the development and optimization of the electron emitters, there are still very important issues related with phosphor properties, including the synthesis of thin film phosphors exhibiting a full visible luminescence spectrum. Most of the phosphors used in FEDs are RE-doped oxides or sulfides, but also the employment of Bi in powders [68] has been recently proposed. To understand the perspectives of Bi:Y₂O₃ thin films in FEDs and lighting technologies, a study of their cathodoluminescence (CL) properties has been performed and compared with the PL properties. The CL spectrum has been obtained by using a 15 keV electron beam as excitation source and mainly consists of three convolved broad bands with maxima at about 415 nm, 477 nm and 513 nm as shown in Fig. 2.25; the maxima at 415 nm and 513 nm can be related to the transition from ³P₁ → ¹S₀ in both the lattice sites C₂ and S₆. Compared with the PL emission peak reported in the same figure, the CL emission peaks are slightly red-shifted. This variation can be ascribed to the presence of charge effects related to the interaction between the electron beam with the oxide host, that can strongly influence the Bi energy bands by the variation of the electric field. Instead the peak at about 477 nm can be related to the emission from defects into the host, since present also in absence of Bi (not shown) [69].

For possible practical applications in display and lighting technologies, also in this case the chromaticity coordinates correlated with

this emission spectrum has been evaluated. Figure 2.25.b) shows the relative chromaticity diagram where the chromaticity coordinates have been reported by a circle. Color coordinates of (0.19, 0.23), corresponding to a light blue emission have been obtained, compared with the (0.23, 0.32) obtained instead under optical excitation at 350 nm, reported in the diagram as a square. These results demonstrate the possibility to excite Bi ions through high energy electrons impact and the capability of Bi doped Y_2O_3 to act as an efficient visible blue light source in field emission devices.

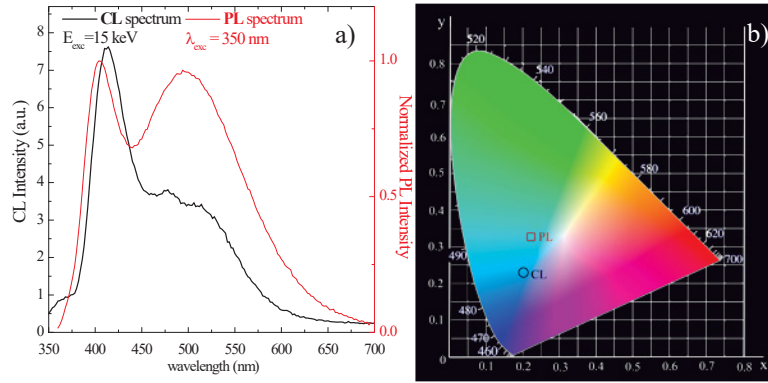


Figure 2.25. a) CL spectrum obtained for Bi:Y₂O₃ with 2×10^{15} Bi/cm² under 15 keV electron beam. The PL spectrum obtained under UV excitation at 350 nm is reported as a comparison. b) Correspondent chromaticity coordinates of the CL blue emission shown in comparison with the ones related to optical excitation.

2.3.6. Bi³⁺ concentration influence on optical efficiency

In the previous section the optical properties of Bi in terms of excitation and de-excitation mechanisms, sites influence, temperature behavior and comparison with the PL and CL properties have been discussed extensively for a fixed Bi content, 2×10^{15} Bi/cm². In this section, the

influence of Bi content on the optical properties will be treated. Figure 2.26 reports the PL trends relative to the Bi^{3+} emission at 500 nm (C_2) from $\text{Bi:Y}_2\text{O}_3$. The Bi dose values have been converted in Bi concentration by taking into account the distribution profile obtained by RBS measurements in Fig. 2.13.b) and approximating it such as uniform over a thickness 70 nm, by obtaining values ranging from $3 \times 10^{18} \text{ Bi/cm}^3$ to $7.5 \times 10^{20} \text{ Bi/cm}^3$. The Bi^{3+} PL trend is linear with the Bi concentration up to $3 \times 10^{19} \text{ Bi/cm}^3$ and then starts to deviate and saturates.

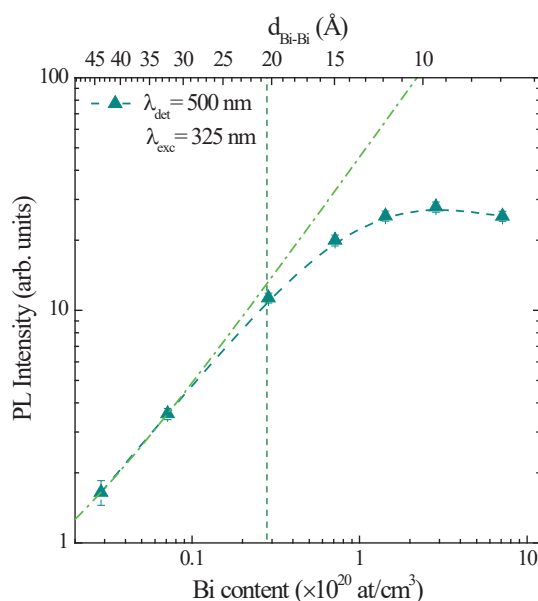


Figure 2.26. C_2 Peak PL intensity at 500 nm versus the Bi content (bottom scale) or the mean Bi-Bi distance (top scale), obtained under 325 nm excitation. Dashed line is reported in correspondence with the critical Bi concentration of $3 \times 10^{19} \text{ Bi/cm}^3$.

This behavior has been attributed to the occurrence of a concentration quenching process that originates from the interaction among Bi ions. Indeed by increasing the Bi concentration, the probability of their resonant

interaction increases leading to ET from an ion to a nearby one, until the last ion de-excites radiatively or meets a quenching center, as already observed in Ref. [70].

We can then define a critical Bi concentration, Bi_0 , above which the Bi^{3+} PL starts to deviate from the linear trend owing to the concentration quenching. Bi_0 is equal to $3 \times 10^{19} \text{ Bi/cm}^3$ in our case and, assuming a uniform Bi distribution in the film, it corresponds to a mean distance between Bi ions, d_{Bi-Bi} , of 20 \AA , defined as d_0 .

Since the PL intensity is proportional to the lifetimes, decay time measurements have been performed for all the Bi concentrations, as shown in Fig. 2.27. These measurements were performed at RT by using a nano-LED at 330 nm as excitation source, as described in 2.3.3. All the cases present the fast component related to the de-excitation of 3P_1 energy level without involving the 3P_0 metastable state that is not influenced by the Bi concentration. Instead, the long components decrease by increasing Bi content, as shown in Fig. 2.27. For all the Bi contents the PL trend versus time was fitted by the double exponential function with two different decay constants corresponding to the two sub-levels of the 3P_1 triplet. Both τ_{s1} and τ_{s2} decrease by increasing the Bi content, respectively from 150 ns to 110 ns and from 633 ns to 435 ns, due to the presence of Bi-Bi interactions and energy transfer processes that become more preponderant and faster than the direct de-excitation by photon emission. These concentration quenching phenomena, as described in 2.1.2 by Eq (2.2), influence the measured decay rate that is the combination of the intrinsic decay rate (that represents the total rate in absence of concentration quenching effects) and the non radiative decay rate due to the energy transfer between Bi ions and defect centers (grain boundaries, metastable energy levels, point defects,

vacancies). These decreases in both the lifetimes obtained by increasing the Bi content influence the PL measurements, causing the saturated behavior described in Fig. 2.26. The highest Bi contents that permit the highest emission intensity limiting the Bi-Bi interactions are found in the range $7 \times 10^{19} \text{ Bi/cm}^3$ to $3 \times 10^{20} \text{ Bi/cm}^3$.

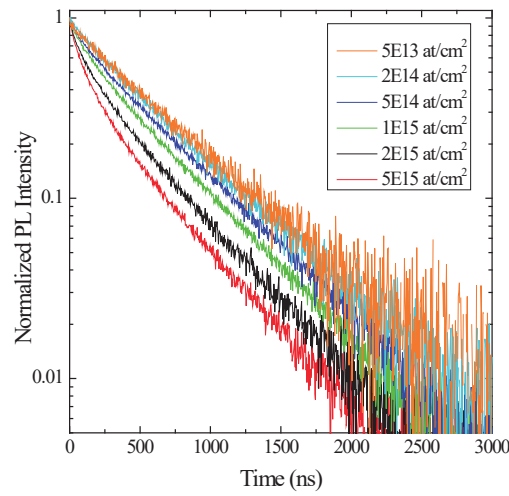


Figure 2.27. Time resolved measurement at 500 nm and RT for different Bi content under 325 nm excitation wavelength.

This result demonstrate that a good control of the Bi-Bi interaction processes or of the quality of the host are fundamental steps to further increase the optical efficiency of these systems.

2.4. Conclusions

In this chapter bismuth was proposed as a potential strong emitter for Si microphotonic applications, such as the realization of integrated light sources in a Si platform for displays and lab-on-chip devices. Indeed the synthesis of very efficient light emitting materials in the visible range

through the combination of ion implantation processes and RF magnetron co-sputtering has been demonstrated.

Two different Bi-doped hosts have been synthesized by magnetron co-sputtering of Y_2O_3 with or without SiO_2 : the yttrium disilicate and the yttrium oxide thin films. By the study of the chemical composition, the stoichiometry of these structure have been demonstrated and the Bi concentration and distribution profiles have been obtained.

Bi-doped yttrium disilicates was thermally treated at 1000°C in oxygen and nitrogen atmospheres to improve the quality of the host. In both cases the samples were found to be amorphous and in addition the presence of Bi metallic clusters has been evidenced by cross-sectional TEM analyses. Even if by a structural and morphological point of view the two atmospheres seem to influence the host in the same way, Bi distribution profiles have evolved differently in these two cases, demonstrating a strong diffusion of Bi ions along the film thickness in O_2 and no redistribution from the initial Gaussian profile in N_2 . This different behavior has been ascribed to the higher mobility of Bi-O complexes formed in O_2 environment inside the Si-O structure. Also the optical properties were completely different, demonstrating the presence of a broad blue emission in O_2 and a red one in N_2 . These emissions have been then ascribed to the formation of two different Bi oxidation state, Bi^{3+} and Bi^{2+} . Thus we have concluded that in addition to the already mentioned metallic nanoparticles there are still some Bi ions dissolved into the host that are responsible for both the distribution profile and the optical properties.

The scenario of Bi-doped yttrium oxide was demonstrated to be completely different. No diffusion of Bi ions and no evidence of Bi precipitates have been obtained after annealing treatments. In addition the

samples have the same polycrystalline bcc structure of the as-deposited Y_2O_3 without other additional phases formation, thus permitting us to deduce that all the Bi ions have replaced Y in a substitutional position, stabilizing in the Bi^{3+} oxidation state. The optical properties have been investigated under UV excitation, demonstrating that two different broad and intense Bi^{3+} emission bands in the green and the blue ranges can be observed by selectively change the excitation wavelength between 310 nm and 390 nm, ascribed to the presence of two possible Y^{3+} lattice sites (C_2 and S_6) affected by different crystalline symmetries. The only evidenced effect of the annealing treatments was then an improvement in the optical intensity of these emissions by removing the defects left over by the ion implantation process.

The Bi^{3+} de-excitation mechanisms in C_2 lattice site have been analyzed by time resolved photoluminescence measurements at different temperatures, in the range between 11K and 300K. These measurements have been explained by modelling the Bi emission and excitation bands with a three levels scheme in which the radiative Bi emitting level $^3\text{P}_1$ interacts with a metastable (but energy favored) one, $^3\text{P}_0$. This has permitted to distinguish the splitting in three sub-levels of the $^3\text{P}_1$ energy band and to evaluate their differences in terms of energy positions.

The possibility to employ $\text{Bi}:\text{Y}_2\text{O}_3$ as active material for field emitting displays technology has been investigated by the study of the optical emission under electrons excitation, known as cathodoluminescence. The obtained intense and broad emission is the superimposition of Bi^{3+} emissions in C_2 and in S_6 site, owing to transfer of the absorbed energy from the host (directly excited) to the dopant in both sites with equal probability.

Also the CIE chromaticity coordinates of these materials have been evaluated either under optical excitation or under electrons excitation, thus

demonstrating the possibility to tune the emitted color from blue to green by simply changing the host or the excitation source, which makes these Bi-doped hosts very good candidates for realizing visible integrated light sources.

References

- [1]. Thomson Reuters, Web of Science database: <http://apps.webofknowledge.com>
- [2]. G. Blasse, B.C. Grabmaier, *Luminescent materials* (Springer - Verlag, 1994).
- [3]. M. Nikl, A. Novoselov, E. Mihoková, K. Polák, M. Dusek, B. McClune, A. Yoshikawa, T. Fukuda, *J. Phys. Condens. Matter* **17**, 3367 (2005).
- [4]. W. Xu, M. Peng, Z. Ma, G. Dong, J. Qiu, *Opt. Express* **20**, 15692 (2012).
- [5]. F. Kang, M. Peng, X. Yang, G. Dong, G. Nie, W. Liang, S. Xua, J. Qiu, *J. Mater. Chem. C* **2**, 6068 (2014).
- [6]. M. Wang, X. Fan and G. Xiong, *J. Phys. Chem. Solids* **56**, 859 (1995).
- [7]. G. Boulon, B. Moine, J.-C. Bourcet, *Phys. Rev. B* **22**, 1163 (1980).
- [8]. M. Gaft, R. Reisfeld, G. Panczer, *Luminescence spectroscopy of minerals and materials* (Springer Berlin, 2005).
- [9]. M. A. Hamstra, H. F. Folkerts, G. Blasse, *J. Mater. Chem.* **4**, 1349 (1994).
- [10]. G. Blasse, A. Meijerink, M. Nomes and J. Zuidema, *J. Phys. Chem. Solids* **55**, 171 (1994).
- [11]. M. Peng and L. Wondraczek, *Opt. Lett.* **34**, 2885 (2009).
- [12]. A. M. Srivastava, *J. Lumin.* **78**, 239 (1998).
- [13]. M. Peng, L. Wondraczek, *Opt. Lett.* **35**, 2544 (2010).
- [14]. H.-T. Sun, J. Zhou, J. Qiu, *Progr. Mater. Sci.* **64**, 1 (2014).
- [15]. E. Haro-Poniatowski, M. Jiménez de Castro, J. M. Fernández Navarro, J. F. Morhange, C. Ricolleau, *Nanotechnology* **18**, 315703 (2007).
- [16]. S. Y. Park, R. A. Weeks, and R. A. Zuhr, *J. Appl. Phys.* **77**, 6100 (1995).

-
- [17]. S. Zhou, N. Jiang, B. Zhu, H. Yang, S. Ye, G. Lakshminarayana, J. Hao, J. Qiu, *Adv. Funct. Mater.* **18**, 1407 (2008).
- [18]. C. Angelov, J. Faure, M. Kalitzova, S. Simov, T. Tzvetkova and A. Djakov, *Vacuum* **51**, 285 (1998).
- [19]. S. Hishita, H. Haneda and S. Suehara, *Nucl. Instr. and Meth. in Phys. Res. B* **91**, 571 (1994).
- [20]. M. Komatsu, K. Oyoshi, S. Hishita, K. Matsuishi, S. Onari, T. Arai, *Mater. Chem. Phys.* **54**, 286 (1998).
- [21]. W. Dong, C. Zhu, *J. Phys. Chem. Solids* **64**, 265 (2003).
- [22]. W. Xiong, Y. Zhou, F. Guo, L. Chen, C. Luo, H. Yuan, *J. Cryst. Grow.* **377**, 160 (2013).
- [23]. H. Jiang, X. Wang, G. Hao, L. Wang, *J. Mater. Sci.: Mater. Electron.* **24**, 814 (2013).
- [24]. D. L. Perry, S. L. Phillips, *Handbook of Inorganic Compounds* (CRC press, 1995).
- [25]. M. Peng, C. Zollfrank and L. Wondraczek, *J. Phys: Condensed Matter* **21**, 285106 (2009).
- [26]. X. Jiang, A. Jha, *Opt. Mater.* **33**, 14 (2010).
- [27]. S. Khonthon, S. Morimoto, Y. Arai, Y. Ohishi, *Opt. Mater.* **31**, 1262 (2009).
- [28]. B. Di Bartolo, V. Goldberg, *Radiationless Processes* (Plenum Press, Springer, 1980).
- [29]. F. Kang, Y. Zhang, and M. Peng, *Inorg. Chem.* **54**, 1462 (2015).
- [30]. E. Snokes, P. G. Kik, A. Polman, *Opt. Mater.* **5**, 159 (1996).
- [31]. B. Jacquier, *Rare Earth Doped Fiber Lasers and Amplifiers* (Springer, 1997).
- [32]. A. J. Kenyon, *Progress in Quantum Electronics* **26**, 225 (2002).
- [33]. W. Y. Ching, L. Ouyang, and Y.-N. Xu, *Phys. Rev. B* **67**, 245108 (2003).
- [34]. K. Kakushima, K. Okamoto, T. Koyanagi, M. Kouda, K. Tachi, T. Kawanago, J. Song, P. Ahmet, K. Tsutsui, N. Sugii, T. Hattori, H. Iwai, *Microelectron. Engin.* **87**, 1868 (2010).

- [35]. M. Houssa, L. Pantisano, L.-A. Ragnarsson, R. Degraeve, T. Schram, G. Pourtois, S. De Gendt, G. Groeseneken, M. M. Heyns, *Mater. Science Engin. R* **51**, 37 (2006).
- [36]. J. A. Gonzalez-Ortega, N. Perea, G.A. Hirata, *Opt. Mater.* **29**, 47 (2006).
- [37]. C. Cannas, M. Mainas, A. Musinu, G. Piccaluga, A. Speghini, M. Bettinelli, *Opt. Mater.* **27**, 1221 (2005).
- [38]. K. Kobayashi and Y. Sakka, *J. Ceram. Soc. Japan* **122**, 649 (2014).
- [39]. J. Ito, H. Johnson, *Amer. Mineralog.* **53**, 1940 (1968).
- [40]. JCPDS database, powder diffraction file no. **74** (1994).
- [41]. M. Nikl, D. Nižňanský, J. Ruzicka, C. Cannas and T. Yanagida, *Silicate Glass-Based Nanocomposite Scintillators*, Advan. Nanocomp. Tech. Inch. (2011).
- [42]. H.-J. Choi, J. H. Shin, K. Suh, H.-K. Seong, H.-C. Han, and J.-C. Lee, *Nanolett.* **5**, 2432 (2005).
- [43]. R. Lo Savio, M. Miritello, F. Iacona, A. M. Piro, M. G. Grimaldi and F. Priolo, *J. Phys.: Cond. Matter* **20**, 455218 (2008).
- [44]. S. H. Shin, D. Y. Jeon and K. S. Suh, *Jpn. J. Appl. Phys.* **40**, 4715 (2001).
- [45]. G. Adchi, N. Imanaka, and Z. Kang, *Binary rare earths oxides* (Kluwer Academic Publishers, 2004).
- [46]. M. W. Shafer, *J. App. Phys.* **36**, 1145 (1965).
- [47]. E. Kaldis, P. Streit, P. Wachter, *J. Phys. Chem. Solids* **32**, 159 (1971).
- [48]. J. Lin, Q. Su, S. Wang, and H. Zhang, *J. Mater. Chem.* **6**, 265 (1996).
- [49]. A. Scarangella, M. Miritello, F. Priolo, *J. App. Phys.* **116**, 123511 (2014).
- [50]. www.eelsdb.eu
- [51]. G. A. Sotiriou, M. Schneider, S. E. Pratsinis, *J. Phys. Chem. C* **115**, 1084 (2011).
- [52]. E. K. Evangelou, C. Wiemer, M. Fanciulli, M. Sethu, W. Cranton, *J. Appl. Phys.* **94**, 318 (2003).
- [53]. M. Leskelä and M. Ritala, *J. Solid State Chem.* **171**, 170 (2003).
- [54]. C. V. Ramana, V. H. Mudavakkat, K. K. Bharathi, V. V. Atuchin, L. D. Pokrovsky and V. N. Kruchinin, *Appl. Phys. Lett.* **98**, 031905 (2011).

- [55]. V. A. G. Rivera, F. A. Ferri, J. L. Clabel H, M. A. Pereira-da-Silva, L. A. O. Nunes, M. S. Li, E. Marega Jr, *J. Lumin.* **148**, 186 (2014).
- [56]. O. Pons-Y-Moll, J. Perriere, E. Millon, R. M. Defourneau, D. Defourneau, B. Vincent, A. Essahlaoui, A. Boudrioua, W. Seiler, *J. Appl. Phys.* **92**, 4885 (2002).
- [57]. A. Huignard, A. Aron, P. Aschehoug, B. Viana, J. Thèry, A. Laurent and J. Perrière, *J. Mater. Chem.* **10**, 549 (2000).
- [58]. A. O. G. Dikovska, P. A. Atanasov, M. Jiménez de Castro, A. Perea, J. Gonzalo, C. N. Afonso and J. García López, *Thin Solid Films* **500**, 336 (2006).
- [59]. JCPDS database; power diffraction file no. 41-1105 .
- [60]. G. Blasse and B. C. Grabmaier, *Luminescent Materials* (Springer, 1994).
- [61]. G. Ju, Y. Hu, L. Chen, X. Wang, Z. Mu, H. Wu and F. Kang, *J. Electrochem. Soc.* **158**, J294 (2011).
- [62]. R. S. Mulliken, *J. Chem. Phys.* **23**, 1997 (1955).
- [63]. A. Kitai, *Luminescent materials and application* (John Wiley and Sons, Inc., 2008).
- [64]. D. L. S. Dang, R. Romestain, D. Simkin, A. Fukuda, *Phys. Rev. B* **18**, 2989 (1978).
- [65]. G. Boulon, *Le Journal de Physique* **32**, 333 (1971).
- [66]. G. Boulon, B. Moine, J. C. Bourcet, R. Reisfeld and Y. Kalisky, *J. Lumin.* **18**, 924 (1979).
- [67]. A. M. van der Craats, G. Blasse, *Chem. Phys. Lett.* **243**, 559 (1995).
- [68]. R. M. Jafer, E. Coetsee, A. Yousif, R. E. Kroon, O. M. Ntwaeaborwa, H. C. Swart, *App. Surf. Sci.* **332**, 198 (2015).
- [69]. V. V. Osipov, A. V. Rasuleva, V. I. Solomonov, *Tech. Phys.* **53**, 1525 (2008).
- [70]. X. Wu, Y. Liang, R. Chen, M. Liu and Y. Li, *J. Mater. Sci.* **46**, 5581 (2011).

“Fall in love with some activity, and do it! Nobody ever figures out what life is all about, and it doesn't matter. Explore the world. Nearly everything is really interesting if you go into it deeply enough. Work as hard and as much as you want to on the things you like to do the best. Don't think about what you want to be, but what you want to do.”

“Innamorati di un’attività e portala a compimento! Nessuno sa cosa è la vita, e non importa. Esplora il mondo. Quasi niente è veramente interessante se tu non ci vai dentro a fondo. Lavora tanto duramente quanto vuoi sulle cose sulle quali ti piace dare il meglio.”

Richard Feynman

Chapter 3: Bismuth-enhanced erbium emission for telecommunications

Since the continuous evolution of the communication technology in the last decades, the need for smaller, faster and more performing devices has brought to the integration between silicon based electronic and photonic components inside the same circuit. Nowadays the main limit is the lack of efficient planar light sources and optical amplifiers in the infrared range fully developed on silicon platform. In this scenario, erbium has been already proposed as an emitting element for long scale telecommunication systems since its emission at 1.54 μm falls in the minimum loss window of optical fibers attenuation, thus permitting to transmit the information by limiting the losses.

In order to introduce high content of Er ions in smaller dimensions, as required by Si microphotonics, the approach of mixed Er-REs compounds has been pursued in this thesis. In particular, mixed yttrium-erbium compounds synthesized by using an UHV magnetron co-sputtering system will be proposed in this chapter as possible materials for Si microphotonics amplifiers. By RF co-sputtering of Y_2O_3 and Er_2O_3 with or without SiO_2 , two different stoichiometric structures were grown, the mixed Er-Y disilicate and the mixed Er-Y oxide. In both of them bismuth has been then introduced by ion implantation.

The influence of post deposition treatments, as thermal annealing in different atmospheres, has been extensively studied, permitting us to observe by TEM characterization the presence of Bi metallic clusters in the inert (N_2) atmosphere and Bi silicate nano-agglomerates in the reactive (O_2) environment. The strong influence of these clusters on the Er optical properties was studied. In particular, it was demonstrated the presence of additional Er non-radiative decay channels in the first case and the increase of the Er optical efficiency through energy transfer mechanism from Bi^{3+} to Er^{3+} in the second case. An additional blocking action of the deleterious interaction between Er and the OH quenching centers due to the Bi silicate

nano-agglomerates was evidenced in O_2 . Hence the annealing in O_2 is highly beneficial. A different scenario is observed in REs oxides.

In fact, in the Bi-doped mixed Y-Er oxide thin films there was no evidence of Bi clusters after the annealing treatment. Instead the stabilization of Bi^{3+} valence state permits a very efficient energy transfer from Bi to Er ions, as was completely demonstrated through optical measurements. Owing to this efficient energy transfer process, a strong increase of the Er effective excitation cross section was obtained, thus allowing us to find the best Bi:Er ratio and suggesting this material as an interesting efficient thin film compound for photonic applications.

3.1. The use of bismuth as emitter for telecommunication windows

Due to the rapid development of telecommunication technology, which demands optical amplifiers with a wide and flat gain spectrum, different near infrared (NIR) emitting materials have been studied with the aim to cover the different telecommunication bands (or windows), where the data attenuation and dispersion in optical fibers are weaker, and then most favourable for data transmission. These windows have been standardized in O (original, 1260 - 1360 nm), E (extended, 1360 - 1460 nm), S (short - wavelength, 1460 – 1530 nm), C (conventional, 1530 - 1565 nm) [1], as distinguishable in Fig. 3.1 that reports the attenuation of silica fibers in the whole infrared range

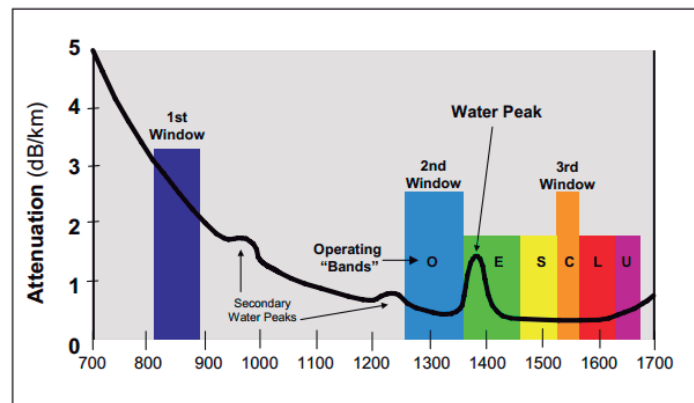


Figure 3.1. Fiber optics attenuation coefficient vs the incident radiations overlapped with the typical telecommunication windows for data transmission in silica optical. The standard one, named C (o Er) band, corresponds to the minimum of losses, is the. Water absorption peaks are also reported in the same picture [1].

The most studied materials that emit in these wavelength ranges are doped with erbium, chosen among all the NIR emitting rare earths (REs) because its main transition from $^4I_{13/2}$ to $^4I_{15/2}$ energy levels is accompanied by the emission of a photon at 1.54 micron that well matches in the C window and moreover corresponds exactly to a minimum loss of optical fibers. The use of Er implies some important limitations since the application of silicon microphotronics requires the introduction of high Er contents in silicon-based materials in order to reach highly efficient micrometric devices integrated in a Si microchip. First of all a strong limit is related to the low number of Er ions that can be introduced in Si-based materials, due to its low solubility that induces Er precipitation in clusters that are optically inactive and thus unwanted for photonic applications in micrometric devices; secondarily, the optical efficiency is limited by the occurrence of Er-Er deleterious interactions that are concentration dependent, such as concentration quenching and up-conversion. Moreover by considering also that (i) Er atomic transitions are generally forbidden by dipole selection rules and become partially permitted only in presence of a strong crystalline field and (ii) Er excitation cross sections are typically never higher than 10^{-21} cm^2 , the optical efficiency of Er based systems is strongly limited in micrometric devices [2]. For these reasons researchers are looking for new solutions to reach higher optical emission efficiency in the NIR range.

An approach is to use proper sensitizers that permit to increase the Er excitation cross section. The idea is indeed to introduce an element (the sensitizer) which can absorb light more efficiently than Er ions (the acceptor) and that can transfer this absorbed energy. Thus an energy matching between the emission band of sensitizer and the absorption band of acceptor is necessary. The most efficient sensitizers used for Er are Si

nanocrystals, as mentioned in Chapter 1, that have been successfully applied as active medium in optical amplifiers, LEDs, slot waveguides [3]. Moreover several works report on the coupling between Er ions and some other REs, with the aim to enhance Er visible or infrared emission. Among them, Tm has been proposed to increase Er visible emission by up-conversion processes, while for Er infrared emission it is well known the high efficiency of the Er-Yb coupling, where Yb permits to increase the Er excitation cross section via Yb-Er energy transfer, obtaining an enhancement by a factor of 10 [4,5]. Additionally, the Yb-Er couple has been already widely used in active media for fiber amplifiers [6] or lasers [7,8] and recently Yb-Er silicate was proposed as an active medium for electrically driven light emitting devices [9].

More recently, the use of bismuth as a sensitizer for Er in place of other RE elements has been proposed in some glasses owing to the growing interest towards its high optical efficiency. In general it was demonstrated that Bi acts as a sensitizer for Er when it presents a NIR emission. Indeed, in addition to the already discussed Bi^{3+} and Bi^{2+} oxidation states responsible of visible emission, Bi can be stabilized into several other oxidation states characterized by infrared emission bands. Since 2001, when *Fujimoto* and *Nakatsuka* first reported the existence of a NIR emission from Bi-doped silica glass [10], the researchers attention towards Bi has grown considerably, due to the enormous potentiality for optical fibres. However the nature of the Bi oxidation state responsible of this emission is still controversial. For this reason researchers often refer to it with different surnames, such as BIA or BIRAC (Bismuth Infrared Active Center). Though these emitting states have been stabilized mostly in glasses, as silicate and aluminosilicate [11], aluminophosphate [12] and germinate [13], nowadays

several works report their stabilization also in crystalline hosts [14, 15]. In all cases the Bi IR emission has always some features in common, like the absorption bands in the visible range, the broad NIR emission extended between 1100 nm and 1600 nm, and the lifetimes up to several hundreds of microseconds. As an example, Fig 3.2.a) shows the typical three NIR Bi absorption bands and their dependence on annealing temperature in Bi-doped zeolite. The absorption bands are assigned to the $^3P_0 \rightarrow ^1S_0$, $^3P_0 \rightarrow ^1D_2$ and $^3P_0 \rightarrow ^3P_2$ transitions of Bi^{3+} ions while the NIR emission can be assigned to the $^3P_1 \rightarrow ^3P_0$ transition [16]. In addition a shift and a broadening of the Bi emission peak have been reported by changing the excitation wavelength due to the different symmetries of the cation sites in which Bi can be introduced, as shown in Fig. 3.2.b).

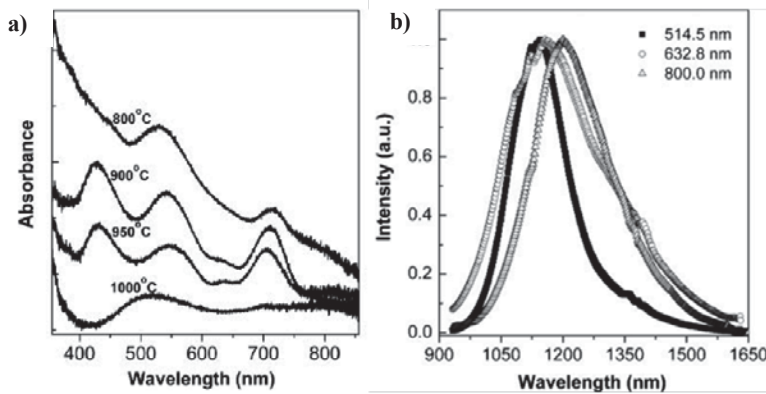


Figure 3.2. NIR Bi **a)** absorption spectra under different annealing temperatures **b)** emission spectra under different excitation wavelengths in zeolite host treated at 1000 °C [16].

In glass hosts, the energy transfer (ET) between NIR-Bi and Er ions has been already reported owing to the overlapping between the Bi 3P_1 IR band and the Er $^4I_{11/2}$ level [17, 18], but it is often accompanied by a process of back transfer (BT) from Er to Bi ions, thus limiting the Er optical efficiency

enhancement to 6-10 times. Only *Fujii et al.* [19] have succeeded in isolating the ET process from Bi ions to Er ions avoiding the BT, thanks to a peculiar host structure of zeolites. Zeolites are characterized by pores and cages, as shown in Fig 3.3.a), that permit the stabilization of BIRAC and of Er^{3+} ions contemporarily with the formation of bismuth compounds agglomerates inside the pores. While the role of the Bi compounds agglomerates has been demonstrated to isolate the optically active elements from the non-radiative decay channels (as OH quenching centers) [20, 21], the role of BIRAC is to absorb the incident light and then to de-excite radiatively by emitting photons or non-radiatively by transferring its energy to Er ions.

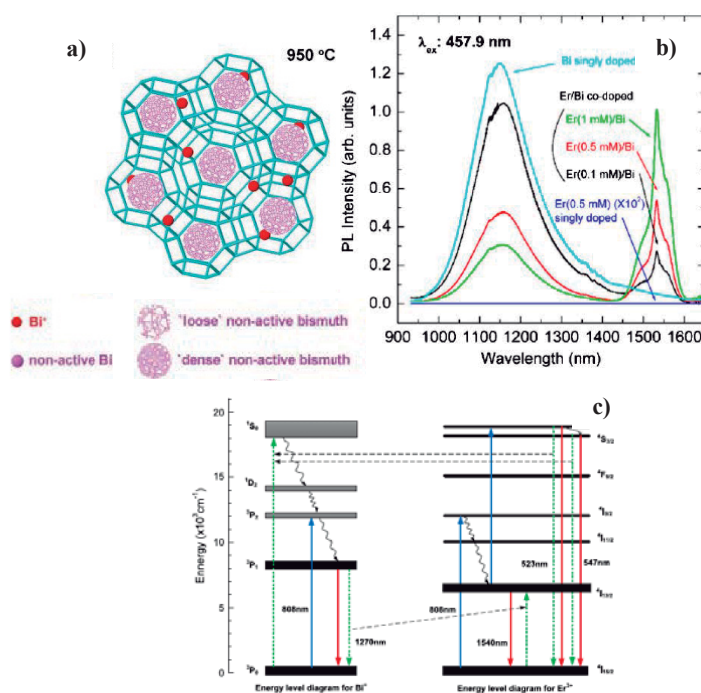


Figure 3.3. a) Scheme of zeolite structure and the relative legend [16]. b) Photoluminescence spectra from Bi-doped, Er-doped and (Er+Bi)-codoped zeolites under 457.9 nm excitation [19]. c) Er and Bi energy diagrams with some possible excitation and de-excitation processes indicated as arrows (continuous line for the radiative processes and dashed for the non-radiative ones) [18].

As an example, Fig 3.3.b) reports the photoluminescence (PL) spectra of Er-doped and (Er+Bi)-codoped zeolites obtained by fixing the excitation wavelength at 457.9 nm, that is out of resonance with any Er transitions but in resonance with $^3P_0 \rightarrow ^1S_0$ Bi transition. As it is possible to notice, in absence of Bi ions no Er emission can be observed, instead in presence of Bi ions two broad signals appear, the first one at about 1150 nm related to Bi emission and the second one at 1535 nm related to the Er transition from $^4I_{13/2}$ to $^4I_{15/2}$. In particular, by fixing the Bi concentration and by increasing the Er one, a contemporary decrease of PL intensity from Bi and increase of Er PL emission at 1540 nm are observed. This behaviour is then related to an efficient ET between Bi and Er due to the overlap between Bi energy bands with Er energy levels, as shown in in Fig. 3.3.c) [18].

In spite of the recent positive results on the NIR Bi and Er coupling, the reported hosts for the stabilization of BIRAC require synthesis techniques not compatible with the standard Si processes. Thus up to now these emitting centers are not used for applications in silicon microphotonics. Instead, some papers report the coupling between Bi^{3+} oxidation state and visible emitting REs, as Eu [22], Sm [24], Tb [23] for LEDs and for solar spectra converter [24], but very few works report these couplings in thin films for Si-based devices. Bi^{3+} ions have been demonstrated also to act as sensitizers for NIR emitting REs such as Yb [25] and Tm [26] for different applications as bio-imaging (since NIR light is silent to tissues) and c-Si solar cells. Even if there is not a direct resonance between Bi^{3+} emission bands and NIR emitting REs energy bands, since Bi^{3+} emission energy exactly corresponds to two times the excitation energy of Yb^{3+} ions, in Bi-Yb co-doped systems it has been demonstrated the efficient conversion of one UV photon into two NIR photons (quantum cutting), very

useful as up-converter material to increase the quantum efficiency of silicon solar cells. Through the optimization of their concentrations, quantum efficiency values up to 180% have been reported [27]. As examples in Fig. 3.4 Bi³⁺ PL spectra in presence and in absence of Yb³⁺ ions are shown for Bi:Y₂O₃ and (Bi+Yb):Y₂O₃. The typical Bi³⁺ luminescence band peaked at 494 nm decreases by increasing the Yb content and simultaneously the typical Yb³⁺ ²F_{5/2} → ²F_{7/2} emission appears in the NIR range [25] as shown in the inset of Fig. 3.4.

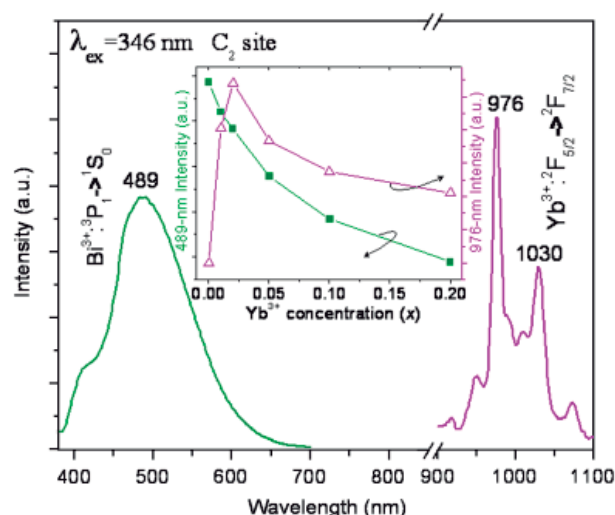


Figure 3.4. PL measurements of Bi:Y₂O₃ and (Yb+Bi):Y₂O₃ under excitation wavelength of 346 nm as evidence of quantum cutting process. In the inset, the Bi and Yb PL trends versus Yb concentration are also shown as evidence of energy transfer from Bi to Yb [25].

This recent growing interest towards Bi optical properties suggests this element as a great candidate to substitute or to be coupled with REs to obtain very efficient emitters in the visible and infrared range for Si photonic applications. However since there are no works related to its coupling with Er ions in Si-compatible hosts, we have proposed the optimization of the Bi³⁺-Er³⁺ coupling in two different original Si-compatible hosts as suitable

materials for Si-based planar optical amplifiers. The structural and optical properties related to this coupling will be illustrated in the next sections.

3.2. Bismuth in erbium - yttrium disilicate thin films

Since the Er solid solubility and its low excitation cross sections represent a very big issue for realising efficient Si-compatible planar photonics devices working in the telecommunication windows, new solutions to overcome these limits are needed. For this reason, the yttrium disilicate host will be proposed as a Si compatible host to dissolve high contents of both Er and Bi ions and their coupling will be discussed.

3.2.1. The approach of Er-based compounds to increase optical efficiency: the mixed Er-Y disilicate

The first approach suggested to overcome the Er solid solubility limit has been the use of Er compounds instead of the Er-doped hosts, among which Er silicates have been already proposed. Indeed, as discussed in Chapter 2 for Y disilicates thin films, in Er disilicates, realized by a mixture of SiO_2 with Er_2O_3 [28], it is possible to dissolve about 10^{22} optically active Er/cm^3 without clustering in a totally stable Si compatible material. Even if the main advantage is that Er is not any more a dopant element but a bulk constituent, the drawback of these compounds is the high probability of interactions between Er ions through the concentration quenching processes [29].

In order to introduce high Er contents without clustering and simultaneously to control the Er-Er interactions, new compounds have been

developed by mixing Er silicate with another RE silicate with similar structural parameters. In particular Y silicate can be chosen since both Er and Y silicates stabilize in the same crystalline phase with similar lattice parameters at about the same temperature, as shown in Fig. 2.7 of section 2.2.1. Thus it is possible to dissolve very high amount of Er^{3+} ions inside the Y silicate structure by replacing Er in Y substitutional position, as already demonstrated for Bi ions in section 2.2.2. In addition, we remind that Y disilicate satisfies several features necessary for realizing planar optical devices: (i) the synthesis procedures are compatible with the standard Si technologies; (ii) it is chemically stable by guarantying no interfacial reactions with silicon or silica substrate; (iii) the energy gap is about 4.78 eV [30] thus it is totally transparent in the visible and infrared range; (iv) it is characterized by high phonon energies (between 800 and 1200 cm^{-1}) [31], associated to the Si-O vibration. The latter aspect is very important because it influences the Er^{3+} emission spectroscopy by inducing a multi-phonons assisted de-excitation process from the upper Er excited level to the lower one, thus by favouring the radiative emission from the first excited level at 1.54 micron.

Several works report the optical properties of mixed Er-Y monosilicate [32] and disilicate [33]. Also in these Si-compatible materials the co-doping of another RE as sensitizer for Er has been already proposed in order to increase its excitation cross section. An example is the introduction of Yb^{3+} as sensitizer in mixed Er-Y silicate, since Yb has a higher excitation cross section (around 10^{-20} cm^2) with respect to Er and there is resonant matching between the Yb $^2\text{F}_{7/2} \rightarrow ^2\text{F}_{5/2}$ transition and the Er transition from the $^4\text{I}_{15/2}$ ground state to the $^4\text{I}_{11/2}$ energy level [5]. Moreover Yb has an ionic radius compatible with the Y one and its compounds present

similar structural properties, so it can be easily incorporated and well dissolved in the mixed Er-Y disilicates.

However Bi excitation cross section is known to be much higher than the ones of other REs, by reaching a value up to 10^{-17} cm^2 for Bi^{3+} in BiGeO host [34]. In addition, its excitation and emission bands are always wider than the REs ones, thanks to its particular electronic configuration, in an energy range compatible with many Er energy levels. Thus Bi can be an interesting candidate to be coupled with Er ions. Unfortunately a very few results about the ET process between Bi^{3+} and Er^{3+} ions exist in literature in Y silicate systems. For these reasons our attention will be more focused on the study of the structural and optical properties of Er and Bi co-doped yttrium disilicates in order to find the best conditions to achieve an efficient NIR emission for telecommunication.

3.2.2. Solubility of Bi ions under high temperature annealing and its influence on Bi-Er coupling

(Y-Er) disilicate thin films with different Er contents have been grown by ultra-high vacuum magnetron co-sputtering. The depositions were performed in Ar atmosphere (5×10^{-3} mbar) by radiofrequency co-sputtering from three targets (Y_2O_3 , Er_2O_3 , SiO_2) on c-Si(100) substrate heated at 400°C . By varying the power applied to the Er_2O_3 target, between 25 and 80W, and by keeping constant the ones applied to the SiO_2 and Y_2O_3 targets, respectively 300W and 200W, we have obtained $(\text{Y}_{2-x}\text{-Er}_x)\text{Si}_2\text{O}_7$ thin films, having at the same time the same disilicate stoichiometry ($\text{RE}_2\text{Si}_2\text{O}_7$) but different Er contents. The films thickness is kept constant, 130 nm, as confirmed by cross sectional scanning electron microscopy and ellipsometric

measurements. Bismuth was then introduced by ion implantation with the same parameters described for Bi in $\text{Y}_2\text{Si}_2\text{O}_7$ in chapter 2. Two different nominal Bi doses have been used, 2×10^{15} and 5×10^{15} Bi/cm².

The film chemical composition and the Er content have been evaluated in the as-deposited samples by Rutherford Backscattering spectrometry (RBS) by using a 2 MeV He^+ beam at an angle of 165° with respect to the incident beam, as in Ref [33]. As an example, in Fig. 3.5 it is shown the RBS spectrum of (Y-Er) disilicate with the lowest Er content related to the Er_2O_3 target power of 25 W. As it is possible to notice, four different signals appear: the surface energy edges of Er, Y, Si and O atoms are indicated in the figure, respectively at 1.820 MeV, 1.675 MeV, 1.138 MeV and 0.731 MeV (in order of decreasing energy).

The RBS signals are all constant, thus indicating their uniform distribution along the film thickness. We have found that the composition of the film is $(\text{Er}+\text{Y}):\text{Si}:\text{O}=2:2:7$, that corresponds to the disilicate stoichiometry. We have also estimated the Er concentration to vary between 0.3 Er% and 6.3 Er% for all the used target powers, by keeping constant the sum of Er and Y contents and therefore the film stoichiometry.

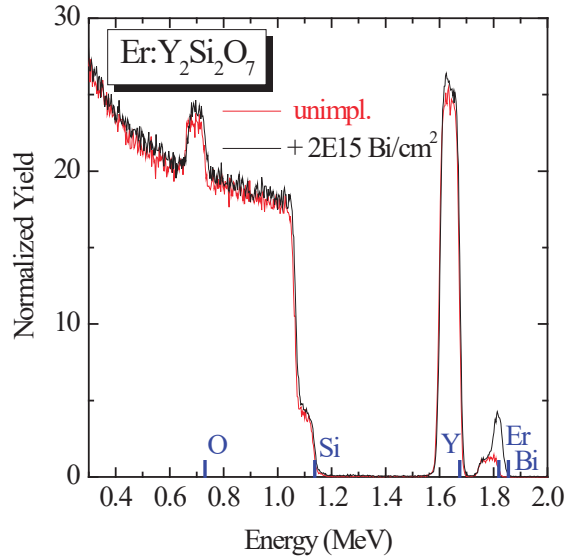


Figure 3.5. RBS spectra of Er:Y₂Si₂O₇ and (Er+Bi):Y₂Si₂O₇. The energy edges of surface of Bi, Er, Y, Si and O atoms are indicated in the figure.

Figure 3.5 shows also the RBS spectrum of the same (Y-Er) disilicate thin film after the Bi introduction. In addition to the signals already observed for the as deposited sample, a further signal related to Bi ions appears, even if partially overlapped with the Er one, since the energy thresholds are 1.855 MeV and 1.820 MeV, respectively, for Bi and Er. Even if Er is uniformly distributed into the film, it is evident that the Bi distribution has a gaussian shape, according to the ion implantation profile, with the peak position estimated to be at 60 nm from the surface and a FWHM of 56 nm, therefore entirely included inside the film thickness. Integral doses of 2.2×10^{15} Bi/cm² and 5.3×10^{15} Bi/cm² have been measured for the ion implantation, then confirming the nominal values.

The as-deposited and as-implanted samples were then subjected to a rapid thermal annealing (RTA) at 1000°C for 30 seconds in an oxidizing

atmosphere (O_2) and in an inert one (N_2), in order to remove eventual defects introduced by the ion implantation process and to guarantee a best disilicate quality. Moreover both atmospheres preserve the disilicate nature, i.e. no out-diffusion of Y, O and Er or intermixing with the silicon substrate as confirmed also by RBS measurements. This annealing temperature, as already stated in section 2.2.1 for $Y_2Si_2O_7$, is not sufficient to permit the crystallization of any polymorphs [35-37].

Instead about the Bi distribution profile the RBS measurements confirm, as already observed for $Y_2Si_2O_7$ doped with 2×10^{15} Bi/cm² in section 2.2.2, the different effects of the two annealing atmospheres: an unchanged Bi Gaussian profile for inert ambient and a Bi diffusion along all the thickness for oxidizing treatment. This behaviour was confirmed for all the Er concentrations in the mixed $(Y_{2-x}Er_x)Si_2O_7$ and for both the used Bi doses. The Bi concentration values of 0.2 Bi% and 0.5% for the lower and higher implanted doses have been estimated for oxygen treated samples, where the Bi distribution profile is uniformly spread along all the film thickness.

Since in the Bi-doped $Y_2Si_2O_7$ we have already observed a strong dependence of the optical properties on the Bi oxidation states stabilization which in turn depend on the annealing ambient, we will compare the two treatments to optimize the Bi-Er coupling and the subsequent infrared emission at 1.54 micron for photonic applications. For this reason, we have first compared the optical properties of Er:Y disilicate with and without Bi. PL measurements have been performed under two different excitation wavelengths: the 488 nm line of an Argon laser that is resonant with the $^4F_{7/2}$ level of Er^{3+} and the 325 nm line of an He-Cd laser which can involve both Bi^{3+} and Bi^{2+} oxidation states transitions, as demonstrated in chapter 2.

While under resonant excitation the typical Er emission at 1535 nm is detected for all the Er contents from mixed Er-Y disilicate [33], in absence of Bi under the UV excitation no PL emission associable to any Er energy levels has been seen. Also Y is optically inactive for both the excitation conditions.

When both Bi and Er coexist in the same host, totally different PL spectra are obtained under the same UV excitation condition for the two annealing atmospheres. In particular, for the samples treated in nitrogen, for all the Er contents, the same PL emission around 600 nm from Bi^{2+} ions is found, as shown in Fig. 3.6 for (Bi+Er):Y disilicate having 4.2 Er% and 0.2 Bi%. This PL emission is the same observed in $\text{Bi}:\text{Y}_2\text{Si}_2\text{O}_7$ having the same Bi concentration reported in section 2.2.2. No PL emission is recorded in the visible and in the infrared region associable to Er de-excitations or to Bi IR emitting centers. Therefore after annealing treatment in nitrogen the optical emission is associable only to Bi^{2+} dissolved ions and no ET mechanisms between Bi and Er are observed independently of the Er content.

After thermal annealing in O_2 we have not recorded any PL signal from Bi^{3+} ions dissolved in the host, as instead observed from Bi-doped yttrium silicate (see section 2.2.2). Instead in the visible range only a very weak emission (just a bit higher than the experimental noise) centred at 600 nm appears, as shown in Fig. 3.6. Since in the reference $\text{Bi}:\text{Y}_2\text{Si}_2\text{O}_7$ sample, not containing Er, this emission could be hidden by the very intense Bi^{3+} emission band, we cannot exclude it also in absence of Er. But together with the disappearance of Bi^{3+} luminescence in presence of Er, we observe the simultaneous appearance of a PL peak in the infrared region, as shown in Fig. 3.6. The IR peak has the typical shape associable with the Er $^4\text{I}_{13/2} \rightarrow ^4\text{I}_{15/2}$ de-excitation in disilicate [33]. Since the 325 nm excitation

wavelength is out of resonance from any Er transitions, we assure the existence of an ET mechanism from Bi^{3+} ions to Er^{3+} . We can conclude that Bi^{3+} ions de-excite non-radiatively from the $^3\text{P}_1$ to the $^1\text{S}_0$ by transferring their energy to the $^4\text{F}_{7/2}$ level of Er^{3+} , as shown in the inset of Fig. 3.6. After subsequent non-radiative transitions, due to the high phonon energy of the host (about 1100 cm^{-1} [31]), Er ions de-excite radiatively by emitting a photon at $1.54\text{ }\mu\text{m}$. This behaviour was also observed in $\text{Er}^{3+}/\text{Bi}^{3+}$ codoped SiO_2 [38].

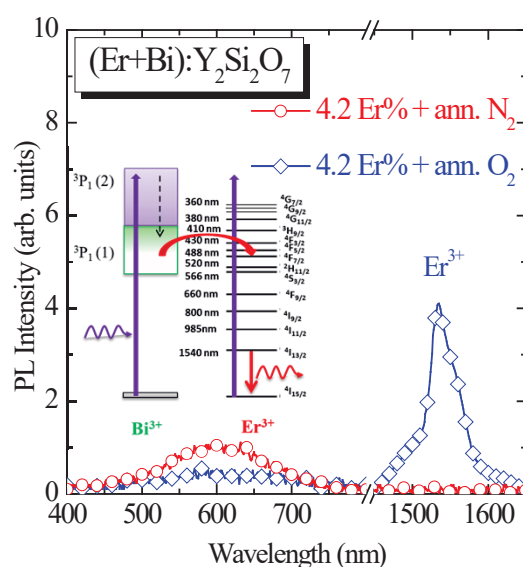


Figure 3.6. Photoluminescence spectra of (Er+Bi) co-doped yttrium disilicate after annealing treatment in nitrogen and in oxygen. Bi content is 0.2%. The measurements were acquired at RT under 325 nm excitation [40]. In the inset the energy diagram of Bi^{3+} and Er^{3+} ions and the possible excitation and de-excitation transitions are shown.

In conclusion, the PL measurements suggest the presence of ET mechanisms from Bi to Er ions only after O_2 annealing, that means only when the Bi^{3+} oxidation state can be preserved.

Moreover it was found that the PL intensities recorded at 1.54 μm under resonant excitation, PL_{Er} , from the un-implanted samples (0 Bi%) were always lower than the ones obtained from the (Bi+Er): $\text{Y}_2\text{Si}_2\text{O}_7$ samples under non-resonant excitation (325 nm), $\text{PL}_{\text{Er+Bi}}$, at the same photon flux. Therefore the mediated excitation through Bi^{3+} appears more efficient than the direct Er absorption of 488 nm photons. We have estimated for all the Er contents the enhancement factor of Er excitation efficiency, η_{Enh} , due to the mediated energy transfer through the following relation:

$$\eta_{\text{Enh}} = \frac{\text{PL}_{\text{Er+Bi}}}{\tau_{\text{Er+Bi}}} \frac{\tau_{\text{Er}}}{\text{PL}_{\text{Er}}} \quad (3.1)$$

where τ_{Er} and $\tau_{\text{Er+Bi}}$ are, respectively, the Er lifetime at 1.54 μm in absence and in presence of Bi. The τ_{Er} values in absence of Bi have been observed to decrease by increasing the Er content, varying between 4.2 ms for the lowest Er content and 1 ms for the highest one. This reduction is due to the occurrence of concentration quenching mechanisms, described in 2.1.2 [39], that affect the Er lifetime as a result of the energy migration between nearby Er ions, as already observed in mixed Er-Y silicates [32]. Instead the $\tau_{\text{Er+Bi}}$ values appear shorter than the correspondent τ_{Er} for all the Er contents. Moreover they are independent of the used excitation wavelength. This reduction has been observed also for the nitrogen annealed (Er+Bi): $\text{Y}_2\text{Si}_2\text{O}_7$ samples, where no ET has been observed since only the Bi^{2+} valence state is stabilized. Therefore this lifetime reduction in both atmospheres can be attributed to the metallic Bi nanoparticle present inside the film thickness in both the cases, as already supposed in chapter 2.

The calculated η_{Enh} values vary from 3.7 for the samples with lower Er contents (0.3 Er% and 1.8 Er%) to 5 for the highest Er contents (4.2 Er% and 6.3 Er%). We can suppose that this small increase can be correlated to the decrease of the mean distance between the Bi^{3+} and Er^{3+} ions in the host, thus increasing their coupling. By taking into account that the calculated η_{Enh} value is proportional to the ratio of the Er effective excitation cross section (mediated by Bi) and the Er direct one (due to absorption at 488 nm), it was found that the mediated excitation cross section is increased up to 5 times with respect to the direct one despite the unwanted metallic Bi clustering formation.

3.2.3. Chemical evolution of Bi precipitates under oxidizing or inert thermal treatments

In order to further optimize the ET process, we have increased the Bi doses introduced in the $(\text{Y}_{2-x}\text{Er}_x)\text{Si}_2\text{O}_7$ samples. We have observed no differences in the optical properties of the samples treated in nitrogen with respect the lower Bi dose, i.e. no ET processes is present and Er decay time reduction is evident. However for the highest Bi dose used after an annealing treatment in O_2 atmosphere a very different scenario is observed: under out of resonance excitation at 325 nm, no PL signal from Er ions at 1.54 μm has been recorded, suggesting the absence of ET mechanisms under this excitation wavelength, neither emission from any Bi oxidation states in the visible range is detected. Thus we have acquired photoluminescence excitation (PLE) measurements by fixing this detection wavelength. The PLE spectrum is shown in Fig. 3.7 with the relative figure of merit in false colors as inset.

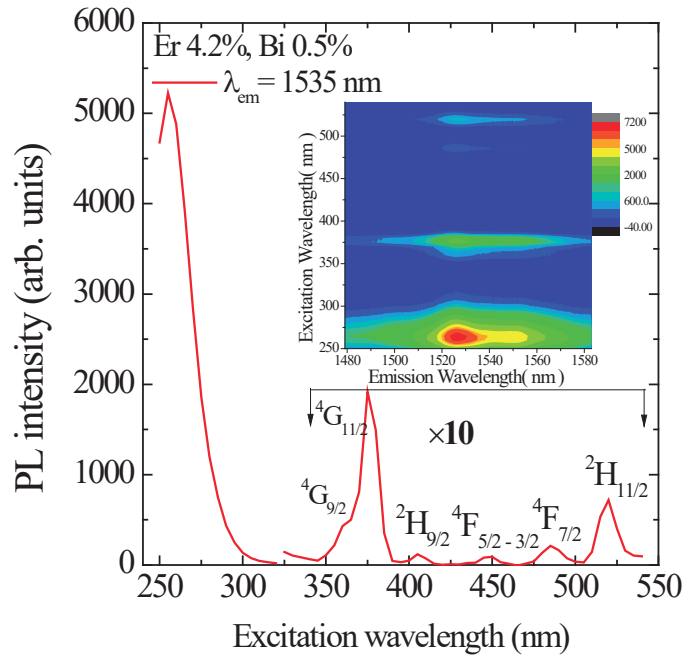


Figure 3.7. PLE of Er emission at 1535 nm in the (Er+Bi):Y₂Si₂O₇ having 4.2 Er% and 0.5 Bi%. The Er resonant excitations are peaked at 370 nm, 410 nm, 445 nm, 488 nm and 520 nm while the mediated contribute from Bi³⁺ is peaked at 255 nm. In the inset, a false colour figure of Er luminescence vs excitation wavelength is shown. Mediated excitation is 250 times higher with respect to the direct one at 488 nm.

It is evident that besides the different peaks relative to direct Er excitation, correspondent to the transitions between the ground state and the excited $^2H_{11/2}$, $^4F_{7/2}$, $^4F_{5/2-3/2}$, $^2H_{9/2}$ and $^4G_{11/2}-^4G_{9/2}$ levels (in order of increasing energies), a further peak at 255 nm is present. It is worthy to notice that the intensity of this contribute is 25 times and 250 times higher than the Er direct one respectively under 380 nm and 488 nm. Since it is well known that Bi³⁺ excitation and emission band can shift by depending on the

chemical environment, and that in Bi silicate compounds [41,42] the $^1S_0 \rightarrow ^3P_1$ excitation transition is expected to be shifted at about 250 - 280 nm, we can suppose that the observed excitation band is ascribed to the $^1S_0 \rightarrow ^3P_1$ excitation of Bi^{3+} in Bi silicate compounds stabilized inside the Y disilicate and the successive energy transfer to Er ions, probably through the match between the Bi excitation band and the Er $^2P_{3/2}$ level or through Bi emission band, spread between 400 nm and 500 nm [42], and the relative Er $^4G_{11/2}$ - $^4G_{9/2}$, $^2H_{9/2}$, $^4F_{5/2}$ - $^4F_{3/2}$, $^4F_{7/2}$ energy levels.

In order to verify the eventual presence of these aggregates in the O_2 treated sample containing 0.5 Bi%, a more detailed structural characterization has been performed. Cross sectional transmission electron microscopy analysis (TEM) with a JEOL Jem 2010 and 2010 F under 200 keV parallel electron beam have been done. In particular, Fig. 3.8.a) and Fig. 3.8.b) report the cross sectional TEM images in bright field of, respectively, the O_2 and N_2 treated sample, containing 4.2 Er% and the highest Bi dose, 5.3×10^{15} Bi/cm². It was possible to observe the good quality of the annealed films also after this high temperature annealing. Also in mixed (Y-Er) disilicate, the O_2 treated sample has an underlying thin SiO_2 layer, about 3-4 nm thick, as observed for Y disilicate in the section 2.2.2.

However also for this Bi content in both the two cross-section views, in the middle of the film thickness it was possible to observe the presence of precipitates, about 6 nm in diameter. These nanoparticles are almost two times bigger than the ones observed for the lowest Bi dose in section 2.2.2, but their distribution appears different in the two ambients. After the annealing treatment in O_2 the particles distribution appears less dense than the one obtained for annealing treatment in N_2 , as it can be seen from the comparison of the two images in Fig. 3.8. In addition, after annealing

treatment in O₂ the nanoparticles distribution is not uniform in all the sample regions analysed, where regions without nanoparticles have been found.

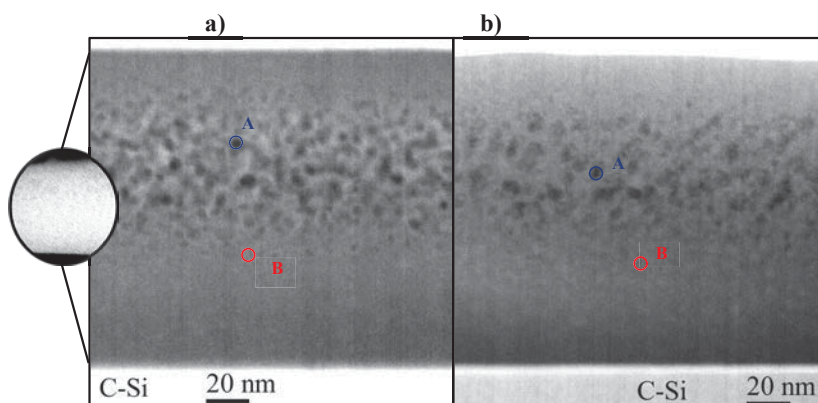


Figure 3.8. a) Cross view TEM images in bright field of (Bi+Er):Y₂Si₂O₇ thin film on c-Si, having 4.2 Er% and 0.5 Bi%, after annealing treatment **a)** in N₂ and **b)** in O₂ ambient. EFTEM image of the nitrogen annealed sample, obtained by selecting the Er N shell (168 eV), is shown in the inset of Fig.3.5.a).

An eventual Er precipitation can be excluded by energy filtered TEM (EFTEM) image recorded by selecting the electrons that have lost energy corresponding to the Er-N shell (168 eV), that shows a uniform Er distribution along all the thickness of the mixed (Y-Er) disilicate host after both treatments. The EFTEM image taken after nitrogen annealing is shown in the inset of Fig 3.8.a). Instead, also for this higher Bi dose it was not possible to acquire the EFTEM signal coming from electrons with energies correspondent to the O_{4,5}-Bi edge (30 eV), owing to the low Bi content, as in section 2.2.2.

In order to further understand the nature of the observed precipitates, energy dispersive X-ray analysis (EDX) was performed with a JEOL ARM

sub-Angstrom microscope, equipped with a sub-nanometric electron probe in scanning TEM (STEM) mode for both the treatments. We have observed different signals from matrix and from nanoparticles for both the ambients. As example in Fig. 3.9 we compare the spectra obtained by focusing the sub-nanometric probe exactly on a nanoparticle, point A in Fig. 3.8.a) and on a point of the matrix far away from the region containing the nanoparticles, point B in Fig. 3.8.a), in the nitrogen treated sample. An identical situation has been recorded for the oxidizing atmosphere.

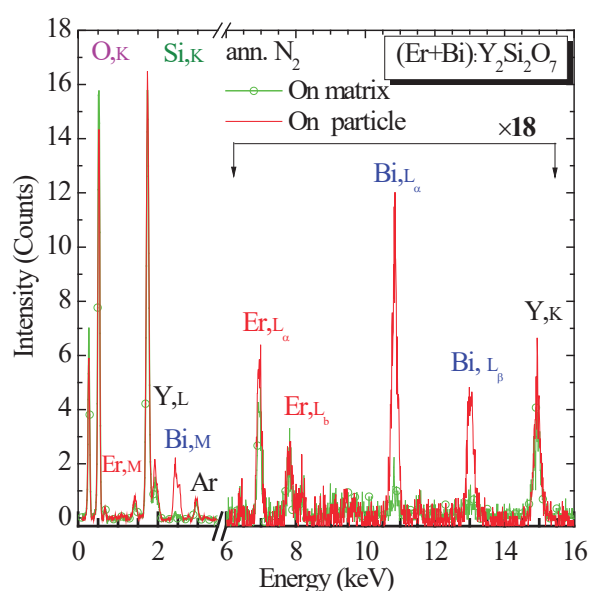


Figure 3.9. EDX spectra acquired for the N_2 treated $(Bi+Er):Y_2Si_2O_7$ samples, having 4.2 Er% and 0.5 Bi%, with a sub-nanometric electron probe on the matrix and on a particle embedded in the matrix. The elements shells correspondent to the observed peaks are listed in the picture.

While on the matrix all the signals relative to the elements contained in the host (O, Si, Y and Er) are present, when the probe is focalized on a precipitate all the peaks relative to the shells of Bi ions are detectable and

appear overlapped to the EDX spectrum of the host, whose contribute cannot be excluded since it shields the nanoparticle.

Therefore it is possible to conclude that for both the annealing treatments the precipitates are mainly composed by Bi. However, since it is impossible to separate the contribution of the embedding host, the EDX spectra from the precipitates cannot give the exact chemical composition of nanoparticles, such as for example Bi metallic, oxidized or silicates. For this reason, electron energy loss spectroscopy (EELS) spectra have been acquired in STEM mode with a 60 keV sub-nanometric electron beam in the same two points of the EDX analysis and for both the annealing treatments. The low loss region from 0 to 70 eV is characterized by the energy losses after excitation of a collective oscillation of conduction electrons, called plasmon resonances. The plasmon energy and peak shape are not simply characteristic of a specific element but also sensitive of its chemical bonding. Figure 3.10 compares the spectra obtained on the nanoparticles (point A) and on the matrix (point B) in N₂ annealed samples.

The complex spectrum acquired on the disilicate matrix can be explained as the overlap of the experimental EELS spectra of its two constituent oxides, SiO₂ and Y₂O₃, as shown in the same figure. More in details, the peaks at 15 eV and 30 eV correspond to the single and double plasmons of Y [43] and the one at 36.4 eV to the Y intra-atomic transition involving the N_{2,3} shell [43], instead, the broad peak at 22.5 eV corresponds to the SiO₂ plasmon loss [44]. Vertical dashed lines are also reported in Fig. 3.10 in correspondence of the Y-N_{2,3} shell and SiO₂ plasmon loss peaks. Since the electronic structure of a silicate can be reproduced by the superposition of the electronic structures of its constituting oxides, as demonstrated for transition metal and RE silicates [44-46], we can conclude

that the observed spectrum corresponds exactly to the one of an yttrium silicate compound. In addition, any contribution from Er_2O_3 is not visible, most probably due to the low Er content inside the host (4.2%) with respect to Y (14%), Si (18.2%) and O (63.6%).

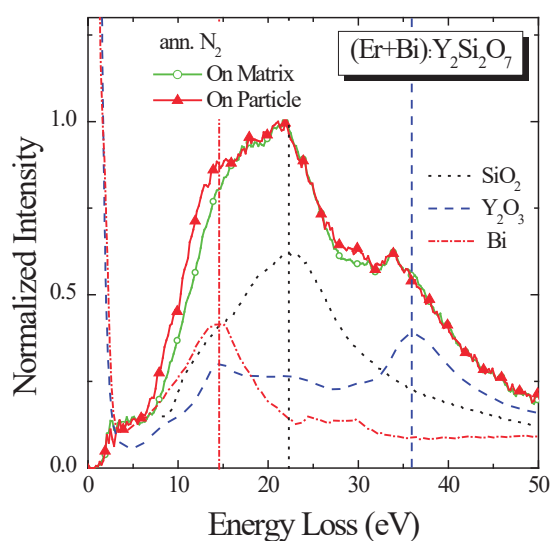


Figure 3.10. Low loss EELS spectra acquired from N_2 treated $(\text{Bi}+\text{Er})\text{:Y}_2\text{Si}_2\text{O}_7$ samples, having 4.2 Er% and 0.5 Bi%, acquired with a sub-nanometric electron probe on the matrix and on a nanoparticle embedded in the same host. The experimental EELS from Bi, SiO_2 and Y_2O_3 are also shown. The zero loss signals have been aligned and multiple scattering background signals have been subtracted by using the Fourier-Log method [47].

When the sub-nanometric probe is instead focused on a particle, the EELS spectrum, shown in the same Fig. 3.10, is quite similar to that one from the matrix. Since the particle is embedded in the yttrium silicate host, the most predominant EELS signal remains still the yttrium silicate one, but in addition a shoulder at lower energy, about at 14.4 eV, is clearly evident. The nature of this shoulder can be associated to the Bi plasmon peak [48], as

verified by acquiring the experimental EELS spectrum from a metallic Bi lamella, also plotted in Fig. 3.10. The relative peak has been marked in Fig. 3.10 by a vertical dashed line. Since by the EELS spectrum the contribution from the particle is distinguishable from the host, we can conclude that the particles are composed by metallic Bi in the sample annealed in N₂ ambient.

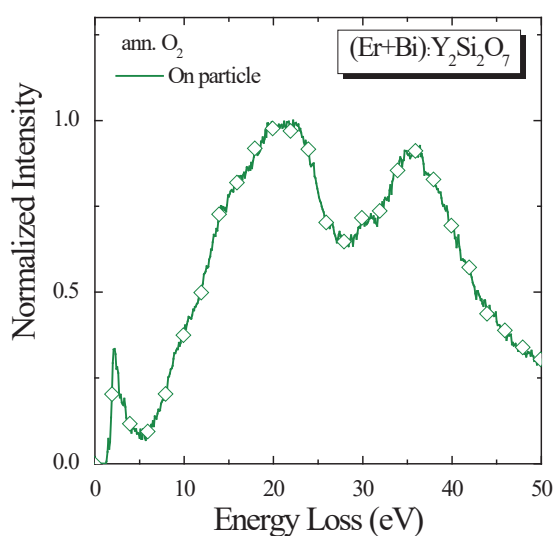


Figure 3.11. Low loss EELS spectrum acquired from O₂ treated (Bi+Er):Y₂Si₂O₇ samples, having 4.2 Er% and 0.5 Bi%, with a sub-nanometric electron probe on a nanoparticle embedded in the same host. The low loss spectrum acquired on the matrix has been found to be identical.

A totally different behaviour has been observed for the sample treated in oxygen atmosphere, shown in Fig. 3.11. In this case the EELS spectrum recorded on the particle is always identical to the one recorded on the matrix.

Thus we can deduce that no Bi metallic nanoparticles are formed after oxidizing annealing treatments, differently from the N₂ case. But since these nanoparticles contain Bi ions, as evidenced by EDX measurements, we can

conclude that they are composed by other Bi compounds, such as bismuth oxide or bismuth silicate, both stable under this temperature annealing. However the direct evidence of these chemical compositions was not possible since by EELS the relative signals cannot be distinguishable because they fall in the same energy range, from 15 eV to 40 eV, where the intense signals from the host are predominant. The good agreement between the observed absorption data with the absorption peak of Bi^{3+} in Bi silicate compounds (see Fig. 3.7) allows us to assert that these agglomerates are formed by Bi silicate compounds. These results are well supported by the Bi_2O_3 - SiO_2 phase diagram [49] that shows the formation of a Bi-Si-O stable phase for $\text{Bi}_2\text{O}_3/\text{SiO}_2$ ratio higher than 2:3, thus confirming the reason why these agglomerates are formed only for higher Bi dose and in an oxidizing atmosphere.

Even if the formation of Bi metallic nanoparticles after annealing in a reducing atmosphere has been already discussed in literature [50], the chemical nature of the Bi precipitates in air or in oxidizing atmospheres has never been discerned, since the enormous difficulty to experimentally distinguish the precipitates contribution from the silica-based host. By the correlation of PLE measurements and sub-nanometric STEM-EDX and STEM-EELS analyses we have instead succeeded to distinguish between the formation of metallic nanoparticles and Bi silicate agglomerates for higher Bi concentration after the two annealing ambients.

In conclusion, we have demonstrated that even if Er ions introduced in yttrium disilicate host by magnetron co-sputtering are well dissolved inside the host, Bi ions do not exploit the same solubility, with the clustering of metallic or silicate Bi precipitates, respectively, after N_2 and or O_2 treatments.

3.2.4. Blockage action of Bi agglomerates in O₂ atmosphere

In addition to the highly efficient mediated excitation through Bi ions from the Bi silicate agglomerates, Fuji et al. attributed a peculiar blockage [16,21] behaviour to similar precipitates, i.e. the increase of Er optical efficiency through the good isolation of Er ions from non-radiative decay channels, due in particular to OH centers. In order to verify if our Bi silicate precipitates have the same behavior in the (Er+Bi):Y₂Si₂O₇ host, we have studied PL properties under Er resonant excitation. What is surprising is that even when the (Bi+Er): disilicate samples having 0.5 Bi% and treated in O₂ are excited under the Er resonant wavelength of 488 nm, the Er PL intensity at 1.54 μm, PL_{Er+Bi}, is increased for all the Er contents by a factor of 1.3 with respect to the one observed in the un-implanted samples, PL_{Er}. In order to better understand this peculiar behaviour, we have measured the Er decay times at 1.54 μm in presence of Bi, τ_{Er+Bi} , and compared them with the values, τ_{Er} , obtained in absence of Bi, as reported for two Er contents in Fig. 3.12 as examples.

It is evident that, for all the Er contents, the PL decay curves are strongly influenced by the presence of Bi. In particular for Bi doped samples the curves appear composed by two contributions: the first one coincident to the un-implanted case, τ_{Er} , and the second one slower. They can be then fitted with a double exponential function

$$I_{PL}(t) = (1 - A) e^{-\frac{t}{\tau_1}} + A e^{-\frac{t}{\tau_2}} \quad (3.2)$$

where (1-A) and A represent, respectively, the fraction of Er ions that de-excite with the shortest lifetime τ_1 and the longest lifetime τ_2 .

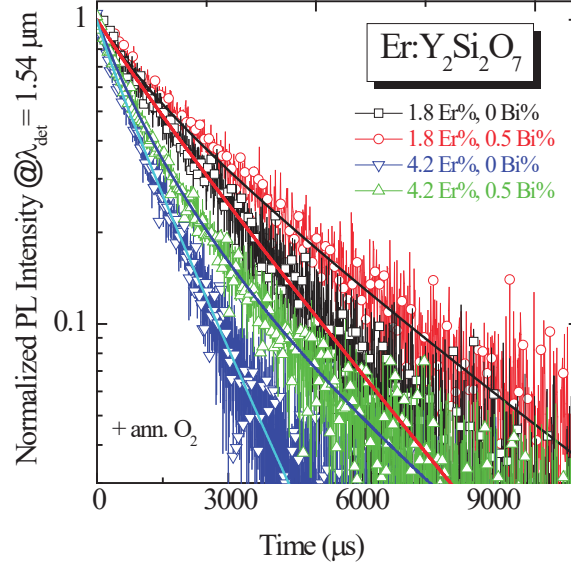


Figure 3.12. Time resolved measurements of Er at $\lambda_{\text{det}} = 1535$ nm from (Er+Bi):Y₂Si₂O₇ samples for two different Er contents, 1.8 Er% and 4.2 Er% in presence and in absence of Bi, after annealing treatment in oxygen. The measurements were acquired at RT under 488 nm excitation. Exponential fits are also plotted; in particular, single exponential fit has been used for the Er-doped samples and double exponential fit for the (Er+Bi) co-doped ones, by following Eq.3.2 [40].

The estimated fraction A and the decay rates, $1/\tau_1$ and $1/\tau_2$, have been reported as a function of Er content, N_{Er} , in Fig. 3.13.

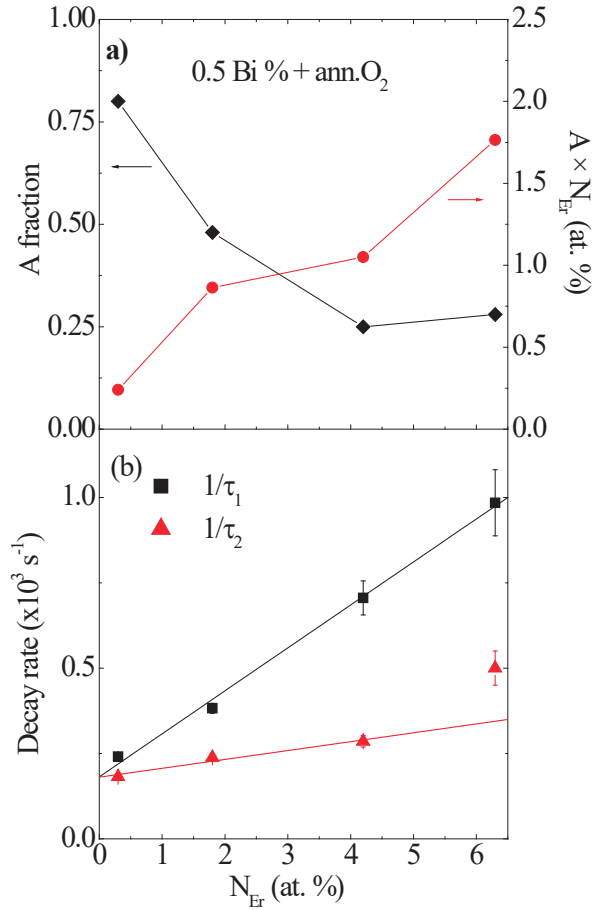


Figure 3.13. a) On the left hand scale, fraction of Er population, A , as a function of Er content of the samples implanted with the higher Bi dose and annealed in O₂. On the right scale, the correspondent absolute percentage of Er ions that decays with slower lifetime, τ_2 . **b)** Reciprocal of the two lifetime components, $1/\tau_1$ and $1/\tau_2$. Linear fits, by using Eq. (3.3), of the decay rate data are also reported [40].

It can be noticed that for the lowest Er content, 0.3 Er%, that is comparable with the Bi content, 0.5 Bi%, the fraction of Er ions, A , that de-excites with the longest lifetime τ_2 is about 80% of the total population. This value decreases by increasing Er content and it reaches 25% for 6.3 Er%.

However, if we consider the effective number of Er ions that have the longest lifetime, $A \times N_{Er}$, reported in the right hand scale of Fig. 3.13.a), it has a monotonic increase for all the considered range. The reached maximum $A \times N_{Er}$ value is about 1.7 Er% for the total content of 6.3 Er% and 0.5 Bi%.

The other interesting point is that, for all the Er contents, the fitted faster component τ_1 is always equal to the intrinsic Er decay time, τ_{Er} , as measured from the unimplanted sample having the same Er content. Moreover, both the $1/\tau_1$ and $1/\tau_2$ values follow a linear trend, as shown in Fig. 3.13.b). This behaviour, typically observed in Er-doped systems, as already mentioned in the previous section, is associable with the occurrence of concentration quenching mechanisms [39]. The decay rate can be expressed as a function of N_{Er} , by the relation

$$\frac{1}{\tau_0} + 8\pi C_{Er-Er} N_q N_{Er} \quad (3.3)$$

where C_{Er-Er} is the interaction coefficient between Er ions and the quenching centers, N_q , in the host, typically OH centers [39], $1/\tau_0$ is the intrinsic Er decay rate in absence of concentration quenching, that in absence of non-radiative channels is the radiative decay rate. The $1/\tau_1$ values, that are equal to the intrinsic Er decay rate, can be well fitted with Eq. (3.3) for all the range of Er contents; the same can be done also for the $1/\tau_2$ data set in the restricted range between 0.3 Er% and 4.2 Er%. By the linear fit of $1/\tau_1$ and $1/\tau_2$ data in Fig. 3.13.b), values of $(130 \pm 5) \times 10^{-3} \text{ cm}^3/\text{s}$ and $(30 \pm 5) \times 10^{-3} \text{ cm}^3/\text{s}$, respectively, have been obtained for $8\pi C_{Er-Er} N_q$, while the same τ_0 value, equal to $5.5 \pm 0.6 \text{ ms}$, has been achieved. This common τ_0 value suggests that the two populations have the same intrinsic Er decay time, though if it is smaller than the one obtained for Er in crystalline Y-Er

disilicate treated at 1200 °C [33] and in Er:Y₂SiO₅ nanoaggregates [32,51]. This can be attributed to the amorphous nature of the films studied in here, owing to the used lower annealing temperature (1000 °C). Moreover while the fraction of Er ions, (1-A), that de-excites with the decay rate $1/\tau_1$, is influenced only by the usual concentration quenching phenomena produced by Er-Er and Er-defects interactions, the remaining number of Er ions - namely $A \times N_{\text{Er}}$ - feel a reduced influence of the non-radiative channels as suggested by the lower $8\pi C_{\text{Er-Er}} N_q$ value. By considering the PL contribution of the two different populations and the relative lifetimes, a PL enhancement of about 1.3 can be estimated with respect to the unimplanted samples for all the Er contents, by confirming the obtained experimental value.

We can suppose that this behavior is associated to the formation of the Bi agglomerates observed in TEM images that better isolate the Er ions from the OH centers, thus limiting the influence of the quenching centers on the Er optical efficiency, as already found by Fujii et al. in nanocrystalline zeolites [16,21]. Thus the blocking action consists to efficient isolate an increasing number of Er ions, $A \times N_{\text{Er}}$, by causing an effective increase of the total decay time with a consequent increased contribution to PL intensities at 1.54 μm .

Moreover, since we have evaluated that these agglomerates are also responsible for mediated excitation to Er ions, when 255 nm excitation wavelength is used (see Fig. 3.7), we can suppose that the same fraction A of Er ions is involved also in the ET processes. Thus the η_{Enh} can be estimated by Eq. (3.1) by reaching at the best a factor of 500.

These results suggest that by further increasing the Bi content, an optimization of the Bi agglomerates blocking effect and contemporary ET mechanism are possible, thus maximizing the number of Er ions isolated by

OH centers and taking advantage of Bi^{3+} higher excitation cross section to enhance the Er optical efficiency of the system at 1.54 μm .

3.3. Bismuth as a sensitizer for Er optical emission in yttrium oxide thin films

In this section another silicon-compatible host, Y_2O_3 thin film, will be explored as a suitable material for the dissolution of high Er and Bi amounts for planar optical amplifiers. The peculiarity of this host is due to the similar body centered cubic (bcc) crystalline structure of Er_2O_3 and Y_2O_3 , with the same space group Ia-3 and similar lattice parameters, due to the fact that Er and Y have similar electronic configurations and ionic radii (0.89 Å for Y^{3+} and 0.88 Å for Er^{3+}). Thus Er can replace Y in substitutional position in the Y_2O_3 host, permitting to vary Er concentration in the host from the dopant level ($\sim 10^{18}$ at/cm³) to the constituent one ($\sim 10^{22}$ at/cm³). The dissolution of very high contents of Er ions not only permits to avoid the formation of optically inactive clusters but also to control the detrimental Er-Er interactions, such as cooperative upconversion and cross relaxation, that modify the optical properties of the system [52,53]. This is in good agreement with the possibility to well dissolve also high amounts of Bi ions in Y_2O_3 as demonstrated in chapter 2.

As a result of the bcc crystal structure of Y_2O_3 , when Er ions replace Y in its substitutional position, all Er ions are in the Er^{3+} chemical state in Y^{3+} substitutional positions but occupying different coordination shells depending on the total Er content, as demonstrated by Extended X-Ray Absorption Fine Structure (EXAFS) measurements in Fig. 3.14.a) [54]. In particular while the first coordination shell is always occupied by O atoms at

a distance of 2.25 – 2.33 Å, the second one (at a distance of 3.5 – 4 Å) can be almost fully occupied by Y^{3+} , mixed by Y^{3+} and Er^{3+} or totally by Er^{3+} depending on Er content. Two different regimes are thus evident, as sketched in Fig. 3.14.b). In the low Er content regime an Er ion can “see” another Er ion in the fourth (or higher) coordination shell, within a mean distance higher than 10 Å, so that only Er-O-Y or Y-O-Y bonds are present, thus the detrimental Er-Er interactions are avoided. Instead in the higher Er concentration regime these interactions become predominant due to the formation of Er-O-Er bonds. It has been found that the Er concentration in which the second regime starts is 10 Er at.%.

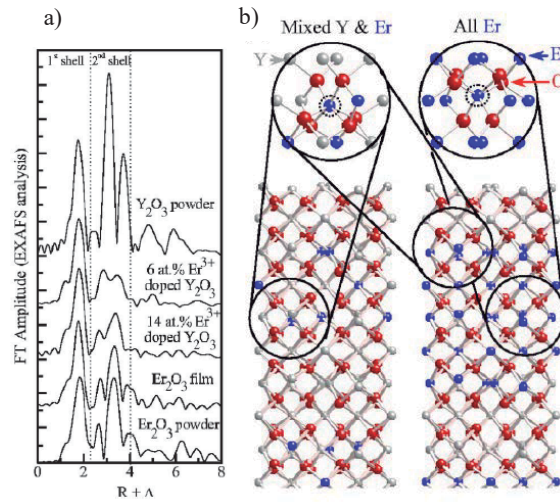


Figure 3.14. a) Fourier transform of EXAFS spectra from Y_2O_3 thin films containing different Er contents, compared with Er_2O_3 and Y_2O_3 thin films as references. b) Er local coordination in Y_2O_3 for low and high Er content regimes [54].

Moreover Y_2O_3 host is subject of great interest because it satisfies some features necessary for the realization of silicon-based waveguides and optical devices. In particular it is transparent from the visible to the infrared region, it has a band gap of about 5.8 eV and a refractive index of 1.9: these optical properties guarantee an high index contrast for an efficient light confinement in optical devices. Moreover yttria thin films are fully compatible with the standard Si technologies, as demonstrated by the good quality of the film grown on c-Si or silica substrate using different ultra large-scale integration (ULSI) compatible synthesis techniques, such as magnetron sputtering [55], ion beam sputtering [56], pulsed laser deposition [57].

Even if the Er: Y_2O_3 system has been widely studied, the coupling between Er and Bi was never reported. In the next section the optical properties of Er: yttrium oxide thin films will be firstly illustrated. Then the (Er+Bi) containing systems will be shown as a promising candidate for optical devices applications.

3.3.1. Er spectroscopy in yttrium oxide

Er: Y_2O_3 thin films were deposited on 5" c-Si wafers by radio-frequency magnetron co-sputtering. The power applied to the Y_2O_3 target was fixed at 500 W, while that one to the Er_2O_3 target was 25 W. We obtained polycrystalline stoichiometric yttrium oxide films, 120 nm thick, with concentration of 1.1 Er at.% (correspondent to 8×10^{20} Er/cm³), as measured by RBS, chosen in order to control and avoid Er-Er interactions. Further details on the films synthesis can be found in Ref. [53]. The samples annealed at 800°C for 30 min in oxygen were still polycrystalline, still with

the crystalline structure of the undoped Y_2O_3 and without an evidence of another Er_2O_3 crystalline phases, as demonstrated by XRD spectra. In particular for $\text{Er}:\text{Y}_2\text{O}_3$ thin films, having Er contents between 1×10^{20} and $1 \times 10^{22} \text{ Er/cm}^3$, the XRD spectra shown in Fig. 3.15 appeared very similar, with the same diffraction peaks and the same relative intensities, associated to the polycrystalline bcc structure of Y_2O_3 [58]. The only difference by increasing the Er content is a slight shift towards higher angles due to a lattice parameter contraction owing to the different Er and Y ionic radii. This result demonstrates the Er dispersion in substitutional Y positions inside the Y_2O_3 lattice, as already demonstrated in chapter 2 for the dissolution of Bi in Y_2O_3 .

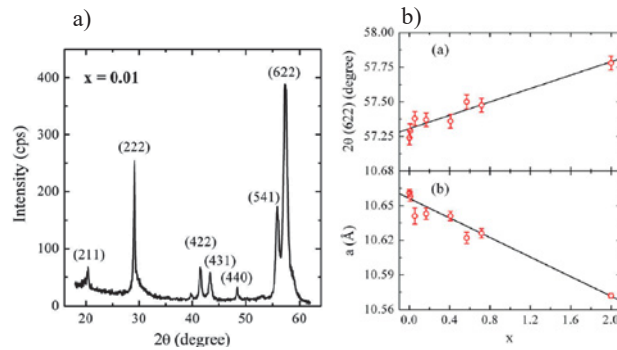


Figure 3.15. a) XRD spectrum of $\text{Y}_{2-x}\text{Er}_x\text{O}_3$ with $x=0.01$ (0.2 Er at.%) showing the same BCC structure of Y_2O_3 . Muller indices of the crystalline planes are also reported. b) shift towards higher angles of the XRD peak positions with the correspondent lattice parameter contraction by increasing Er [53].

The optical properties of the annealed $\text{Er}:\text{Y}_2\text{O}_3$ film have been analyzed by PL and lifetime measurements at room temperature. The 488 nm line of an Argon laser was chosen as pumping source, because it permits to excite directly the $^4\text{I}_{15/2} \rightarrow ^4\text{F}_{7/2} \text{Er}^{3+}$ transition. The PL spectrum obtained

for 1.1 Er at.% is shown in Fig. 3.16: different emission peaks have been observed, in particular centered at 566 nm, 660 nm, 980 nm and 1540 nm, associated respectively to the Er^{3+} transitions from ($^4\text{S}_{3/2}$, $^2\text{H}_{11/2}$), $^4\text{F}_{9/2}$, $^4\text{I}_{11/2}$ and $^4\text{I}_{13/2}$ to the $^4\text{I}_{15/2}$ ground state. In addition, the broad emission peaked at 1140 nm in Fig. 3.16 is ascribed to the Si band edge emission from the interface with the passivated SiO_2 layer formed between the Si substrate and the $\text{Er}:\text{Y}_2\text{O}_3$ thin film after oxidizing annealing as shown in section 2.2.2 for $\text{Bi}:\text{Y}_2\text{O}_3$.

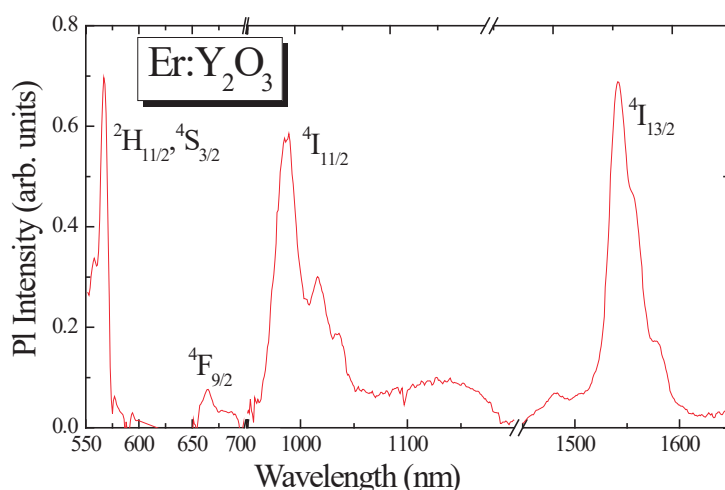


Figure 3.16. PL emission spectrum of $\text{Er}:\text{Y}_2\text{O}_3$ after annealing treatment at 800°C for 30 min in O_2 under 488 nm excitation at room temperature. The Er main emissions at 566 nm, 660 nm, 980 nm and 1540 nm are evident.

As already demonstrated for Bi, also Er atoms can occupy two non-equivalent lattice sites, the first having point symmetry C_2 with four equivalent Er-O bonds (distance 2.5 Å) and two slightly distorted Er-O

bonds (distance 2.33 Å); the second point symmetry is S_6 (also known as C_{3i}) characterized by six equivalent Er-O bonds (distance 2.26 Å) [59]. Differently from the permitted $\text{Bi}^{3+} {}^3\text{P}_1 \rightarrow {}^1\text{S}_0$ transition, for Er ions in S_6 site the electric-dipole transitions are not allowed since S_6 is an inversion center. For this reason optical emission from Er in Y_2O_3 comes from Er ions in the C_2 site.

The presence of all these Er emitting levels, differently from the unique 1.54 μm emission observed from $\text{Er}:\text{Y}_2\text{Si}_2\text{O}_7$ in section 3.2.2, is mainly ascribed to the lower phonon energy of the host, between 400 and 600 cm^{-1} . Since the emission probability is proportional to the ratio between the radiative rate ($W_r = 1/\tau_r$) and the total one ($W_r + W_{nr}$), the radiative de-excitation is more probable when the energy gap between two successive levels is higher than the phonon energy, 600 cm^{-1} . In this case more than one phonon should be involved in the de-excitation process thus lowering W_{nr} and therefore favoring the emission probability.

The radiative times for all the energy levels when Er is in Y_2O_3 host obtained by the Judd-Ofelt theory [60] are 78 μs , 698 μs , 644 μs , 6.8 ms and 7.7 ms respectively for Er de-excitations from ${}^2\text{H}_{11/2}$, ${}^4\text{S}_{3/2}$, ${}^4\text{F}_{9/2}$, ${}^4\text{I}_{11/2}$ and ${}^4\text{I}_{13/2}$ to the ${}^4\text{I}_{15/2}$ energy level. Figure 3.17 reports decay time curves of two of the most intense PL emissions, the $({}^2\text{H}_{11/2}, {}^4\text{S}_{3/2}) \rightarrow {}^4\text{I}_{15/2}$ at 566 nm and ${}^4\text{I}_{13/2} \rightarrow {}^4\text{I}_{15/2}$ at 1540 nm. Two very different temporal scales are evident: while at 566 nm we estimated a lifetime value of about 26 μs , a much longer lifetime has been observed at 1540 nm, equal to 2.5 ms for 1.1 Er at.%. Both values are compatible with the reported Er radiative lifetime of the ${}^4\text{S}_{3/2}$ and of ${}^4\text{I}_{13/2}$ in Y_2O_3 .

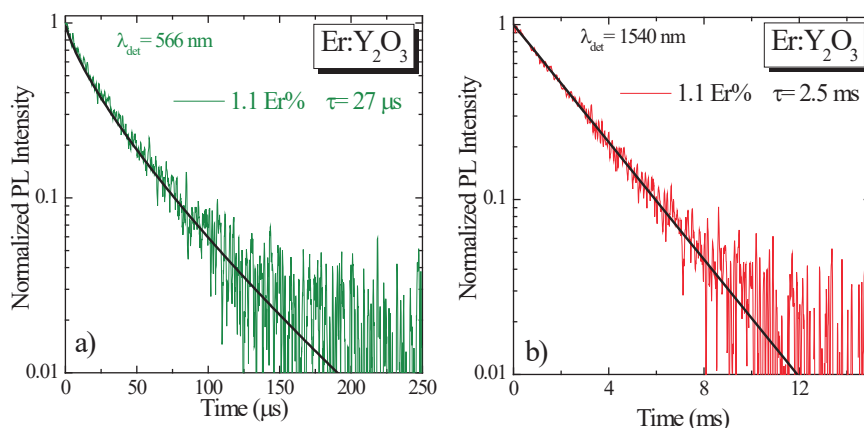


Figure 3.17. Time resolved measurements of Er emission at $\lambda_{\text{det}} = 566$ nm (a) and $\lambda_{\text{det}} = 1540$ nm (b) for Er:Y₂O₃ after annealing treatment at 800°C for 30 min in O₂. The measurements were acquired at RT under 488 nm excitation. Exponential fits are also reported with the estimated lifetime values.

3.3.2. Efficient Bi and Er coupling for visible and infrared emission

Bi ions were introduced in the Er:Y₂O₃ samples by ion implantation, as described in chapter 2, resulting in a Gaussian Bi profile spread over a thickness of about 80 nm, as measured by RBS. The Bi dose was varied in order to change the average Bi concentration between 3×10^{18} and 7×10^{20} Bi/cm³. The as-implanted samples were then annealed at 800°C for 30 min in oxygen atmosphere to stabilize the Bi³⁺ oxidation state and to remove eventual defects left over by the implantation process. The crystalline structure of the (Bi+Er):Y₂O₃ samples is unchanged with respect to the Bi:Y₂O₃ and Er:Y₂O₃. Thus it permits to conclude that even in presence of

both Er and Bi ions, both the species are well dissolved into the host, without forming separated crystalline phases.

The eventual coupling between Bi and Er ions has been analyzed through the study of the optical properties of the (Er+Bi):Y₂O₃ thin film.

The energy transfer (ET) process was firstly studied by Forster for allowed transitions in organic materials [61] and then extended to forbidden transitions in inorganic materials by Dexter [62]. It is expected to be highly efficient when there is a large spectral overlap between the sensitizer (called also donor) emission spectrum and the acceptor excitation spectrum. A critical Förster radius, R_0 , has also been defined as the sensitizer-acceptor distance where the de-excitation through ET has the same probability with respect to the radiative one. This value depends mainly on the overlapping integral between the donor luminescence $f_D(\lambda)$ (normalized at the whole integral in all the PL spectrum) and the acceptor absorbance $\varepsilon_A(\lambda)$, following the formula

$$R_0^6 = \frac{9000 \times \ln 10 \times \Phi_D \times \kappa^2}{128 \times \pi^5 \times n_r^4 \times N_A} \times \int_0^\infty f_D(\lambda) \varepsilon_A(\lambda) \lambda^4 d\lambda \quad (3.4)$$

where n_r is the refractive index of the host, N_A is Avogadro's number, Φ_D is the luminescence quantum yield of the donor and κ^2 is an orientation factor taking into account the relative orientation of the dipoles (for random orientation it is fixed at 2/3) [63]. Thus the Förster ET rate for dipole-dipole interaction can be written as a function of the sixth power of the donor-acceptor distance, r , that is [64]

$$k_{ET} = \frac{1}{\tau_D} \left(\frac{R_0}{r} \right)^6 \quad (3.5)$$

More in general also dipole-quadrupole and quadrupole-quadrupole interactions are permitted and in those cases the power 6 becomes respectively 8 or 10.

In order to verify if there are the conditions for the coupling between Bi and Er in our case, the Bi^{3+} (C_2) and the Bi^{3+} (S_2) emission spectra (studied in section 2.3.2) have been overlapped with the Er excitation spectrum, in absence of Bi, in Fig. 3.18. As it is possible to notice, the Bi^{3+} (C_2) emission band, between 360 nm and 680 nm, matches with several Er^{3+} excitation peaks, such as $^4\text{G}_{9/2}$ (360 nm), $^4\text{G}_{11/2}$ (378 nm), $^2\text{H}_{9/2}$ (410 nm), $^4\text{F}_{5/2}$ (455 nm), $^4\text{F}_{7/2}$ (488 nm), $^2\text{H}_{11/2}$ (520 nm). It overlaps also with one of the Er emitting levels shown in Fig. 3.16, $^4\text{S}_{3/2}$ (566 nm), indicated in figure as a line. Lower overlap is observed between Bi^{3+} (S_6) and Er^{3+} ions. Therefore we can expect the occurrence of energy transfer between both Bi^{3+} sites and Er^{3+} ions, but favored from Bi^{3+} in C_2 site.

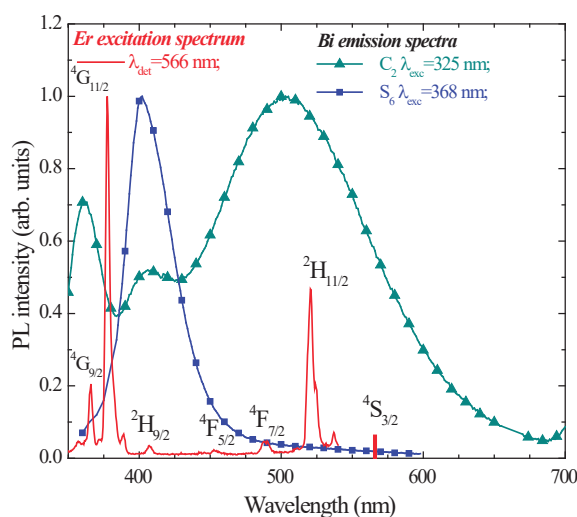


Figure 3.18. Comparison between $\text{Er}:\text{Y}_2\text{O}_3$ excitation spectrum detected at $\lambda_{\text{det}} = 566$ nm and emission spectrum of Bi^{3+} (C_2) and Bi^{3+} (S_6) in $\text{Bi}:\text{Y}_2\text{O}_3$ under $\lambda_{\text{det}} = 325$ nm and 368 nm.

In order to verify this coupling we have performed PL measurements with the 325 nm line of a He-Cd laser, in order to excite selectively Bi^{3+} ions in the C_2 symmetry and simultaneously to avoid the resonant Er excitation. The obtained PL spectra from the $(\text{Er}+\text{Bi})\text{:Y}_2\text{O}_3$ samples are shown in Fig. 3.19 for two different Bi contents as examples. In both cases we observe the Er^{3+} sharp peaks at 566 nm, 660 nm, 980 nm and 1540 nm and in addition the typical Bi^{3+} (C_2) emission peaked at 500 nm. It is interesting to note that the Bi^{3+} (C_2) intensity decreases if compared with the single Bi doping of Y_2O_3 reported in the same figure and already analyzed in chapter 2. The simultaneous decrease of Bi^{3+} luminescence and the appearance of Er^{3+} emissions suggest the occurrence of the effective ET from excited Bi^{3+} (C_2) to Er^{3+} ions. The same behavior has been obtained for all the implanted Bi concentrations.

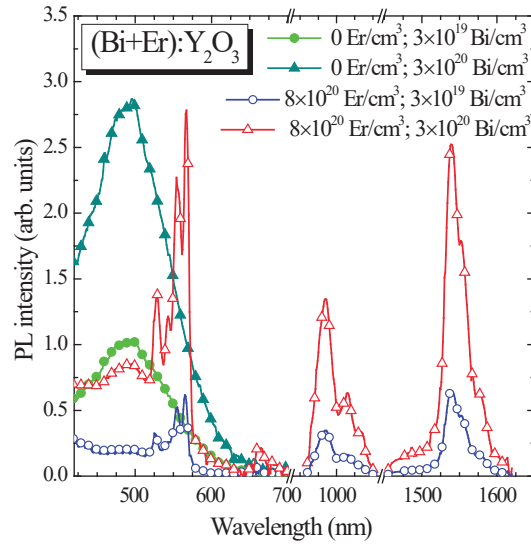


Figure 3.19. Room temperature photoluminescence spectra from $\text{Bi:Y}_2\text{O}_3$ and $(\text{Er}+\text{Bi})\text{:Y}_2\text{O}_3$ for two different Bi contents. The spectra have been measured by pumping with the 325 nm line of a He-Cd laser with a photon flux of 2×10^{18} photons/(cm^2s^{-1}) [65].

The emission pattern from (Er+Bi):Y₂O₃, after the Bi signal subtraction, is unchanged with respect to the one from Er:Y₂O₃ under direct excitation reported in section 3.3.1. Also the time resolved PL measurements revealed that Er³⁺ decay times of all its radiative levels are unchanged in presence of Bi ions, thus suggesting that the mechanisms of Er³⁺ de-excitation are independent of the Bi presence. Therefore no energy back-transfer (BT) from Er to Bi ions is present in this type of host, as instead found in many works on Er and Bi codoped glasses [17] Moreover, the same PL behavior has been obtained also by selectively exciting the S₆ symmetric site at 368 nm.

In order to confirm the origin of the Er³⁺ emission observed under 325 nm excitation, the Er excitation band in presence of Bi was obtained by PLE measurements, by varying the excitation wavelength between 280 nm and 500 nm and by fixing the detection wavelength to one of the Er³⁺ radiative transitions. Figure 3.20 reports the PLE spectra for detection wavelengths of 566 nm and 1540 nm, as examples, from the (Er+Bi):Y₂O₃ sample containing 3×10²⁰ Bi/cm³. The same broad excitation band, extended between 310 nm and 400 nm and centered at 330 nm, has been recorded for both the detection wavelengths. In addition it is interesting to note that the Er³⁺ PL signals expected under the known resonant excitation wavelengths (such as 360 nm, 378 nm, 410 nm, 455 nm and 488 nm, indicated as blue lines in the Fig. 3.20) are too low with respect to the signal observed under UV excitation to be visible in the spectra reported in Fig. 3.20.

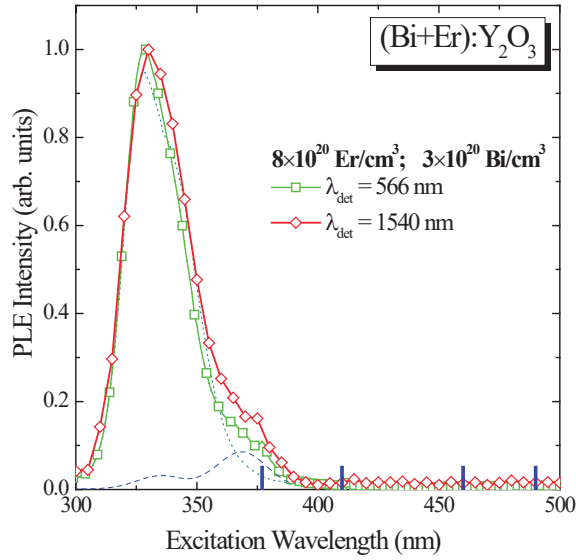


Figure 3.20. PLE spectra from (Er+Bi):Y₂O₃ recorded from Er at 566 nm and at 1540 nm. The blue lines at the bottom scale represent the excitation wavelengths corresponding to the Er energy levels. The deconvolution of Er excitation band in Bi (C₂) and Bi (S₆) excitation bands is also represented by dashed and dotted lines.

About the observed broad band, it can be described as the convolution of the Bi³⁺(S₆) and Bi³⁺(C₂) excitation bands, reported as dashed and dotted lines in Fig. 3.20 and already discussed in section 2.3.2. It is evident that the weight of the Bi³⁺(S₆) excitation band is very low with respect to the Bi³⁺(C₂) one. It suggests that the main ET process between Bi³⁺ and Er is more efficient when Bi³⁺ ions are in the C₂ site, as already suggested by the overlap integral in Fig. 3.18.

Therefore we can conclude that the observed Er³⁺ luminescence is due mainly to an ET from the Bi³⁺ (C₂) to the Er³⁺ ions: excited Bi³⁺ ions can either emit photons at around 500 nm, corresponding to the ³P₁→¹S₀

transition, or de-excite non-radiatively by transferring their energy to the ($^2H_{11/2}$, $^4S_{3/2}$) level of the nearby Er^{3+} ion. Then Er^{3+} ion de-excites by subsequent radiative decays to the ground state by emitting its characteristic photons in the visible and infrared regions.

A quantitative estimation of the Bi-Er ET efficiency, η_{ET} , for the C_2 site and of its dependence on Bi content has been obtained by considering the Bi^{3+} PL emission decrease when in presence of Er. In particular we have compared the Bi^{3+} PL emission from $(Er+Bi):Y_2O_3$, $PL(500\text{ nm})_{Er+Bi}$, and from $Bi:Y_2O_3$, $PL(500\text{ nm})_{Bi}$, for all the Bi concentrations. The η_{ET} values can be evaluated as [63]

$$\eta_{ET} = 1 - \frac{PL(500nm)_{Er+Bi}}{PL(500nm)_{Bi}} = 1 - \frac{\tau_{Er+Bi}}{\tau_{Bi}}. \quad (3.6)$$

The energy transfer efficiency of the Bi^{3+} (C_2 site) evaluated by PL intensity reduction is reported as a function of Bi content on the right hand scale of Fig. 3.21. It is about 85% for low Bi content, with only a slight decrease to about 70% for the higher Bi content despite the occurrence of the competitive Bi concentration quenching.

These considerations are further supported by time resolved measurements of Bi ions in both the C_2 and S_6 symmetry sites. In both cases a Bi lifetime reduction has been observed when in presence of Er ions, even if more marked for the C_2 site. The reduction of Bi lifetime can be explained by considering that the ET to Er ions represents an additional non-radiative decay channel to the Bi de-excitation. As example, by evaluating lifetime reduction for the Bi content of $3 \times 10^{20} \text{ Bi/cm}^3$, ET efficiency of 72% is obtained for C_2 symmetric site, compatible with the one obtained by the evaluation of PL reduction. Instead an efficiency of 45% is observed for S_6

symmetry sites, thus further confirming that C_2 symmetric site permits the best Bi-Er coupling.

In order to understand the efficiency trend of the Bi-Er coupling as a function of Bi concentration, we have compared the Er PL intensity trend as a function of Bi concentration with the Bi (C_2) PL trend in absence of Er. Figure 3.21 reports the PL trends relative to the Er^{3+} emissions at 1540 nm and at 566 nm from the (Er+Bi): Y_2O_3 and of the Bi^{3+} emission at 500 nm from Bi: Y_2O_3 as a function of Bi content.

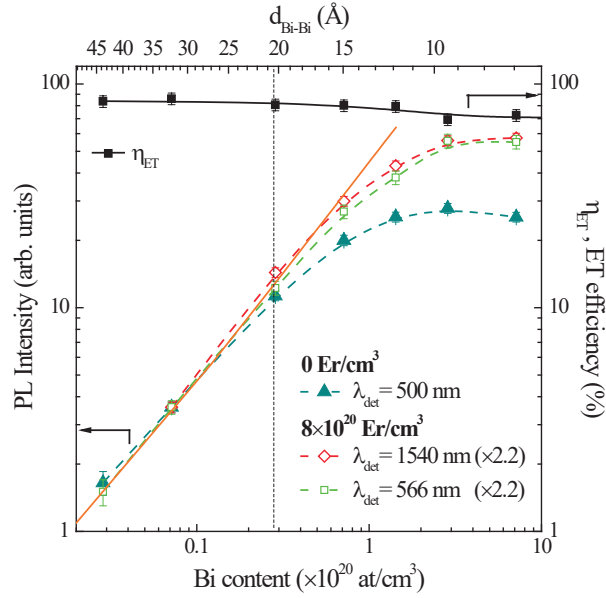


Figure 3.21. PL Intensity versus Bi concentration (and Bi-Bi mean distance, d_{Bi-Bi} , on top scale) recorded at 500 nm from Bi: Y_2O_3 , at 566nm (after subtraction of PL contribution from Bi, and at 1540 nm from (Er+Bi): Y_2O_3 . The continuous line is the linear fit to the data. On the right scale, ET efficiency calculated by PL reduction of Eq. (3.6), versus Bi content for (Er+Bi): Y_2O_3 samples. Black dotted line is reported to indicate the critical Bi content, Bi_0 [65].

The PL intensities of all the Er energy levels increase by increasing the Bi content with the same slope of the Bi^{3+} PL trend as expected thanks to the occurrence of ET from Bi to Er ions for all the Bi contents. However, in this case the deviation from the linear trend occurs for Bi concentrations higher than the critical concentration Bi_0 of $3 \times 10^{19} \text{ Bi/cm}^3$ for which the concentration quenching process between Bi ions occurs. These results confirm that the ET is efficient already at lower Bi concentration and moreover it is high even when the sensitizer optical efficiency is limited by the concentration quenching. In other words, the ET prevails over the latter effect for all the investigated Bi range. This behavior can be understood by considering that, being the Er content the same in all the samples, the mean Er-Bi distance, $d_{\text{Er-Bi}}$, is approximately unchanged and equal to about 6.8 Å. Er-Bi interactions are hence stronger than Bi-Bi interactions and only for Bi concentrations around $3 \times 10^{20} \text{ Bi/cm}^3$, well above Bi_0 , the Bi-Bi interactions start to be visible. When the Bi concentration reaches about $7 \times 10^{20} \text{ Bi/cm}^3$, corresponding to $d_{\text{Bi-Bi}} \sim d_{\text{Er-Bi}}$, the Bi-Bi concentration quenching starts to compete severely with the Bi-Er ET, thus inducing the saturation of the Er^{3+} PL intensity. These results suggest that the increase of the Bi content above Bi_0 , although deleterious for the Bi optical efficiency, permits to improve the Er emission, owing to their spatial distribution. Therefore, for $8 \times 10^{20} \text{ Er/cm}^3$ the optimized Bi-Er coupling is reached for concentrations of $3 \times 10^{20} \text{ Bi/cm}^3$ in $(\text{Er+Bi})\text{:Y}_2\text{O}_3$, corresponding to a Bi:Er ratio of about 1:3.

The presence of Bi^{3+} as a sensitizer for Er^{3+} is very important not only because it permits to extend the range of excitation wavelengths of the $(\text{Er+Bi})\text{:Y}_2\text{O}_3$ system but also because the direct Bi^{3+} excitation is expected to be more efficient than the direct Er excitation. In order to quantify the Er^{3+} excitation cross section through the Bi^{3+} sensitization in our $(\text{Er+Bi})\text{:Y}_2\text{O}_3$

samples, we compared the Er^{3+} emission obtained under Bi-mediated excitation with the one obtained under the direct 488 nm excitation. In the latter case the measurements have been rescaled to an equivalent thickness of 80 nm that corresponds to the thickness of the Bi containing layer, in order to consider the same volume of Er excited ions. Since we have found both the same Er emission patterns and the same decay times for each radiative Er level independently of the excitation conditions, in Fig. 3.22 we show the comparison between the Er^{3+} PL trends recorded at 1540 nm and at 566 nm as a function of the pump flux, under both the excitation conditions, from the (Er+Bi): Y_2O_3 sample containing $3 \times 10^{20} \text{ Bi/cm}^3$ (that is the one showing the best Er-Bi coupling). First of all it is easy to note that to obtain similar Er^{3+} PL intensities the 488 nm photon flux must be more than three orders of magnitude higher than the 325 nm photon flux.

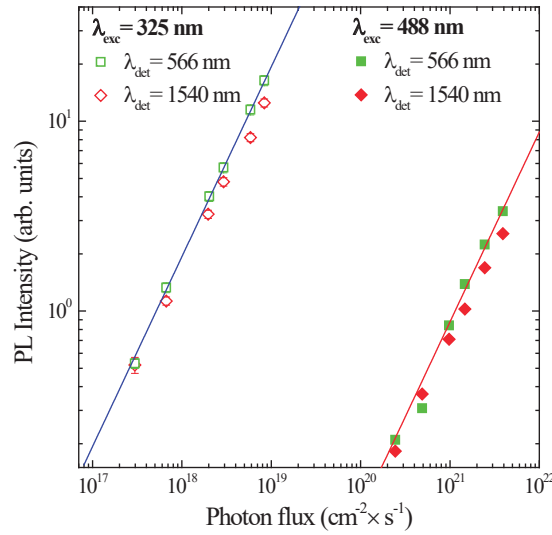


Figure 3.22. Photoluminescence intensity versus photon flux recorded at 566 nm and at 1540 nm from (Er+Bi): Y_2O_3 under 325 nm (indirect) and 488 nm (direct) excitation. Linear fits to the visible PL data are plotted.

In a linear regime the PL intensity I_{PL} versus the photon flux Φ can be fitted by the linear relation [2,66]

$$I_{PL} \propto \sigma \frac{\tau}{\tau_{rad}} N_{Er} \Phi, \quad (3.7)$$

where the slope depends on the total lifetime τ , the radiative lifetime τ_{rad} , the Er concentration N_{Er} and the Er^{3+} effective excitation cross section σ .

Thus by finding a linear regime in both the Er observed trends, permitting to deduce that no upconversion (UP) mechanisms are present for these samples, it is possible to extrapolate information about the mediated excitation cross section with respect to the direct one. Since the measured τ does not change under direct and mediated excitation, the ratio of the slopes of the fits obtained by using Eq. 3.7 for the Er green emission at 566 nm gives the ratio of the effective excitation cross sections under direct Er absorption, σ_{Er} , and under mediated excitation, σ_{Er-Bi} . We found that σ_{Er-Bi} is about 2220 times higher than σ_{Er} . Assuming σ_{Er} equal to $2.4 \times 10^{-21} \text{ cm}^2$ [67], we can estimate a σ_{Er-Bi} value of $5.3 \times 10^{-18} \text{ cm}^2$, that is compatible with the value of 10^{-17} cm^2 reported for Bi^{3+} direct excitation cross section in BiGeO [34]. This high value further confirms the very efficient energy transfer between Bi^{3+} and Er^{3+} ions in Y_2O_3 films; moreover it is interesting to underline that this value is one of the highest obtained for Er in Si compatible hosts.

In conclusions we have investigated an original class of mixed oxide containing both Bi and Er in Y substitutional positions. The ET efficiency of 70% has been demonstrated for the best Bi:Er ratio with an enhancement of the Er^{3+} effective excitation cross section by more than three orders of magnitude with respect to the direct one. These results make this material

very promising for Si-compatible optical amplifiers not only at 1540 nm, wavelength of interest for telecommunication, but also in the visible range due to the contemporary enhancement of visible Er emission from ($^4S_{3/2}$, $^2H_{11/2}$) and $^4F_{9/2}$ energy levels.

3.4. Conclusions

In this chapter the possibility to synthesize Bi and Er containing silicates and oxides using methods fully compatible with the standard silicon technologies has been demonstrated. While very high amount of Er ions can be well introduced and dissolved in both the matrices, by controlling in a continuous way its concentration and the Er-Er mean distances, we have demonstrated a good dissolution of Bi ions only in the oxide host.

By TEM imaging and STEM-EDX analyses it was possible to observe that in silicates host Bi always precipitates in clusters after annealing treatments in both N_2 and O_2 . These nanoclusters have metallic nature in N_2 and they are oxidized in O_2 , as demonstrated by the low loss energy spectrum acquired in STEM-EELS. The presence of metallic nanoparticles has been demonstrated to be deleterious for Er optical emission, introducing a new path of Er non radiative de-excitation that lowered its optical emission at 1.54 μm and, as a consequence, the optical efficiency of the system. However, in O_2 a totally different scenario has been observed; the stabilization of Bi^{3+} at lower Bi doses and the formation of Bi silicate nanoparticles at higher Bi doses have been shown. Moreover it was demonstrated that while only Bi^{3+} ions act as sensitizers for Er ions, Bi silicate nanoparticles have also a beneficial effect for Er emission since they reduce the interaction with non-radiative decay channels, as OH centers.

The energy transfer process between Bi and Er, found in silicates, can be maximized in an oxide host where all the Bi ions introduced are stabilized in the Bi^{3+} oxidation state. This process has been widely discussed and evidenced by studying the optical properties of the Er and Bi containing compounds. In particular, the contemporary reduction of Bi^{3+} PL emission and the respective lifetimes at 500 nm and 406 nm in presence of Er, the existence of Er luminescence under non resonant excitation and the correspondence between Bi and Er excitation bands suggest that all the energy absorbed by Bi ions is transferred to Er, thanks to the high overlap between the Bi emission bands and the Er excitation bands. As a consequence, Er ions can be excited through Bi ET processes in a wide range in the UV, between 300 and 400 nm with an estimated efficiency between 70% and 80%. Since no differences in the Er de-excitation mechanisms after Bi introduction have been evidenced, it was possible to deduce that Bi ions act only as a sensitizer and do not introduce any additional Er non-radiative path, permitting to greatly increase Er optical properties.

Er effective excitation cross section in presence of Bi has been evaluated in both the hosts by the comparison between Er optical properties under direct and mediated excitation by varying the excitation photon flux. In all the cases, an enhancement of Er excitation cross section has been obtained. This enhancement is by a factor of 5 in silicates at the lowest Bi content, where not all the Bi ions are stabilized in the Bi^{3+} state, and it reaches at best a factor of 500 in silicates with the highest Bi content, owing to the formation of Bi silicate nanoparticles. An even higher increment up to 2000 has been instead obtained in oxides allowing the Er mediated excitation cross section to reach values up to $5.3 \times 10^{-18} \text{ cm}^2$. This high value is due to a

good dissolution of Bi ions inside the host, that results in a very efficient ET process between Bi and Er ions, and to the high Bi excitation cross section, around 10^{-17} cm^2 .

These results demonstrated that by properly optimizing the synthesis and the post-annealing conditions and introducing Bi as a sensitizer these materials are good candidates for Si-compatible optical amplifiers at 1540 nm.

References

- [1]. <http://www.fowiki.com/b/understand-fiber-attenuation>.
- [2]. A. Polman, *J. Appl. Phys.* **82**, 1 (1997).
- [3]. N. Daldosso, L. Pavesi, *Laser & Photon. Rev.* **3**, 508 (2009).
- [4]. C. Strohhöfer, A. Polman, *Opt. Mater.* **21**, 705 (2003).
- [5]. P. Cardile, M. Miritello, F. Priolo, *Appl. Phys. Lett* **100**, 251913 (2012).
- [6]. G. C. Valley, *Opt. Fiber Tech.* **7**, 21 (2001).
- [7]. T. Schweizer, T. Jensen, E. Heumann, G. Huber, *Opt. Comm.* **118**, 557 (1995).
- [8]. H.-S. Hsu, C. Cai, A. M. Armani, *Opt. Exp.* **17**, 23265, (2009).
- [9]. B. Wang, R. M. Guo, X. J. Wang, L. Wang, L. Y. Hong, B. Yin, L. F. Gao, Z. Zhou, *Opt. Mater.* **34**, 1371 (2012).
- [10]. Y. Fujimoto, M. Nakatsuka, *Jpn. J. Appl. Phys.* **40**, L279 (2001).
- [11]. V. G. Truong, L. Bigot, A. Lerouge, M. Douay, I. Razdobreev, *Appl. Phys. Lett.* **92**, 041908 (2008).
- [12]. X. Meng, J. Qiu, M. Peng, D. Chen, Q. Zhao, X. Jiang, C. Zhu, *Opt. Exp.* **13**, 1628 (2005).
- [13]. H.-P. Xia, X.-J. Wang, *Appl. Phys. Lett.* **89**, 051917 (2006).
- [14]. V. O. Sokolov, V. G. Plotnichenko, E. M. Dianov, *Opt. Exp.* **21**, 9324 (2013).
- [15]. L. Su, H. Zhao, H. Li, L. Zheng, G. Ren, J. Xu, W. Ryba-Romanowski, R. Lisiecki, P. Solarz, *Opt. Lett.* **36**, 4551 (2011).

-
- [16]. H.-T. Sun, A. Hosokawa, Y. Miwa, F. Shimaoka, M. Fujii, M. Mizuhata, S. Hayashi, and S. Deki, *Adv. Mater.* **21**, 3694 (2009).
- [17]. M. Peng, N. Zhang, L. Wondraczek, J. Qiu, Z. Yang, Q. Zhang, *Opt. Exp.* **19**, 20799 (2011).
- [18]. T. M. Hau, X. Yu, D. Zhou, Z. Song, Z. Yang, R. Wang, J. Qiu, *Opt. Mater.* **35**, 487 (2013).
- [19]. Z. Bai, H.-T. Sun, T. Hasegawa, M. Fujii, F. Shimaoka, Y. Miwa, M. Mizuhata, S. Hayashi, *Opt. Lett.* **35**, 1926 (2010).
- [20]. Z. Bai, M. Fujii, T. Hasegawa, K. Imakita, Y. Miwa, M. Mizuhata, S. Hayashi, *Microporous and Mesoporous Materials* **145**, 21 (2011).
- [21]. H.-T. Sun, T. Hasegawa, M. Fujii, F. Shimaoka, Z. Bai et al. *Appl. Phys. Lett.* **94**, 141106 (2009).
- [22]. R. Cao, T. Fu, Y. Cao, H. Ao, S. Guo, G. Zheng, *Mater. Lett.* **155**, 68 (2015).
- [23]. W. A. I. Tabaza, H. C. Swart, R.E. Kroon, *J. Lumin.* **148**, 192 (2014).
- [24]. M. N. Huang, Y. Y. Ma, X. Y. Huang, S. Ye, Q. Y. Zhang, *Spectr. Acta Part A: Mol. Biomol. Spectr.* **115**, 767 (2013).
- [25]. X. Y. Huang, X. H. Ji, Q. Y. Zhang, *J. Am. Ceram. Soc.* **94**, 833 (2011).
- [26]. C. Hazra, S. Sarkar, V. Mahalingam, *RSC Adv.* **2**, 6926 (2012).
- [27]. R. Zhou, Y. Kou, X. Wei, C. Duan, Y. Chen, M. Yin, *Appl. Phys. B* **107**, 483 (2012).
- [28]. M. Miritello, R. Lo Savio, F. Iacona, G. Franzò, A. Irrera, A. M. Piro, C. Bongiorno, F. Priolo, *Adv. Mater.* **19**, 1582 (2007).
- [29]. E. Snoeks, P.G. Kik, A. Polman, *Opt. Mater.* **5**, 159 (1996).
- [30]. W. Y. Ching, L. Ouyang, Y.-N. Xu, *Phys. Rev. B* **67**, 245108 (2003).
- [31]. M. Díaz, C. Pecharromán, F. del Monte, J. Sanz, J. E. Iglesias, J. S. Moya, C. Yamagata, S. Mello-Castanho, *Chem. Mater.* **17**, 1774 (2005).
- [32]. K. Suh, J. H. Shin, S.-J. Seo, B.-S. Bae, *Appl. Phys. Lett.* **92**, 121910 (2008).
- [33]. M. Miritello, R. Lo Savio, P. Cardile, F. Priolo, *Phys. Rev. B* **81**, 041411 (2010).
- [34]. M. J. Weber, R. R. Monchamp, *J. Appl. Phys.* **44**, 5495 (1973).

- [35]. J. Ito, H. Johnson, *Am. Mineralog.* **53**, 1940 (1968).
- [36]. U. Kolitsch, V. Ijevskii, H. J. Seifert, I. Wiedmann, F. Aldinger, *J. Mater. Science* **32**, 6135 (2006).
- [37]. T. R. Dinger, R. S. Rai, G. Thomas, *J. Am. Ceram. Soc.* **71**, 236 (1988).
- [38]. J. Zheng, Y. H. Zuo, L. Z. Zhang, W. Wang, C. L. Xue, B. W. Cheng, J. Z. Yu, H. Q. Guo, Q. M. Wang, *J. Lumin.* **130**, 1760 (2010).
- [39]. M. B. Camargo, L. Gomes, S. P. Morato, *Opt. Mater.* **4**, 597 (1995).
- [40]. A. Scarangella, M. Miritello, F. Priolo, *J. Appl. Phys.* **118**, 123511 (2014).
- [41]. W. Xiong, Y. Zhou, F. Guo, L. Chen, C. Luo, H. Yuan, *J. Cryst. Growth* **377**, 160 (2013).
- [42]. H. Jiang, X. Wang, G. Hao, L. Wang, *J. Mat. Sci.: Mater. Electron.* **24**, 814 (2013).
- [43]. S. Lozano-Perez, V. de Castro Bernal, R. J. Nicholls, *Ultramicroscopy* **109**, 1217 (2009).
- [44]. N. Ikarashi, K. Manabe, *J. Appl. Phys.* **94**, 480 (2003).
- [45]. G. Lucovsky, Y. Zhang, G. B. Rayner Jr., G. Appel, H. Ade, J. L. Whitten, *J. Vac. Sci. Technol. B* **20**, 1739 (2002).
- [46]. M. Miritello, R. Lo Savio, A. M. Piro, G. Franzò, F. Priolo, *J. Appl. Phys.* **100**, 013502 (2006).
- [47]. R.F. Egerton, *Electron Energy-Loss Spectroscopy in the Electron Microscope*, 3th edition (Springer, 2011).
- [48]. N. Jiang, D. Sua, J. C. H. Spence, S. Zhou, J. Qiu, *Solid State Comm.* **149**, 111 (2009).
- [49]. F. Yiting, F. Shift, S. Renying, M. Ishii, *Progr. Cryst. Growth Ch. Mater.* **40**, 183 (2000).
- [50]. S. Zhou, N. Jiang, B. Zhu, H. Yang, S. Ye, G. Lakshminarayana, J. Hao, J. Qiu, *Adv. Funct. Mater.* **18**, 1407 (2008).
- [51]. C. Li, C. Wyon, R. Moncorgè, *IEEE J. Quantum Electron.* **28**, 1209 (1992).
- [52]. F. Vetrone, J.-C. Boyer, J. A. Capobianco, A. Speghini, M. Bettinelli, *Chem. Mater.* **15**, 2743 (2003).

- [53]. R. Lo Savio, M. Miritello, P. Cardile, and F. Priolo, *J. Appl. Phys.* **106**, 043512 (2009).
- [54]. J. Hoang, T. T. Van, M. Sawkar-Mathur, B. Hoex, M. C. M. Van de Sanden, W. M. M. Kessels, R. Ostroumov, K. L. Wang, J. R. Bargar, J. P. Chang, *J. Appl. Phys.* **101**, 123116 (2007).
- [55]. T.-M. Pan, J.-D. Lee, *J. El. Mater.* **36**, 1395 (2007).
- [56]. R. J. Gaboriaud, F. Pailloux, P. Guerin, F. Paumier, *Thin Solids Film* **400**, 106, (2001).
- [57]. S. Zhang, R. Xiao, *J. Appl. Phys.* **83**, 3842 (1998).
- [58]. JCPDS database; power diffraction file no. 41-1105 .
- [59]. R. Miida, F. Sato, M. Tanaka, H. Naito, H. Arashi, *J. Appl. Crystallogr.* **30** 272 (1997).
- [60]. M. J. Weber, *Phys. Rev.* **171**, 283 (1968).
- [61]. T. Förster, *Ann. Phys.* **6**, 55 (1948).
- [62]. D. L. Dexter, *J. Chem. Phys.* **21**, 836 (1953).
- [63]. L. J. Charbonnière, N. Hildebrandt, *Eur. J. Inorg. Chem.* **2008**, 3241 (2008).
- [64]. F. Auzel, *Chem. Rev.* **104** , 139 (2004).
- [65]. A. Scarangella, R. Reitano, G. Franzò, F. Priolo, M. Miritello, *Appl. Phys. Lett.* **107**, 041908 (2015).
- [66]. A. J. Kenyon, *Semicond. Sci. Technol.* **20**, R65 (1997).
- [67]. W. J. Miniscalco, *J. Lightwave Technol.* **9**, 234 (1991).

List of publications

- A. Scarangella, M. Miritello and F. Priolo, “*Influence of Bi on the Er luminescence in yttrium-erbium disilicate thin films*”, **Journal of Applied Physics** 116, 123511 (2014); doi: 10.1063/1.4896495
- A. Scarangella, R. Reitano, G. Franzò, F. Priolo, and M. Miritello, “*Enhancement of Er optical efficiency through bismuth sensitization in yttrium oxide*”, **Applied Physics Letters** 107, 041908, (2015), doi: 10.1063/1.4927833
- A. Scarangella, S. Boninelli, G. Amiard, F. Priolo and M. Miritello, “*Nanometric resolved investigation of Bi dissolution in Y-Er disilicate thin films*”, **in preparation**.
- A. Scarangella, R. Reitano, G. Franzò, F. Priolo, and M. Miritello, “*Time resolved spectroscopy of Bi^{3+} ions in yttrium oxide thin films*”, **in preparation**.

Acknowledgments

Alla fine di questi tre anni di dottorato, volati troppo rapidamente, sento quasi il bisogno di fermarmi un attimo a pensare a quello che hanno rappresentato per me, a quanto ho guadagnato grazie alle persone che ho incontrato e conosciuto, ai risultati che ho ottenuto non soltanto da un punto di vista puramente scientifico ma anche etico e comportamentale, perché ogni persona che ho avuto il piacere di incrociare in questi tre anni è stata in grado di insegnarmi qualcosa da diversi punti di vista.

Ringrazio innanzitutto il Prof. Priolo che ha seguito il mio percorso scientifico sin dall'attività svolta per la tesi magistrale aiutandomi a raggiungere anche quest'altro importante traguardo.

Un grazie particolare va a Maria che, al di là del suo ruolo di supervisor e di guida nell'attività sperimentale, è stata sempre disponibile con me, dispensando consigli e suggerimenti su ogni campo, in parte grazie ai quali sono diventata la persona che adesso sono, supportandomi e sopportandomi soprattutto in questo ultimo periodo, difficile tanto per me quanto per lei (quindi grazie anche ad Aurora!). Penso di poter dire che l'intesa che si è creata tra di noi è veramente particolare e di questo la ringrazio.

Il Prof. Reitano ha aggiunto un tocco di curiosità e divertimento alla mia attività sperimentale, rendendo i turni allo spettrofluorimetro quasi una vera e propria gita (sebbene stancante...) e permettendomi di dare un notevole incremento alla attività di ricerca svolta durante questa tesi.

Ringrazio Simona che invece è stata una fonte di consigli scientifici e umani, in cui è sempre stato piacevole confrontarsi, da cui ho appreso tanto e con cui sono contenta di aver instaurato un rapporto che va al di là delle mura di questo dipartimento.

Un grazie va anche alla Dr.ssa Franzò che è stata sempre disponibile al confronto, con la sua esperienza e professionalità.

Un ringraziamento va anche a tutti i membri del gruppo Matis del CNR-IMM, ognuno dei quali ha contribuito con un tassello al puzzle del mio dottorato: il Prof. Terrasi, la Prof.ssa Grimaldi, il Dr. Iacona, Vittorio, Salvo M., Isodiana, Lucia, Alessia, Giuliana, Elena, Paolo M., Massimo,

Francesco, Eric, Viviana, Ruy, Maria Antonietta e i ragazzi che hanno intersecato la mia attività di dottorato, Salvo C., Giorgia S., Paolo S., Paolo C., Antonella, Stefano e ai miei ex compagni di studi, adesso colleghi Rosario (fornitore di patatine anti depressive), Marta, Giacomo e Federica. Grazie anche a Giuseppe P., Carmelo P. e Salvo T. per la loro esperienza tecnica.

In particolare ringrazio i miei “compagni di sorte” Vicky, Enrica e Giuseppe C. con cui ho condiviso tanti momenti importanti durante questo dottorato, tra cui le ansie di quest’ultimo periodo di scrittura, compreso il pranzo dell’Immacolata passato in un deserto diartimento o le chiamate empatiche alle 10 di sera.

Ringrazio anche Daniele che invece ha allietato questi tre anni con momenti di svago come i bellissimi tornei di pallavolo che ha organizzato e che hanno alleviato in parte le mie stancanti giornate. E i miei attuali e ex compagni di stanza che mi hanno sempre saputo consigliare bene e confortare nei momenti di bisogno, Gabriele, Seweryn, Pietro e Josè (compagna di stanza, di merende, di the, di dolci, di chiacchierate, e potrei continuare all’infinito).

Grazie anche alla mia famiglia e ai miei genitori che mi sono sempre stati vicino, nonostante i miei sbalzi di umore; alle mie amiche di una vita, Annalisa, Ilenia, Mariangela, Sabrina, Manuela e Laura per cui le parole di ringraziamento non potrebbero bastare; a Cristina, la cui compagnia mi manca sempre; a Chiara e Desy che mi hanno aiutato ad affrontare questo periodo difficile a prescindere dalla tesi; e grazie anche a Giuseppe che, nonostante l’enorme cambiamento nella sua vita, è riuscito ad essere presente in quest’ultimo mese, seppur lontano, e che mi ha sempre supportato in questi tre anni di dottorato, credendo sempre in me e tirando fuori il meglio di me. Il futuro è incerto per tutti, ma la persona con cui voglio dividerlo per me è l’unica certezza.

*“Here I stand staring at the sun
Distant land, staring at the sun
You're not there but we share the same one
Miles apart, staring at the sun
Distant talks, staring at the sun
One thing's true, just like you
There's only one”*

Curriculum Vitae

Adriana Scarangella was born in Catania (CT) on December 30th 1988.

1. Education

- High school diploma obtained in 2007 with grade 100/100
- Bachelor Degree in Physics obtained in 2010 at the University of Catania with full marks 110/110 cum laude with a dissertation entitled: “Interactions between electromagnetic radiation and metallic nanoparticles” (supervisor Dr. Giovanni Piccitto).
- Master Degree in Physics obtained in 2012 at the University of Catania with full marks 110/110 cum laude with a dissertation entitled: “Optical and Structural Properties of Er-Y mixed disilicates doped with bismuth” (supervisors: Prof. Francesco Priolo, Dr. Maria Miritello).
- Admission to the PhD course in Materials Science and Technology (XXVIII) in 2013.
- PhD student in Materials Science and Technology at the University of Catania in collaboration with CNR-IMM-MATIS since January 2013 to October 2015, in the framework of the PON project Bio-nanotech Research and Innovation Tower (BRIT) financed by the Italian Ministry for Education, University and Research (MIUR).
- Research contract at CNR-IMM-MATIS since December 2015.

2. Additional Skills

- Material synthesis and modification

Synthesis of Rare Earths doped thin films through magnetron co-sputtering;
Modification of structural and electrical properties of materials through ion implantation processes; Optimization of the quality of the thin films through fluxed annealing treatment and rapid thermal annealing (RTA)

- Chemical and structural characterization

Rutherford Backscattering Spectrometry (RBS), X-Ray Diffraction (XRD) Spectroscopy, Scanning electron microscopy (SEM), Transmission electron microscopy (TEM), Ellipsometry, X ray photoelectron spectroscopy (XPS), Absorption and Reflectivity measurements.

- Optical characterization

Steady state and time resolved photoluminescence (PL) spectroscopy, Cathodoluminescence (CL) spectroscopy, photoluminescence excitation spectra (PLE).

- Good competences in Microsoft Office™ tools (Word, Excel, Power Point), Origin PRO; basic competences in C Programming Language
- Good competences in simulation software as SIMNRA, SRIM, RUMP e GENPLOT, basic competences in Gatan Digital Micrograph and CaRIne Crystallography

3. Collaborations

- Università di Catania, Dipartimento di Fisica e Astronomia, Catania, Italia.
- Istituto di Microelettronica e Microsistemi (CNR-IMM), Catania, Italia.
- ST Microelectronics, Catania, Italia.
- Istituto di Processi Chimico-Fisici (CNR-IPCF), Messina, Italia
- Istituto dei Materiali per l'Elettronica ed il Magnetismo (IMEM-CNR), Parma, Italia .
- California Institute of Technology (CALTECH), Atwater Group, Pasadena - California, USA.
- Interdisciplinary Nanoscience Center – INANO, Arrhus University, Denmark.
- CP2M- Marseille, Aix-Marseille University, Marsiglia, Francia.

4. Participation to conferences, workshops and seminars

Adriana Scarangella has participated to international conferences and school by personally presenting 4 oral contributions and 2 posters:

- II edition of the workshop Carbomat 2011, “Carbon-based low-dimensional Materials”, Catania, Italy (5-7 December 2011).
- International Summer School “Material for Renewable Energy”, Erice, Italy (18-28 July 2012).
- International Winter School “7th Optoelectronics and Photonics Winter School”, Levico Terme, Italy (16-22 March 2013), **with a personal poster presentation:** “*Optical and Structural Properties of Bi-doped Er-Y disilicate thin film on silicon substrate*”
- International School on Photonics: “Where photonics meets electronics”, Arezzo, Italy (20-24 May 2013).
- International School “Flexible Sensors and Electronics – Materials, Methods & Technologies”, Catania, Italy (11 - 13 September 2013).
- International Summer School “Material for Renewable Energy 2014”, Erice, Italy (11-19 July 2014) **with a personal poster presentation:** “*Bismuth and Erbium doped thin films for Si optical amplifiers at telecommunication wavelength*”
- E-MRS Fall Meeting 2014, Warsaw (Poland), (14-20 September 2014) **with a personal oral contribution:** “*Efficient emission at 1.54 micron from Er in bismuth doped yttrium oxide*”
- IEEE NMDC 2014, Acicastello, Italy (12-15 October 2014) **with a personal oral contribution:** “*Bismuth as sensitizer for Er-based thin films*”

- E-MRS Spring Meeting 2015, Lille (France), (11-15 May 2015) **with a personal oral contribution:** “*Bismuth as a sensitizer for efficient Er-based photonics materials*”
- FISMAT 2015, Palermo, Italy (28 September- 02 October 2015) **with a personal oral contribution:** “*Bismuth and Erbium co-doped yttrium oxide for efficient photonics devices at 1.54 μm* ”

5. Other activities

- President of the student project “EPS Young minds - Catania section” funded by European Physical Society and of the student project “Archimedes - Catania Chapter”, funded by Optical Society of America since 2012.
- Tutor for bachelor students in the class of Experimental Physics in 2012.
- Active participation to the academic contest “Start-up Academy 2014” at the University of Catania (C.A.P.I.T.T. - Scuola Superiore di Catania - C.O.F.) after a preselection of 20 entrepreneurial ideas with the project “Gifted - Servizio di Consulenza all'Acquisto”.

6. Awards

E-MRS Graduate Student Award in Symposium H, “*Nanoparticles in dielectric matrix for electronics and optics: from the fabrication to the devices*”, E-MRS Spring Meeting 2015.